



저작자표시-비영리-변경금지 2.0 대한민국

이용자는 아래의 조건을 따르는 경우에 한하여 자유롭게

- 이 저작물을 복제, 배포, 전송, 전시, 공연 및 방송할 수 있습니다.

다음과 같은 조건을 따라야 합니다:



저작자표시. 귀하는 원저작자를 표시하여야 합니다.



비영리. 귀하는 이 저작물을 영리 목적으로 이용할 수 없습니다.



변경금지. 귀하는 이 저작물을 개작, 변형 또는 가공할 수 없습니다.

- 귀하는, 이 저작물의 재이용이나 배포의 경우, 이 저작물에 적용된 이용허락조건을 명확하게 나타내어야 합니다.
- 저작권자로부터 별도의 허가를 받으면 이러한 조건들은 적용되지 않습니다.

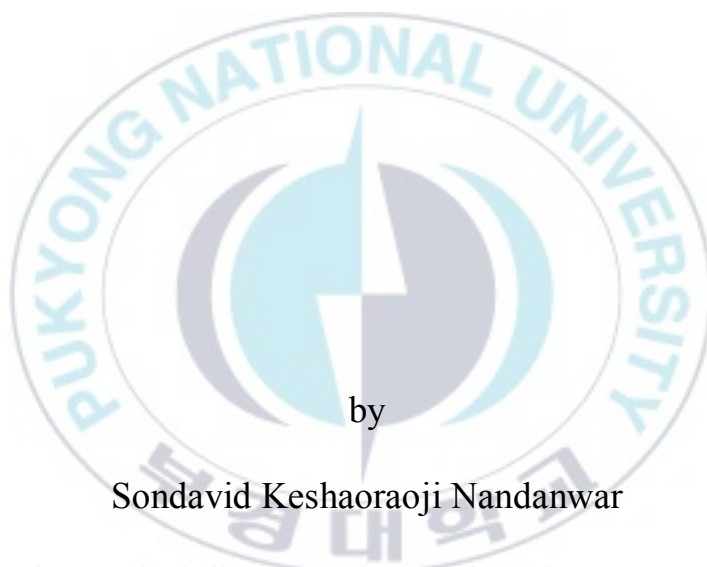
저작권법에 따른 이용자의 권리는 위의 내용에 의하여 영향을 받지 않습니다.

이것은 [이용허락규약\(Legal Code\)](#)을 이해하기 쉽게 요약한 것입니다.

[Disclaimer](#)

Thesis for the Degree Doctor of Philosophy

Synthesis, Characterization, and Environmental Applications of Organometallic Complexes and Nano-Metal Oxides



Sondavid Kesharaoji Nandanwar

Department of Interdisciplinary Program of Marine Convergence Design

The Graduate School

Pukyong National University

February 2021

Synthesis, Characterization, and Environmental Applications of Organometallic Complexes and Nano-Metal Oxides

(유기 금속 복합체 및 나노 금속 산화물의 합성, 특성 분석 및 활용 연구)

Advisor: Prof. Cho Jeong Hyung

by
Sondavid Kesharaoji Nandanwar

A thesis submitted in partial fulfillment of the requirements
for the degree of
Doctor of Philosophy

in Department of Interdisciplinary Program of Marine Convergence Design, The Graduate
School,
Pukyong National University
February 2021

Synthesis, Characterization, and Environmental Applications of Organometallic
Complexes and Nano-Metal Oxides

A dissertation

by

Sondavid Kesharaoji Nandanwar

Approved by:



(Chairman) Hee Jae Shin



(Member) Myung Won Lee



(Member) Songyi Lee



(Member) Hak Jun Kim



(Member) Jeong Hyung Cho

February 19, 2021

DEDICATION

This dissertation is wholeheartedly dedicated to my beloved parents, who have been my source of inspiration and gave me strength when I thought of giving up, who continually provide their moral, spiritual, emotional, and financial support.

To my brothers, sisters, relatives, mentors, friends, and lab mates who shared their words of advice and encouragement to finish my research.



Table of Content

List of Figure	v
List of Table	viii
List of Abbreviation	ix
Abstract	xiii
Chapter 1 General introduction.....	1
1.1 Organometallic complexes	2
1.1.1 Synthesis and characterization of organometallic complexes	4
1.1.2 Applications of zinc(II) and cobalt(II) organometallic complexes	5
1.2 Nano-metal oxides.....	8
1.2.1 Methods for synthesis of nano-metal oxides	9
1.2.2 Characterization of nano-metal oxides	10
1.2.3 Applications of NMO	12
1.3 Purpose of this work.....	13
1.4 References.....	15
Part I Synthesis of zinc(II)-azole and cobalt(II)-azole complexes for the removal of antibiotic resistant bacteria	29
Chapter 2 Synthesis and characterization of novel chelation-free Zn(II)-azole complexes: Evaluation of antibacterial, antioxidant and DNA binding activity ...	30
2.1 Abstract	30
2.2 Introduction	31
2.3 Material and methods	34
2.3.1 General method for the synthesis of complexes	34
2.3.2 Antibacterial assay	35
2.3.3 DNA mobility shift assays	35
2.3.4 Antioxidant assay	36
2.4 Results and discussion.....	37
2.4.1 Synthesis of Zn1-3.....	37
2.4.2 Molecular structures of Zn(II)-complexes Zn1-3	37

2.4.3 Antibacterial activity	42
2.4.4 Gel-electrophoresis assay	43
2.4.5 Antioxidant assay	45
2.5 Conclusion	47
2.6 References.....	48
Chapter 3 Cobalt(II) Benzazole Derivative Complexes: Synthesis, Characterization, Antibacterial Activity, Synergistic Activity with Antibiotics and Its Mechanism of Action	55
3.1 Abstract.....	55
3.2 Introduction.....	56
3.3 Results and discussion.....	59
3.3.1 Synthesis	59
3.3.2 Crystal structures	59
3.3.3 Determination of minimal inhibitory concentration.....	62
3.3.4 Synergistic effect.....	64
3.3.5 SYTOX green uptake assay	66
3.4 Conclusion	67
3.5 Experimental Section	68
3.5.1 Materials, instrumentation, and physical measurements	68
3.5.2 General method for the synthesis of Co1-3	68
3.5.3 Antibacterial assay	69
3.5.4 Checkerboard dilution test.....	70
3.5.5 SYTOX green uptake assay	70
3.6 References.....	72
Part II Algal growth inhibition and dye degradation efficiency of synthetic MoZnO and Cu-VO.....	80
Chapter 4 Synthesis, Characterization, and Anti-algal Activity of Molybdenum Doped Metal Oxides	81
4.1 Abstract.....	81
4.2 Introduction.....	82
4.3 Results	85

4.3.1 Synthesis, morphological and microstructural analysis of MoZnO	85
4.3.2 Structural analysis of MoZnO	87
4.3.3 Anti-algal assay	90
4.3.4 Mechanisms of algae growth inhibition	94
4.4 Discussion	100
4.5. Materials and methods	103
4.5.1 Preparation of MoZnO	103
4.5.2 Characterization	103
4.5.2.1 Morphological and microstructural analysis	103
4.5.2.2 Structural analysis	103
4.5.2.2.1 XRD analysis	103
4.5.2.2.2 FT-IR analysis	105
4.5.3 Algae Growth Inhibition	105
4.5.3.1 Algae culture	105
4.5.3.2 Algae growth inhibition assay	105
4.5.4 Effect of metal salts, metal oxides and their combinations	106
4.5.5 Experiments on algae growth inhibition mechanisms	107
4.5.5.1 ·OH assay	107
4.5.5.2 ROS assay	107
4.5.5.3 Lipid peroxidation assay	108
4.5.5.4 Effect of agglomeration	108
4.5.5.4.1 Optical microscope analysis	108
4.5.5.4.2 SEM analysis	109
4.5.6 Statistical analysis	109
4.6 Conclusions	110
4.7 References	112
Chapter 5 Microwave□Assisted Synthesis and Characterization of Solar□Light□ Active Copper–Vanadium Oxide: Evaluation of Antialgal and Dye Degradation Activity	122
5.1 Abstract	122

5.2 Introduction.....	123
5.3. Results	126
5.3.1 Synthesis, morphological and microstructural analysis of Cu-VO	126
5.3.2 Structural analysis of Cu-VO	128
5.3.3 Anti-algal assay.....	131
5.3.4 Dye degradation assay	133
5.3.5 Mechanisms of action.....	133
5.4 Discussion.....	136
5.5 Materials and methods	139
5.5.1 Synthesis of Cu-VO.....	139
5.5.2 Characterization	139
5.5.3 Photocatalytic experiments	140
5.5.3.1 Algae culture.....	140
5.5.3.2 Algae growth inhibition.....	140
5.5.3.3 Photocatalytic dye degradation	140
5.5.4 Photocatalysis mechanism.....	141
5.5.4.1 ·OH assay.....	141
5.5.4.2 ROS assay.....	141
5.6. Conclusions.....	142
5.7 References.....	143
국문요약	151
Acknowledgement	154

List of Figures

Figure 1.1 Diagrammatic presentation of antibacterial mechanism of action.....	6
Figure 1.2 Diagrammatic presentation of nano-zinc oxide synthesis, characterization, and applications.....	11
Scheme 2.1. Synthesis of Zn(II)-complex (Zn1-3).....	37
Figure 2.1. Single X-ray crystal structure of dichlorobis(2-isopropylimidazole) zinc(II) complex (Zn1).....	41
Figure 2.2. Single X-ray crystal structure of dichlorobis(2-methylbenzimidazole) zinc(II) complex (Zn2).....	41
Figure 2.3. Single X-ray crystal structure of dichlorobis(2-methylbenzoxazole) zinc(II) complex (Zn3).....	42
Figure 2.4. Agarose gel electrophoresis pattern of pDNA in the presence of complexes Zn1–3. Lane 1, DNA control; lane 2, DNA + Zn1 (1 mM); lane 3, DNA + Zn2 (1mM); lane 4, DNA + Zn3 (1 mM).....	44
Figure 2.5. Agarose gel electrophoresis pattern of CTDNA in the presence of the synthesized zinc complexes Zn1-3. Lane 1, CTDNA control; lane 2, DNA + Zn1 (1 mM); lane 3, DNA + Zn2 (1 mM); lane 4, DNA + Zn3 (1 mM).....	44
Figure 2.6: Antioxidant activity of complexes Zn1-3.....	46
Scheme 3.1. Synthesis of Co1-3 from benzazole ligands L1-L3.....	59
Figure 3.1. X-ray structure of dichloro-bis(2-methylbenzimidazole) cobalt(II) Co1.....	61
Figure 3.2. X-ray structure of dichloro-bis(2-methylbenzoxazole)cobalt(II) Co2.....	62
Figure 3.3. X-ray structure of dichloro-bis(2-methylbenzothiazole)cobalt(II) Co3.....	62
Figure 3.4. Kinetics of <i>MRSA</i> membrane crossing by the Co1-3, AMP, and Co1-3 + AMP at $3 \times \text{MIC}$	66
Figure 4.1. FESEM image of (A) ZnO, and (B) MoZnO, particle size distribution of (C) ZnO, and (D) MoZnO.....	86
Figure 4.2. EDX spectrum of MoZnO. EDX spectrum displayed the atomic composition of MoZnO.....	86
Figure 4.3. X-ray diffraction patterns of the (A) ZnO and (B) MoZnO.....	88

Figure 4.4. FT-IR spectra of A) ZnO, Na ₂ MoO ₄ ·2H ₂ O, and MoZnO, B) ZrO ₂ , Na ₂ MoO ₄ ·2H ₂ O, and MoZrO, C) WO ₃ , Na ₂ MoO ₄ ·2H ₂ O, and MoWO, D) ZSrTiO ₃ , Na ₂ MoO ₄ ·2H ₂ O, and MoSrTiO.	90
Figure 4.5. Preliminary anti-algal activity of molybdenum-doped metal oxides at 2 h, 24 h, and 48 h (A) MoZnO, (B) MoZrO ₂ , (C) MoWO ₃ , and (D) MoSrTiO ₃	92
Figure 4.6. Plot of pseudo first order rate versus concentration of molybdenum-doped metal oxides (obtained from preliminary anti-algal activity)	92
Figure 4.7. Growth inhibition of <i>M. aeruginosa</i> by MoZnO with time. (A) Change in pigment of <i>M. aeruginosa</i> suspension. (B) Change in OD680 of <i>M. aeruginosa</i> , and (C) Inhibition rate (%) of <i>M. aeruginosa</i> . Statistical significance (determined by paired t-test) is shown by * = $p < 0.05$, ** = $p < 0.001$, *** = $p < 0.0001$, when compared to control (0).	93
Figure 4. 8. Effect of ZnSO ₄ (1), (MoCl ₅) ₂ (2), ZnO (3), Na ₂ MoO ₄ ·2H ₂ O (4), and their combinations ZnSO ₄ +Na ₂ MoO ₄ ·2H ₂ O (5), ZnO+Na ₂ MoO ₄ ·2H ₂ O (6), ZnSO ₄ +(MoCl ₅) ₂ (7), and ZnO+(MoCl ₅) ₂ (8) on the growth of <i>M. aeruginosa</i> . Statistical significance (determined by paired t-test) is shown by * = $p < 0.05$, ** = $p < 0.001$, when compared to control (0)	94
Figure 4.9. Fluorescence intensity of extracellular ·OH generated at 4 h. C and SC are control groups under open air and shading of <i>M. aeruginosa</i> , and EX and SEX experimental groups under open air and shading of <i>M. aeruginosa</i> . Statistical significance (determined by paired t-test) is shown by *** = $p < 0.0001$, when compared to control (0)	95
Figure 4. 10. ·OH assay under the shading of <i>M. aeruginosa</i> . TA (0.5 mM; 100 mL) was poured in two 250 mL conical flasks. After setting the conical flasks in two 500 mL beaker respectively, the beaker was filled with <i>M. aeruginosa</i> culture. One was labeled as an experimental group (SEX) and another one as the control group (SC)	96
Figure 4.11. Intracellular ROS induced by MoZnO in the <i>M. aeruginosa</i> cells	97
Figure 4. 12. Lipid peroxidation of <i>M. aeruginosa</i> cells at 4 h	98
Figure 4. 13. Optical microscope images of <i>M. aeruginosa</i> cells after incubation with MoZnO up to 4 h: (A) 0 mg/L; (B) 1 mg/L; (C) 2.5 mg/L; (D) 5 mg/L; (E) 10 mg/L	98
Figure 4. 14. SEM images of <i>M. aeruginosa</i> cells after incubation with MoZnO up to 4 h: (A) 0 mg/L; (B) 5 mg/L; (C) 10 mg/L	99
Figure 5.1. FESEM image of Cu-VO (A) low magnification and (B) high magnification, and (C) particle size distribution	127

Figure 5.2. EDX spectrum of Cu-VO	127
Figure 5.3. X-ray diffraction patterns of Cu-VO	130
Figure 5.4. XPS spectra of Cu-VO A) Cu B) V, and C) O	130
Figure 5.5. FT-IR spectra of Cu-VO and KVO_3	131
Figure 5.6. Growth inhibition of <i>M. aeruginosa</i> by Cu-VO	132
Figure 5.7. UV-vis absorbance spectra (A) and % degradation of 50 μ M MB (B) treated with Cu-VO catalyst at different time interval	133
Figure 5.8. Fluorescence intensity of extracellular \cdot OH generated at 4 h.....	134
Figure 5.9. Intracellular ROS induced by Cu-VO in the <i>M. aeruginosa</i> cells ...	135



List of Tables

Table 2.1 Crystallographic data and structure refinement for complexes Zn1–3..	39
Table 2.2 Crystallographic data and structure refinement for complexes Zn1–3..	40
Table 2.3 Crystallographic data and structure refinement for complexes Zn1–3..	40
Table 2.4 MIC values of complexes 1–3 and ligands L1 and L2 in $\mu\text{g/mL}$	43
Table 3.1. Crystallographic data and structure refinement for complexes Co1–3	60
Table 3.2. Comparison of selected bond lengths (\AA) and angles ($^\circ$) of Co1-3.....	60
Table 3.3. Hydrogen bonding of Co1 [\AA and $^\circ$]	61
Table 3.4. MIC ($\mu\text{g/mL}$) values of Co1-3	64
Table 3.5. Synergistic activity of the complexes Co1-3 against MRSA.....	65
Table 4.1. Element proportion analysis of MoZnO	87
Table 4.2. Calculated crystallite size, lattice constants, and microstrain values of ZnO and MoZnO.....	89
Table 4.3. Calculated texture coefficients of MoZnO for the seven main peaks ..	89
Table 4.4. Experimental grouping	107
Table 5.1. Element proportion analysis of Cu-VO	128
Table 5.2. Calculated crystallite size, lattice constants, and microstrain values of Cu-VO	129

List of Abbreviations

AFM	Atomic Force Microscopy
Ag	Silver
AMP	Ampicillin
ARB	Antibiotic resistance bacteria
BG-11	Blue-Green medium
°C	Degree Celsius
C ₆ H ₁₄	Hexane
CFU	Colony forming unit
CH ₃ CN	Acetonitrile
CHL	Chloramphenicol
Cl	Chlorine
cm	Centimeter
Co	Cobalt
CT-DNA	Calf thymus deoxyribonucleic acid
Cu	Copper
d	Duplet
DCM	Dichloromethane
DLS	Dynamic Light Scattering
DMSO	Dimethyl sulfoxide
DPPH	2,2-Diphenyl-1-picrylhydrazyl
EcDNA	<i>E. coli</i> deoxyribonucleic acid
EDS	Energy-dispersive X-ray spectroscopy
eV	Electron volt
FESEM	Field emission scanning electron microscopy
FT-IR	Fourier-transform infrared spectroscopy

$^1\text{H NMR}$	Proton nuclear Magnetic Resonance
H	Hydrogen
h	Hour
K	Kelvin
KAN	Kanamycin
L	Liter
MB	Methylene blue
MCl_2	Metal chloride
MDA	Malondialdehyde
mg	Milligram
MIC	Minimum inhibitory concentration
Min	Minute
mL	Milliliter
mM	Millimolar
Mo	Molybdenum
MoCl_5	Molybdenum pentachloride
mol	mole
MoSrTiO	Molybdenum-doped strontium titanium oxide
MoWO	Molybdenum-doped tungsten oxide
MoZnO	Molybdenum-doped zinc oxide
MoZrO	Molybdenum-doped zirconium oxide
MRSA	Methicillin-Resistant <i>S. aureus</i>
N	Nitrogen
$\text{Na}_2\text{MoO}_4 \cdot 2\text{H}_2\text{O}$	Sodium molybdate dihydrate
NEO	Neomycin
nm	Nanometer

NMO	Nano-metal oxides
NZO	Nano-zinc oxide
O	Oxide
OC	Organometallic compounds
OD	Optical density
·OH	Hydroxyl free radical
PEN	Penicillin
ROS	Reactive oxygen species
s	Singlet
SD	Standard deviation
SE	Standard error
SrTiO ₃	strontium-titanium oxide
STR	Streptomycin
TBA	2-thiobarbituric acid
TCA	Trichloroacetic acid
TEM	Transmission Electron Microscopy
UV	Ultraviolet
UV-VIS	UV-visible spectroscopy
V	Vanadium
v	Volume
V ₂ O ₅	Vanadium pentoxide
w	Weight
XRD	X-ray diffraction
Zn	Zinc
ZnO	zinc oxide
ZnSO ₄	Zinc sulfate

ZrO₂ zirconium oxide

μg Microgram

μL Microliter



Synthesis, Characterization, and Environmental Applications of Organometallic Complexes and Nano-metal Oxides

Sondavid Keshaoraoji Nandanwar

Department of Interdisciplinary Program of Marine Convergence Design

Pukyong National University

Abstract

Environmental pollutants such as bacteria, blooming harmful cyanobacteria, and dye limited the access to fresh drinking water and sanitation, which necessitates the remediation of these pollutants. Increased industrialization, global warming, and high living standards contribute to environmental pollution and pose continuing risks to human health. Bacteria are omnipresent and developed resistance to several antibiotics, which are one of the serious threats to the accomplishment of recent medications. The bloom of harmful cyanobacteria is intensified in water due to global warming and eutrophication. Cyanobacterial bloom produces toxins in water and endangers aquatic life and human health. *Microcystis aeruginosa* is the major bloom-causing freshwater blue-green algae, which contaminate the freshwater by releasing cyanotoxins such as neurotoxins and hepatotoxins. Methylene blue (MB) is used in several industries, and research institutes eventually discharge it in the water. MB contaminated water has several harmful effects on humans. To counter these issues, efficient, easy, and cheap techniques are required. Organometallic complexes (OC) and nano-metal oxides (NMO) could offer boundless scope to mitigate these environmental issues. Hence, an intensive investigation is needed to estimate the potential of OC and NMO for pollution control to help in this unprecedented crisis.

Accordingly, the main objective of this work was to synthesize, characterize, and evaluate antibacterial, anti-algal, and dye degradation activity of OC and NMO. We synthesized six organometallic complexes (dichloro-bis(2-isopropylimidazole)-zinc(II) (**Zn1**), dichloro-bis(2-methylbenzimidazole)-zinc(II) (**Zn2**), dichloro-bis(2-methylbenzoxazole)-zinc(II) (**Zn3**), dichloro-bis(2-methylbenzimidazole)-cobalt(II) (**Co1**), dichloro-bis(2-methylbenzoxazole)-

cobalt(II) (**Co2**), and dichloro-bis(2-methylbenzothiazole)-cobalt(II) (**Co3**) complexes) and two nano-metal oxides (molybdenum doped zinc oxide (**4**) and copper-vanadium oxides (**5**). Complexes **Zn1-3/ Co1-3** was synthesized by mixing metal and ligands at room temperature. Molybdenum doped zinc oxide (**4**) (MoZnO) was synthesized using a dry ball mill method, whereas copper doped vanadium oxide (**5**) using a microwave method. Organometallic complexes were characterized using UV-visible spectroscopy (UV-VIS), ¹H NMR spectroscopy, single X-ray crystallography, and elemental analysis, whereas metal complexes using field emission-scanning electron microscopy (FESEM), Energy-dispersive X-ray spectroscopy (EDS), X-ray diffraction (XRD), and FT-IR spectroscopy. Organometallic complexes (**Zn1-3/ Co1-3**) were applied against Gram-positive and Gram-negative bacteria, including resistant strain. **4** was applied against harmful bloom-forming cyanobacteria and **5** against harmful bloom-forming cyanobacteria and dye, under visible light. The mechanism of action of complexes **Zn1-3/ Co1-3** and nano-metal oxides **4** and **5** were investigated against bacteria, cyanobacteria, and dye, respectively. Sytox green assay was used to find bacteria surface penetration behavior of **Co1-3** alone and in the combination of ampicillin (AMP). ·OH, ROS, and lipid peroxidation assays were performed to find the oxidative degradation mechanism of nano-metal oxides **4** and **5**.

Single crystal X-ray analysis showed that complexes **Zn1-3/ Co1-3** had tetrahedral geometry. XRD analysis of metal oxides indicated the crystalline nature of nano-metal oxides **4** and **5**. The average diameter of nano-metal oxides **4** and **5** obtained by FESEM was 40 nm (**4**) and 150 nm (**5**). **Zn1-3/ Co1-3** was exhibited significant antibacterial activity against all antibiotic susceptible bacteria within a concentration range of 50-200 µg/ml. Complexes **Co1-3** showed high antibacterial activity than complexes **Zn1-3**. The complexes **Co2** and **Co3** were more active against *S. aureus* with the minimum inhibitory concentration (MIC) value of 12.5 µg/mL. The combination of AMP with complexes **Co1-3** increased the antibacterial activity of **Co1-3** against Methicillin-Resistant *S. aureus* strains (MRSA). Interestingly, complexes **Co1-3** alone and in combination with AMP exhibited different antibacterial mechanism of action. Complexes **Co2** and **Co3** in combination with AMP disrupted the MRSA membrane, whereas other complexes did not show such a mechanism of action. Nano-metal oxides **4** and **5** showed anti-algal activity against *M. aeruginosa* with a minimum effective concentration of 1 mg/L and 4 mg/L, respectively. The investigation of the anti-algal mechanism of nano-metal oxides **4** and **5** showed the generation of hydroxyl free radical (·OH) in the BG-11 medium under visible light. ·OH was a highly reactive oxygen species that caused the peroxidation of *M. aeruginosa* lipid membrane and triggered the intracellular ROS level. Nano-metal

oxide **5** showed 93.8% degradation of MB. Overall, the current study demonstrated that the complexes **Zn1-3/ Co1-3** and visible light active nano-metal oxides **4** and **5** could be easily synthesized and employed to control environmental pollutants such as bacteria, cyanobacteria, and dye.



Chapter 1

General Introduction

Water has critical importance for human beings (Zhang et al. 2019). Increased use of unwanted medication, global warming, industrialization, and high living standards contribute to water pollution. Water pollution has a serious impact on human health because water is an easy source of infection. The use of unwanted medicines is increasing among people (Kraemer, Ramachandran, and Perron 2019). The use of medicine is also increased in aquaculture, the food sector, and agriculture. Due to poor regulation, these medicines contaminate water bodies (Kraemer et al. 2019). Aquatic microorganisms such as bacteria gradually develop resistance to these medicines called antibiotic resistance bacteria (ARB). Among the many, 70% of *S. aureus* strains develop resistance to multiple antibiotics. The treatment of these ARB is of serious worry for the researchers (Nnadozie and Odume 2019). Climate change and nutrient enrichment have escalated the growth of bloom-forming toxic-cyanobacteria in freshwater ecosystems (Sotton et al. 2019). These cyanobacteria secrete venomous chemicals, which accumulate in the water bodies. These venomous chemicals can trigger several environmental infections and threaten aquatic life and human health (Rastogi, Madamwar, and Incharoensakdi 2015). Out of many bloom-forming cyanobacteria, *Microcystis aeruginosa* (*M. aeruginosa*) is frequently originated in fresh-water bodies. *M. aeruginosa* secretes venomous chemicals such as neurotoxins and hepatotoxins (Rastogi et al. 2015; Sotton et al. 2019). These venomous chemicals are highly toxic and cause serious concerns about the availability of healthy drinking water. Many industries such as textile, leather, paper, plastics, and research institutes use dyes for coloring their goods and experimental purpose (Bapat et al. 2006; J. Liu et al. 2019). Improper handling of these dyes causes their discharge into the water bodies. These non-biodegradable dyes can cause serious infections to aquatic animals and human beings (Rafatullah et al. 2010). Methylene blue (MB) is used regularly for

dying clothes and in various experiments (Bapat et al. 2006). The regular contact of MB with the eyes produces a burning sensation, which may permanently damage the eyes. It also causes toxicity to the central nervous system, gastrointestinal infections, and brain parenchyma decolorization (Begum et al. 2020). Therefore, the remediation of all these environmental issues has the utmost importance and challenges. To address these issues, organometallic complexes (OC) and nano-metal oxides could offer boundless scope. A deep investigation is required for the estimation of the potential of OC and nano-metal oxides for pollution control to help in this unprecedented crisis.

The present study aimed to develop novel OC and NMO using simple, cheap, and eco-friendly methods such as ball mill, microwave, and thermal methods. We have synthesized and characterized novel chelation-free OC of zinc and cobalt and nano-metal oxides of zinc and vanadium for the treatment of infectious and antibiotic-resistant bacteria, bloom-forming cyanobacteria, and dye degradation. We investigated the effect of various antibiotics on the antibacterial activity of cobalt complexes. Further, we find the mechanism of action of OC and nano-metal oxides.

1.1 Organometallic complexes

Organometallic complexes are the combination of organic ligands and metal, containing no fewer than one carbon-metal bond (Hartinger and Dyson 2009). Coordinate covalent bonds are present between carbon and metal in OC. Due to the presence of coordination bonds, these compounds are also called coordination compounds (Mudi, Usman, and Ibrahim 2015). Also, many OC contains bonds between hetero-atoms of organic parts such as oxygen or nitrogen and metal parts. Various OC is found in humans and plants such as myoglobin, hemoglobin, and chlorophyll. The first synthetic organometallic complex was synthesized by Zeise called Zeise's salt, which contains platinum metal (Hunt 1984). This finding opened the window for the synthesis of many OC of disparate transition metals, for

example, cobalt, nickel, copper, zinc, and cadmium (Nandanwar and Kim 2019). OC has multiple applications such as medicine (Ong and Gasser 2019), reaction catalyst (Herrmann et al. 2001), organic light-emitting diodes (Humbs et al. 1999; Muhammad and Sulaiman 2014), photovoltaic (Kido and Okamoto 2002), photonics and optoelectronics (Arroudj et al. 2017; Popczyk et al. 2019), and biocidal use (Daum 1957), and typically applied for the treatment of cancer (Bertrand and Casini 2014), bacterial (Stringer et al. 2017), and fungal (Parveen et al. 2018) infections. The importance of OC over organic compounds is their mastery to modify coordination number, geometry, and oxidation states. Additionally, metals can control the medicinal properties of organic counterparts by fluctuating net electronic charges of the compound (Pravin and Raman 2013). It indicates that the metal nucleus is present as an essential operational element in an array of synthesized organometallic drugs. Due to the multipurpose synthetic applicability and biological activity of these OC, researchers can design, organize, and implement novel methods for the discovery of novel drugs. OC has mainly developed for anticancer applications e.g. coordination complexes of metal with DNA ligand have been thoroughly researched for the application of effective cancer-curing drug development, elucidating the structure of DNA and its charge transmission ability, and in DNA footprinting (Li, Yang, and Wang 2010). Recently, OC has gained more attention for the development of antibacterial drugs. They own several mechanisms for bacterial growth inhibition and can eliminate antibiotic resistance in pathogenic bacteria (Lewandowski et al. 2017).

Most of the OC used for antibacterial activity have multidentate ligands (Biot et al. 2012). A very few monodentate ligands have been developed for antibacterial activity. It creates a huge gap between the understanding of the antibacterial activity of monodentate and multidentate OC. To fill this gap, we have synthesized and characterized monodentate OC and investigated its antibacterial activity.

1.1.1 Synthesis and characterization of organometallic complexes

The synthesis of OC is depended mainly on the reactivity of ligands. Ligands are of two types monodentate and multidentate ligands. The synthesis of all OC depends on the interactions between metal and ligands, solvents, pH, temperature, and atmospheric gases. Synthesis of OC with monodentate ligands is usually easy and single step (Sondavid K. Nandanwar et al. 2020), compared to multidentate ligands (Yimer 2015). Most of the multidentate ligands have a complex structure and require multiple-step synthesis (Ommenya et al. 2020). Green and chemical synthesis methods are the main approaches for the synthesis of OC. The green method usually involves dry conditions, whereas chemical methods involve the use of organic solvents such as DCM, methanol, and DMSO. The product yield is usually high in chemical synthesis. Gamil et al. (Al-Hazmi et al. 2020) synthesized Schiff's-base complexes of Fe (III), Cu (II), Zn (II), and Ni (II) using the ball mill method. Amit et al. (Yaul et al. 2020) synthesized Schiff's-base complexes under microwave light. Fatemeh et al. (Ghorbani et al. 2020) used the solvent-free synthesis of Cu (II) or Zn (II) Schiff base complexes.

OC is characterized using several methods such as Ultraviolet-visible (UV-vis) spectroscopy, Magnetic Susceptibility Measurements, Fourier Transform Infrared Spectroscopy (FT-IR), Elemental Analysis, Proton nuclear magnetic resonance ($^1\text{H-NMR}$) Spectroscopy, $^{13}\text{C-NMR}$, and Single-Crystal X-ray Diffraction Spectroscopy (Single Crystal XRD).

Ultraviolet-visible analysis of the complexes under the range of $250\text{-}1000\text{ cm}^{-1}$ gives information about ligand field (d-d transitions) and charge transfer between metal and ligand (Vigato and Tamburini 2004). Magnetic susceptibility is used to evaluate the magnetic moments of the complexes. Magnetic moment values are used to determine the hybridization of the complexes. These results indicate the high spin and low spin nature of complexes (Raman, Ravichandran, and Thangaraja 2004). The extent of electron pairing, stereochemistry, and metal-metal interactions

in the complexes can be evaluated using the magnetic moment values. The UV-vis and magnetic moment analysis are beneficial for the estimation of complex geometry. These two methods provide critical information regarding the geometry of Cu(II) and Co(II) OCs (Ahmadi et al. 2013). FT-IR analysis provides information about the types of coordination bonds present in the complexes (Keypour, Salehzadeh, and Parish 2002; Yimer 2014). Due to the coordination of ligand with metal, the electron density of ligands shifted towards metal. The reduction of electron density of ligand decreases the bond strength between the coordinated atom and its neighboring atom. The decreased bond strength minimizes the frequency value of the ligand. The comparison of the FT-IR spectrum of free ligands and their complex gives information about the type and number of coordination present in the complexes. The elemental analysis provides information about the percentage of atoms present in the complexes (Li et al. 2010). Elemental analysis is used to determine the empirical formula of complexes. Proton nuclear magnetic resonance ($^1\text{H-NMR}$) (Rostamizadeh, Daneshfar, and Moghimi 2019) and $^{13}\text{C-NMR}$ (Keypour et al. 2019) spectroscopy provide information about the proton and carbon atoms in the complexes. The change in the spin state of electrons under the applied electric field gives information about the position of hydrogen and carbon in the complexes, which is very useful information to determine the exact geometry of complexes. Single-Crystal X-ray Diffraction Spectroscopy is of utmost importance for the determination of detailed information about the geometry of complexes (Mahmood et al. 2019). We can find detailed information about the geometry, bond length, bond angle, symmetry/ asymmetry, and space group of complexes using Single-Crystal X-ray Diffraction Spectroscopy.

1.1.2 Applications of zinc(II) and cobalt(II) organometallic complexes

Organometallic complexes have broad biological applications (cancer, infectious viruses, fungus, and inflammation treatment). OC was mainly used for cancer treatment (Sun et al. 2015), and later their antibacterial activity was explored.

Antibacterial activity of OC has been studied against diverse bacteria such as *Escherichia coli*, *Staphylococcus aureus*, Methicillin-Resistant *S. aureus*, and *Bacillus subtilis* (Sondavid K. Nandanwar et al. 2020). Recently, the study of antimicrobial activity of synthetic OC is of immense interest among researchers (Abd-El-Aziz, Agatemor, and Etkin 2017). OC has a beneficial medicinal property that extends its importance for multiple biological applications. As a result, synthetic OC appears as an important structural nucleus in different types of antibacterial drugs. OC shows similar antibacterial activity against all Gram-negative and Gram-positive bacteria (Ejidike and Ajibade 2015).

Researchers observed that an OC possesses multiple antibacterial mechanisms, which is of utmost importance to control antibiotic-resistant bacteria (Wenzel et al. 2013). The mechanism of action of OC includes the interruption of critical cellular processes, and mainly concern with the type of metal and ligands. The increment of oxidative stress, protein inactivation, blocking of nucleic acid, and cell wall disruption is the main antibacterial mechanisms of OC (Harrison, Ceri, and Turner 2007; Paladini et al. 2015). The antibacterial mechanism of action of OC is diagrammatically shown in Figure 1.1.

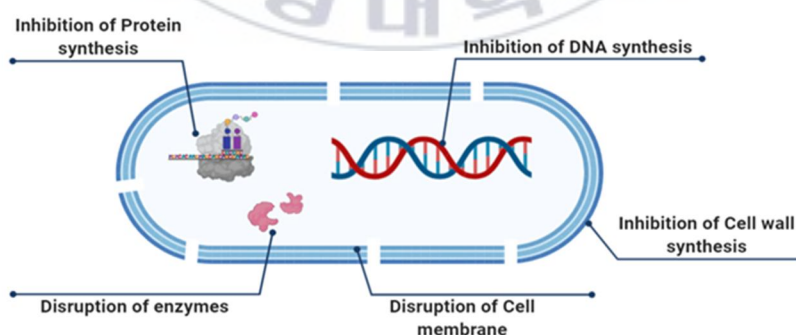


Figure 1.1 Diagrammatic presentation of antibacterial mechanism of action.

Out of many trace metals, zinc ranks 2nd in the human body (Cuevas and Koyanagi 2005; Osredkar 2011). All classes of enzymes show the presence of zinc metal. Zinc is also present in blood, kidney, liver, and bone (Abu Ali et al. 2016). Much research has exposed the antibacterial activity of Zn(II) complexes (Chkirate et al. 2020; Zelenák, Györyová, and Mlynarcík 2001) with less toxicity to normal cells (Taylor et al. 2015). Zinc has comparable antibacterial activity to that of Ag(I) and Cu(II) ions (Singha et al. 2019). Many dental materials such as mouth rinses and toothpaste have antibacterial zinc additive to combat oral cariogenic bacteria *albicans* such as *Streptococcus mutants*, *Actinomyces viscosus*, *Lactobacillus casei*, *Staphylococcus aureus*, and *Candida albicans* (Almoudi et al. 2018; Yakoob et al. 2014). Besides, Zn(II) complexes are applied to combat bacteria such as *Escherichia coli*, *Streptococcus faecalis*, and soil bacteria (Szunyogová et al. 2007). Researchers highly focused on the antibacterial study of chelated Zn(II) complexes than chelation-free Zn(II) complexes. Chelated Zn(II) complexes showed antibacterial activity against *Salmonella typhi*, *Shigella flexneri*, *S. aureus*, *Aeromonas hydrophila*, *Enterococcus faecalis* with MIC value between the range of 50-200 µg/mL (Bharty et al. 2015). Sondavid et al. (Sondavid K Nandanwar et al. 2020) showed that the Zn(II) complexes of monodentate ligands could also show comparable antibacterial activity against Methicillin-Resistant *S. aureus*, *S. aureus*, *E. coli*, *Bacillus subtilis*, *E. faecalis*, *Salmonella typhimurium*, and *Klebsiella pneumonia*.

Since ancient times, the cobalt(II) ion has medicinal importance for the control of microbial growth (Scarpellini et al. 2003). A trace amount of cobalt is present in the human body. It is the main constituent of vitamin B12, which controls *in vivo* DNA synthesis (Moll and Davis 2017). Cobalt(II) is the central metal ion of the corrin ring (Chemaly 2020) and some proteins such as methionine aminopeptidase 2 (Węglarz-Tomczak et al. 2016). Cobalt can alter the medicinal property of some metal-binding drugs (Malik et al. 2018). Based on these properties much

antibacterial cobalt(II) complexes have been synthesized to combat bacterial infections. Maghmi et al. (Maghmi et al. 2015) found that the antibacterial activity of the cobalt(II) complex was similar to complexes of manganese(II), copper(II), nickel(II), and ruthenium(III) complexes. Beheshti et al. (Beheshti et al. 2016) found the poor antibacterial activity of chelated cobalt(II)-azole complexes against *E. coli*, *P. aeruginosa*, *S. aureus*, and *B. subtilis* with MIC value of 400-3000 µg/mL. Researches have focused more on the antibacterial activity of chelated cobalt(II) complexes compared to chelation-free complexes. Sondavid et al. (Sondavid K Nandanwar et al. 2020) showed that the monodentate Co(II)-azole complexes have far better antibacterial activity against Methicillin-Resistant *S. aureus*, *S. aureus*, *E. coli*, *Bacillus subtilis*, *E. faecalis*, *Salmonella typhimurium*, and *Klebsiella pneumonia* with MIC value of 12.5 µg/mL. This comparison revealed the importance of chelation-free cobalt(II) for medicinal applications.

1.2 Nano-metal oxides

Nanotechnology is the study of technology and science at the nanoscale. It denotes the scientific principles and new assets that can be originated and mastered when working in the nano range. Nanoparticles are smaller particles with sizes range from 1-100 nm (Sharma, Tiwari, and Dixit 2015). In Greek Nanos mean 'dwarf'. Nano-size is one-billionth of a meter (10^9 m) or equal to the size of about ten water molecules or 6 carbon atoms. The size of the RBC is about 7000 nm. The nano-metal oxide has higher reactivity than the same metal oxide of micro size. The physical and chemical properties of the same metal oxide change with a change in size from bulk to the nanoscale. At nanoscale metal, oxides have reduced melting temperature, high surface to volume ratio, improved optical properties, and improved conductivity (Singh et al. 2016). Nano-metal oxides (NMO) are enticing the attention of researchers as it can be synthesized in different size and shapes for various applications such as batteries (Chavali and Nikolova 2019), photovoltaic cells (Chavali and Nikolova 2019), energy conversion (Chavali and Nikolova 2019),

photo-catalysis, pharmaceutical (Mirzaei and Darroudi 2017), and cosmetic industries (Mirzaei and Darroudi 2017). For example, a nano-zinc oxide is used for UV protection, medication, cosmetics and concrete, antimicrobial agent, and pollution control.

Nano-metal oxide with a narrow bandgap 2-4 eV is significant for photocatalytic applications (Millan et al. 2014). The photocatalyst is a light-active NMO, which has high efficiency for the absorption of light photons. Most of the NMO are UV light active with a bandgap of more than 3 eV. Sunlight contains 5% UV light and 40% visible light. Therefore, visible light active NMO is highly important than a UV light active NMO. The doping of UV light active NMO with metals and nonmetals can reduce the bandgap of parent material (Y. Liu et al. 2019). Out of s, p, d, and f block metal, d block metals are most usually used to reduce the bandgap of parent NMO (Wang et al. 2014). Metal dopants improve the electron transition from the valence band to the conduction band, boosting the electrical performance of NMO (Du et al. 2014). Molybdenum doping in zinc oxide improves the antifungal activity of the zinc oxide (Sondavid Nandanwar et al. 2020).

1.2.1 Methods for synthesis of nano-metal oxides

Nano-chemistry comprises the design and synthesis of novel NMO (Chavali and Nikolova 2019). Several methods and techniques are developed for the synthesis of novel NMO. Top-down and bottom-up are two general methods for the fabrication of NMO. The top-down method includes the use of bulk metal oxide for the synthesis of NMO (Medhi, Marquez, and Lee 2020). The top-down method takes away upper coatings of bulk metal oxide for the synthesis of NMO, for example, mask etching. In this method, one cannot control the shape and size of the NMO. A bottom-up method initiates at the atomic level in which one can control the shape and size of the NMO. In the bottom-up methods, the oxidizing and reducing agents are used with a pristine metal salt, which controls the growth and size of metal salt up to the nano level. For example, the QDs or nanoparticles could

be synthesized from the colloidal dispersion of its metal salts (Chavali and Nikolova 2019).

The bottom-up method is subdivided into the physical method and the chemical method. Physical methods include physical vapor deposition, chemical vapor deposition, pulsed laser deposition, atomic layer deposition, molecular beam epitaxy, spray pyrolysis. Chemical methods are hydrothermal, precipitation, microemulsion, sol-gel, microwave, sonochemical, electrochemical, and photochemical methods. These physical and chemical methods are expensive, labor-intensive, and detrimental to the environment (Wilson 2018).

All these methods involve the use of toxic solvents such as methanol, which is injurious to health and the environment. The suitable methods for NMO synthesis are aqueous and solvent-free methods such as ball milling and microwave methods. Regarding these issues, we have synthesized molybdenum doped zinc oxide (MoZnO) and copper doped vanadium oxide (Cu-VO) using dry ball milling and water-mediated microwave methods.

1.2.2 Characterization of nano-metal oxides

The characterization of NMO involves the use of numerous techniques. However, the alteration of color during the progress of the reaction is the primary qualitative signal for NMO synthesis. During the synthesis of MoZnO, the typical color change is from pink to brown and colorless to yellow for Cu-VO (Seabold and Neale 2015) due to the synthesis of colored products. Typically, NMO is characterized using Ultraviolet-visible (UV-vis) Spectrophotometer (Becheri et al. 2008), Dynamic Light Scattering (DLS) (Balraj et al. 2017), Field Emission Scanning Electron Microscopy (FESEM) (Azizi et al. 2014), Transmission Electron Microscopy (TEM) (Becheri et al. 2008), Energy Dispersive X-ray Spectroscopy (EDX), X-ray Powder Diffraction (XRD) (Becheri et al. 2008), Fourier Transform Infrared Spectroscopy (FT-IR) (Becheri et al. 2008), Atomic

Force Microscopy (AFM) (Balraj et al. 2017), and Zeta potential measurement (Balraj et al. 2017).

Ultraviolet-visible Spectrophotometer works based on the wavelength absorbed by the NMO. The colorless NMO absorbs UV light (190-380 nm), whereas visible light (380-800 nm) is absorbed by colored NMO; it is characteristically useful for inspection of NMO synthesis. DLS is used to determine NMO surface charges and size distribution in a liquid medium. The size, shape, and morphology of NMO are determined by SEM, TEM, and AFM. Specifically, TEM analysis gives information about the size and shape distribution, while SEM analysis is about the shape and morphology of NMO. EDX is used to determine atomic% of NMO, and XRD for diffraction pattern identification and crystal structure of the NMO. The Bragg's reflection of nano-ZnO are (100), (002), (101), (102), (110), (103), (200), (112), and (201). FT-IR is used to determine the types of bonding present in NMO. The ion leaching from NMO is analyzed by measuring zeta potential, which gives information about the colloidal stability of NMO. Schematic presentation of NMO synthesis using the ball mill method with its characterization and applications in different fields is presented in Figure 1.2.

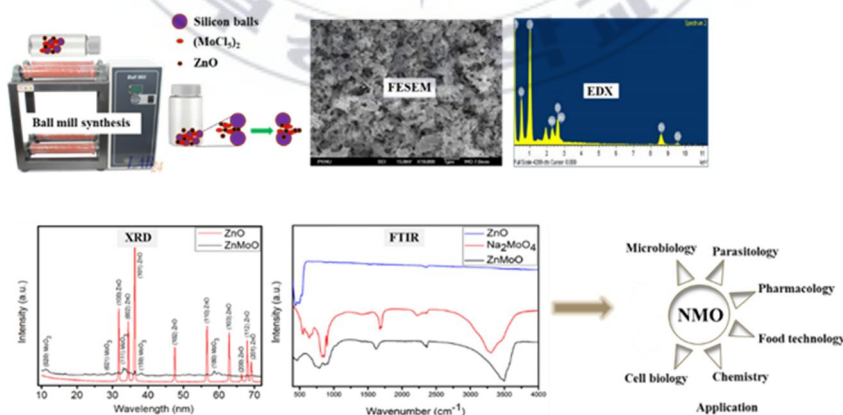


Figure 1.2 Diagrammatic presentation of nano-zinc oxide synthesis, characterization, and applications.

1.2.3 Applications of NMO

Over the past few years, researchers have performed an immense effort for the development of effective NMO to control environmental pollution. NMO catalyzes the reaction only under the light is called photocatalyst. Photocatalyst absorbs light and provides such energy to a reacting substance to make a chemical reaction occur. The photoactive NMO has been studied for the abatement of algae, microbes, dye, and drugs (Alavi and Nokhodchi 2020; Sirelkhatim et al. 2015). Under light radiation, photoactive NMO produces free radicals such as hydroxyl radicals ($\cdot\text{OH}$) and reactive oxygen species (ROS). $\cdot\text{OH}$ and ROS are extremely reactive oxidizing species, which can oxidize almost every type of cell. These results in the peroxidation of cell lipid membranes (Kiwi and Nadtochenko 2004), deprivation of cell walls and EPS (Linkous et al. 2000), and degradation of whole cells (Linkous et al. 2000). NMO has a broad effective surface, which enhances the speed of photocatalytic reaction. $\cdot\text{OH}$ can also oxidize all types of dye pollutants. NMO has limitless catalytic efficiency with long-term reactivity.

Anti-algal activity of nano-zinc oxide: Nano-zinc oxide (NZO) has been widely used for biological applications such as anti-algal activity (Halbus, Horozov, and Paunov 2020). Visible light comprises a major percentage of net sunlight. NZO has high activity under UV light and less activity under visible light due to its wide bandgap (3.2 eV). Under UV light, it generates pairs of electrons and holes. The fast recombination of electrons and holes decreases the reactivity of NZO. Researchers used strategies to synthesize visible light active NZO with fewer electrons and holes pairs recombination, which increases its catalytic efficiency. For example, doping of NZO with metal and nonmetal can narrow down bandgap and reduce electrons and holes pairs recombination. The metal-doped NZO has high biological activity such as antialgal activity under visible light. Thus metal-doped NZO can be applied for the control of toxic algae. Shariati et al. (Shariati et al. 2018) compared the anti-algal activity of pristine NZO and indium-doped zinc

oxide. Indium doped zinc oxide showed strong anti-algal than NZO under visible light. Molybdenum doped zinc oxide showed very high anti-algal activity than NZO under visible light (Sondavid Nandanwar et al. 2020).

Dye degradation activity of nano-vanadium oxide: Vanadium pentoxide (V₂O₅) is an efficient *n*-type semiconductor photocatalyst for the degradation of organic pollutants due to its benign nature, high chemical and light stability, and visible light activity (Jayaraj et al. 2018). V₂O₅ showed poor degradation efficiency towards methylene blue dye (Jayaraj et al. 2018). Fabrication of metal oxide composites of V₂O₅ is an effective strategy for the improvement of degradation efficiency towards methylene blue dye (Zelege and Kuo 2019). Recently, visible light active transition metal/vanadium composites have been intensively investigated for various applications such as dye degradation (Suresh et al. 2014). Cobalt doped vanadium oxide showed high methylene blue degradation efficiency than vanadium oxide (Ghiyasiyan-Arani, Masjedi-Arani, and salvation-Niasari 2016). Nickel doped vanadium oxide showed high rhodamine B degradation efficiency than vanadium oxide (Rafique et al. 2020).

1.3 Purpose of this work

In this study we attempted to synthesize novel non-chelated organometallic complexes of zinc(II) and cobalt(II) and semiconductor photocatalysts MoZnO and Cu-VO using facile, benign, and cheap method for the removal of antibiotic-resistant bacteria, toxin producing freshwater algae, and industrial waste.

Part I,

Chapter 2. focuses on the facile synthesis of zinc(II)azole complexes and evaluation of their antibacterial and antioxidant activities.

Chapter 3. focuses on the facile synthesis of cobalt(II) benzazole complexes and evaluation of their antibacterial mechanism of action.

Part II,

Chapter 4. focuses on the ball mill synthesis of molybdenum doped zinc oxide and evaluation of their anti-algal mechanism.

Chapter 5. focuses on the microwave assisted synthesis of Cu-VO and evaluation of their anti-algal and dye removal mechanism.

All of the results supports that synthesized OC are able to remove bacteria, and nano-metal oxides are efficient to remove cyanobacteria and dye from their medium under visible light.



1.4 References

- Abd-El-Aziz, Alaa S., Christian Agatemor, and Nola Etkin. 2017. "Antimicrobial Resistance Challenged with Metal-Based Antimicrobial Macromolecules." *Biomaterials* 118:27–50.
- Abu Ali, Hijazi, Suhad N. Omar, Mohanad D. Darawsheh, and Hadeel Fares. 2016. "Synthesis, Characterization and Antimicrobial Activity of Zinc(II) Ibuprofen Complexes with Nitrogen-Based Ligands." *Journal of Coordination Chemistry* 69(6):1110–22.
- Ahmadi, R. A., F. Hasanvand, G. Bruno, H. A. Rudbari, and S. Amani. 2013. "Synthesis, Spectroscopy, and Magnetic Characterization of Copper(II) and Cobalt(II) Complexes with 2-Amino-5-Bromopyridine as Ligand." *Russian Journal of Coordination Chemistry/Koordinatsionnaya Khimiya* 39(12):867–71.
- Al-Hazmi, Gamil A. A., Khlood S. Abou-Melha, Nashwa M. El-Metwaly, Ismail Althagafi, Fathy Shaaban, and Rania Zaky. 2020. "Green Synthesis Approach for Fe (III), Cu (II), Zn (II) and Ni (II)-Schiff Base Complexes, Spectral, Conformational, MOE-Docking and Biological Studies." *Applied Organometallic Chemistry* 34(3):1–15.
- Alavi, Mehran, and Ali Nokhodchi. 2020. "An Overview on Antimicrobial and Wound Healing Properties of ZnO Nanobiofilms, Hydrogels, and Bionanocomposites Based on Cellulose, Chitosan, and Alginate Polymers." *Carbohydrate Polymers* 227(September 2019):115349.
- Almoudi, Manal Mohamed, Alaa Sabah Hussein, Mohamed Ibrahim Abu Hassan, and Nurhayati Mohamad Zain. 2018. "A Systematic Review on Antibacterial Activity of Zinc against Streptococcus Mutans." *Saudi Dental Journal* 30(4):283–91.
- Arroudj, S., A. Aamoum, L. Messaadia, A. Bouraiou, S. Bouacida, K. Bouchouit,

- and B. Sahraoui. 2017. "Effect of the Complexation on the NLO Electronic Contribution in Film Based Conjugated Quinoline Ligand." *Physica B: Condensed Matter* 516(January):1–6.
- Azizi, Susan, Mansor B. Ahmad, Farideh Namvar, and Rosfarizan Mohamad. 2014. "Green Biosynthesis and Characterization of Zinc Oxide Nanoparticles Using Brown Marine Macroalga *Sargassum Muticum* Aqueous Extract." *Materials Letters* 116:275–77.
- Balraj, B., N. Senthilkumar, C. Siva, R. Krithikadevi, A. Julie, I. Vetha Potheher, and M. Arulmozhi. 2017. "Synthesis and Characterization of Zinc Oxide Nanoparticles Using Marine *Streptomyces* Sp. with Its Investigations on Anticancer and Antibacterial Activity." *Research on Chemical Intermediates* 43(4):2367–76.
- Bapat, Prashant, Subir Kumar Nandy, Pramod Wangikar, and K. V. Venkatesh. 2006. "Quantification of Metabolically Active Biomass Using Methylene Blue Dye Reduction Test (MBRT): Measurement of CFU in about 200 S." *Journal of Microbiological Methods* 65(1):107–16.
- Becheri, Alessio, Maximilian Dürr, Pierandrea Lo Nostro, and Piero Baglioni. 2008. "Synthesis and Characterization of Zinc Oxide Nanoparticles: Application to Textiles as UV-Absorbers." *Journal of Nanoparticle Research* 10(4):679–89.
- Begum, Robina, Jawayria Najeeb, Ayesha Sattar, Khalida Naseem, Ahmad Irfan, Abdullah G. Al-Sehemi, and Zahoor H. Farooqi. 2020. "Chemical Reduction of Methylene Blue in the Presence of Nanocatalysts: A Critical Review." *Reviews in Chemical Engineering* 36(6):749–70.
- Beheshti, Azizolla, Forough Safaeiyan, Faeze Hashemi, Hossein Motamedi, Peter Mayer, Giuseppe Bruno, and Hadi Amiri Rudbari. 2016. "Synthesis, Structural Characterization, Antibacterial Activity and Computational Studies of New

- Cobalt (II) Complexes with 1,1,3,3-Tetrakis (3,5-Dimethyl-1-Pyrazolyl)Propane Ligand.” *Journal of Molecular Structure* 1123:225–37.
- Bertrand, Benoît, and Angela Casini. 2014. “A Golden Future in Medicinal Inorganic Chemistry: The Promise of Anticancer Gold Organometallic Compounds.” *Dalton Trans.* 43(11):4209–19.
- Bharty, M. K., R. K. Dani, P. Nath, A. Bharti, N. K. Singh, Om Prakash, Ranjan K. Singh, and R. J. Butcher. 2015. “Syntheses, Structural and Thermal Studies on Zn(II) Complexes of 5-Aryl-1,3,4-Oxadiazole-2-Thione and Dithiocarbamates: Antibacterial Activity and DFT Calculations.” *Polyhedron* 98:84–95.
- Biot, Christophe, William Castro, Cyrille Y. Botté, and Maribel Navarro. 2012. “Small Organometallic Compounds as Antibacterial Agents.” *Dalton Transactions* 41(21):6335–49.
- Chavali, Murthy S., and Maria P. Nikolova. 2019. “Metal Oxide Nanoparticles and Their Applications in Nanotechnology.” *SN Applied Sciences* 1(6):1–30.
- Chemaly, Susan M. 2020. “Use of ^{13}C and ^1H NMR to Determine the Structure of the Diastereomeric Cobalt Corrinoids Aquacyanocobinamide and Aquacyanocobester.” *Polyhedron* 175:114203.
- Chkirate, Karim, Khalid Karrouchi, Necmi Dege, Nada Kheira Sebbar, Abdelaziz Ejjoumany, Smaail Radi, N. N. Adarsh, Ahmed Talbaoui, Marilena Ferbinteanu, El Mokhtar Essassi, and Yann Garcia. 2020. “Co(Ii) and Zn(Ii) Pyrazolyl-Benzimidazole Complexes with Remarkable Antibacterial Activity.” *New Journal of Chemistry* 44(6):2210–21.
- Cuevas, Luis E., and Ai Koyanagi. 2005. “Zinc and Infection: A Review.” *Annals of Tropical Paediatrics* 25(3):149–60.
- Daum, Richard J. 1957. “A G R I C U L T U R A L A N D B I O C I D A L APPLICATIONS OF *Annals New York Academy of Sciences.*”

- Du, Jian, Xin liang Chen, Cai chi Liu, Jian Ni, Guo fu Hou, Ying Zhao, and Xiao dan Zhang. 2014. "Highly Transparent and Conductive Indium Tin Oxide Thin Films for Solar Cells Grown by Reactive Thermal Evaporation at Low Temperature." *Applied Physics A: Materials Science and Processing* 117(2):815–22.
- Ejidike, Ikechukwu P., and Peter A. Ajibade. 2015. "Synthesis, Characterization and Biological Studies of Metal(II) Complexes of (3E)-3-[(2-{(E)-[1-(2,4-Dihydroxyphenyl) Ethylidene]Amino}ethyl)Imino]-1-Phenylbutan-1-One Schiff Base." *Molecules* 20(6):9788–9802.
- Ghiyasiyan-Arani, Maryam, Maryam Masjedi-Arani, and Masoud salavati-Niasari. 2016. "Size Controllable Synthesis of Cobalt Vanadate Nanostructures with Enhanced Photocatalytic Activity for the Degradation of Organic Dyes." *Journal of Molecular Catalysis A: Chemical* 425:31–42.
- Ghorbani, Fatemeh, Hamzeh Kiyani, Seied Ali Pourmousavi, and Davood Ajloo. 2020. "Solvent-Free Synthesis of 1-Amidoalkyl-2-Naphthols Using Magnetic Nanoparticle-Supported 2-(((4-(1-Iminoethyl)Phenyl)Imino)Methyl)Phenol Cu (II) or Zn (II) Schiff Base Complexes." *Research on Chemical Intermediates* 46(6):3145–64.
- Halbus, Ahmed F., Tommy S. Horozov, and Vesselin N. Paunov. 2020. "Surface-Modified Zinc Oxide Nanoparticles for Antialgal and Antiyeast Applications." *ACS Applied Nano Materials* 3(1):440–51.
- Harrison, Joe J., Howard Ceri, and Raymond J. Turner. 2007. "Multimetal Resistance and Tolerance in Microbial Biofilms." *Nature Reviews Microbiology* 5(12):928–38.
- Hartinger, Christian G., and Paul J. Dyson. 2009. "Bioorganometallic Chemistry—from Teaching Paradigms to Medicinal Applications." *Chem. Soc. Rev.*

38(2):391–401.

Herrmann, Wolfgang A., Volker P. W. Bo, Christian W. K. Gsto, Manja Grosche, Claus-peter Reisinger, and Thomas Weskamp. 2001. “Synthesis, Structure and Catalytic Application of Palladium(II) Complexes Bearing.” *Journal of Organometallic Chemistry* 618:616–28.

Humbs, Werner, Emile Van Veldhoven, Hong Zhang, and Max Glasbeek. 1999. “Sub-Picosecond Fluorescence Dynamics of Organic Light-Emitting Diode Tris(8-Hydroxyquinoline) Metal Complexes.” *Chemical Physics Letters* 304(1–2):10–18.

Hunt, L. B. 1984. “The First Organometallic Compounds WILLIAM CHRISTOPHER ZEISE.” *Platinum Metals Review* 28(2):76–83.

Jayaraj, Santhosh Kumar, Vishwanathan Sadishkumar, Thirumurugan Arun, and Paramasivam Thangadurai. 2018. “Enhanced Photocatalytic Activity of V₂O₅ Nanorods for the Photodegradation of Organic Dyes: A Detailed Understanding of the Mechanism and Their Antibacterial Activity.” *Materials Science in Semiconductor Processing* 85(April):122–33.

Keypour, Hassan, Fatemeh Forouzandeh, Sadegh Salehzadeh, Farshid Hajibabaei, S. Feizi, Roya Karamian, N. Ghiasi, and Robert William Gable. 2019. “DNA Binding Studies and Antibacterial Properties of a New Schiff Base Ligand Containing Homopiperazine and Products of Its Reaction with Zn(II), Cu(II) and Co(II) Metal Ions: X-Ray Crystal Structure of Cu(II) and Zn(II) Complexes.” *Polyhedron* 170:584–92.

Keypour, Hassan, Sadegh Salehzadeh, and R. V. Parish. 2002. “Synthesis of Two Potentially Heptadentate (N₄O₃) Schiff-Base Ligands Derived from Condensation of Tris(3-Aminopropyl)-Amine and Salicylaldehyde or 4-Hydroxysalicylaldehyde. Nickel(II) and Copper(II) Complexes of the Former

- Ligand.” *Molecules* 7(2):140–44.
- Kido, Junji, and Yoshi Okamoto. 2002. “Organo Lanthanide Metal Complexes for Electroluminescent Materials.” *Chemical Reviews* 102(6):2357–68.
- Kiwi, J., and V. Nadtochenko. 2004. “New Evidence for TiO₂ Photocatalysis during Bilayer Lipid Peroxidation.” *Journal of Physical Chemistry B* 108(45):17675–84.
- Kraemer, Susanne A., Arthi Ramachandran, and Gabriel G. Perron. 2019. “Antibiotic Pollution in the Environment: From Microbial Ecology to Public Policy.” *Microorganisms* 7(6):1–24.
- Lewandowski, Eric M., Łukasz Szczupak, Stephanie Wong, Joanna Skiba, Adam Guśpiel, Jolanta Solecka, Valerije Vrček, Konrad Kowalski, and Yu Chen. 2017. “Antibacterial Properties of Metallocenyl-7-ADCA Derivatives and Structure in Complex with CTX-M β -Lactamase.” *Organometallics* 36(9):1673–76.
- Li, Yong, Zheng-Yin Yang, and Ming-Fang Wang. 2010. “Synthesis, Characterization, DNA Binding Properties, Fluorescence Studies and Antioxidant Activity of Transition Metal Complexes with Hesperetin-2-Hydroxy Benzoyl Hydrazone.” *Journal of Fluorescence* 20(4):891–905.
- Linkous, C. A., G. J. Carter, D. V. Locuson, A. J. Ouellette, D. K. Slattery, and L. A. Smitha. 2000. “Photocatalytic Inhibition of Algae Growth Using TiO₂, WO₃, and Cocatalyst Modifications.” *Environmental Science and Technology* 34(22):4754–58.
- Liu, Junli, Yuhan Wang, Jianzhong Ma, Yi Peng, and Ai Qin Wang. 2019. “A Review on Bidirectional Analogies between the Photocatalysis and Antibacterial Properties of ZnO.” *Journal of Alloys and Compounds* 783:898–918.

- Liu, Yu, Wei Wang, Xiaomin Xu, Jean Pierre Marcel Veder, and Zongping Shao. 2019. "Recent Advances in Anion-Doped Metal Oxides for Catalytic Applications." *Journal of Materials Chemistry A* 7(13):7280–7300.
- Maghami, Mahboobeh, Faezeh Farzaneh, Jim Simpson, Mina Ghiasi, and Mohammad Azarkish. 2015. "Synthesis, Crystal Structure, Antibacterial Activity and Theoretical Studies on a Novel Mononuclear Cobalt(II) Complex Based on 2,4,6-Tris(2-Pyridyl)-1,3,5-Triazine Ligand." *Journal of Molecular Structure* 1093:24–32.
- Mahmood, Khalid, Waleed Hashmi, Hammad Ismail, Bushra Mirza, Brendan Twamley, Zareen Akhter, Isabel Rozas, and Robert J. Baker. 2019. "Synthesis, DNA Binding and Antibacterial Activity of Metal(II) Complexes of a Benzimidazole Schiff Base." *Polyhedron* 157:326–34.
- Malik, Manzoor Ahmad, Ovas Ahmad Dar, Parveez Gull, Mohmmad Younus Wani, and Athar Adil Hashmi. 2018. "Heterocyclic Schiff Base Transition Metal Complexes in Antimicrobial and Anticancer Chemotherapy." *MedChemComm* 9:409–36.
- Medhi, Riddhiman, Maria D. Marquez, and T. Randall Lee. 2020. "Visible-Light-Active Doped Metal Oxide Nanoparticles: Review of Their Synthesis, Properties, and Applications." *ACS Applied Nano Materials* 3(7):6156–85.
- Millan, Jose, Philippe Godignon, Xavier Perpina, Amador Perez-Tomas, and Jose Rebollo. 2014. "A Survey of Wide Bandgap Power Semiconductor Devices." *IEEE Transactions on Power Electronics* 29(5):2155–63.
- Mirzaei, Hamed, and Majid Darroudi. 2017. "Zinc Oxide Nanoparticles: Biological Synthesis and Biomedical Applications." *Ceramics International* 43(1):907–14.
- Moll, Rachel, and Bernard Davis. 2017. "Iron, Vitamin B12 and Folate." *Medicine (United Kingdom)* 45(4):198–203.

- Mudi, S. Y., M. T. Usman, and S. Ibrahim. 2015. "Clinical and Industrial Application of Organometallic Compounds and Complexes: A Review." *American Journal of Chemistry and Applications* 2(6):151–58.
- Muhammad, Fahmi Fariq, and Khaulah Sulaiman. 2014. "Optical and Morphological Modifications in Post-Thermally Treated Tris(8-Hydroxyquinoline) Gallium Films Deposited on Quartz Substrates." *Materials Chemistry and Physics* 148(1–2):473–77.
- Nandanwar, Sondavid K, Shweta B. Borkar, Bryan Nathanael, Enkhnarayan Bayarra, Lei Lottice, and Anne Piad. 2020. "Synthesis and Characterization of Novel Chelation-Free Zn (II) -Azole Complexes: Evaluation of Antibacterial , Antioxidant and DNA Binding Activity." 59(May):589–97.
- Nandanwar, Sondavid K., Shweta B. Borkar, Bryan Nathanael Wijaya, Jeong Hyung Cho, Naresh H. Tarte, and Hak Jun Kim. 2020. "Cobalt(II) Benzazole Derivative Complexes: Synthesis, Characterization, Antibacterial and Synergistic Activity." *ChemistrySelect* 5(11):3471–76.
- Nandanwar, Sondavid K., and Hak Jun Kim. 2019. "Anticancer and Antibacterial Activity of Transition Metal Complexes." *ChemistrySelect* 4(5):1706–21.
- Nandanwar, Sondavid, Myung Won Lee, Shweta Borkar, Jeong Hyung Cho, Naresh H. Tarte, and Hak Jun Kim. 2020. "Synthesis, Characterization, and Anti-Algal Activity of Molybdenum-Doped Metal Oxides." *Catalysts* 10(7):805.
- Nnadozie, Chika F., and Oghenekaro Nelson Odume. 2019. "Freshwater Environments as Reservoirs of Antibiotic Resistant Bacteria and Their Role in the Dissemination of Antibiotic Resistance Genes." *Environmental Pollution* 254:113067.
- Ommenya, F. K., E. A. Nyawade, D. M. Andala, and J. Kinyua. 2020. "Synthesis,

- Characterization and Antibacterial Activity of Schiff Base, 4-Chloro-2- $\{(E)-[(4\text{-Fluorophenyl})\text{Imino}]\text{Methyl}\}$ phenol Metal (II) Complexes.” *Journal of Chemistry* 2020.
- Ong, Yih Ching, and Gilles Gasser. 2019. “Organometallic Compounds in Drug Discovery: Past, Present and Future.” *Drug Discovery Today: Technologies* xxx(xx):8–10.
- Osredkar, Josko. 2011. “Copper and Zinc, Biological Role and Significance of Copper/Zinc Imbalance.” *Journal of Clinical Toxicology* s3(01).
- Paladini, Federica, Mauro Pollini, Alessandro Sannino, and Luigi Ambrosio. 2015. “Metal-Based Antibacterial Substrates for Biomedical Applications.” *Biomacromolecules* 16(7):1873–85.
- Parveen, Humaira, Raedah Aiyed Suliman Alatawi, Meshari A. Alsharif, Mohammed Issa Alahmdi, Sayeed Mukhtar, Salman Ahmad Khan, Sadaf Hasan, and Asad U. Khan. 2018. “Novel Pyrazoline-Based Organometallic Compounds Containing Ferrocenyl and Quinoline Units: Synthesis, Characterization and Microbial Susceptibilities.” *Applied Organometallic Chemistry* 32(4):1–8.
- Popczyk, Anna, Aouatif Aamoum, Anna Migalska-Zalas, Przemyslaw Płóciennik, Anna Zawadzka, Jaroslaw Mysliwiec, and Bouchta Sahraoui. 2019. “Selected Organometallic Compounds for Third Order Nonlinear Optical Application.” *Nanomaterials* 9(2):1–15.
- Pravin, Narayanaperumal, and Natarajan Raman. 2013. “DNA Interaction and Antimicrobial Activity of Novel Tetradentate Imino-Oxalato Mixed Ligand Metal Complexes.” *Inorganic Chemistry Communications* 36:45–50.
- Rafatullah, Mohd, Othman Sulaiman, Rokiah Hashim, and Anees Ahmad. 2010. “Adsorption of Methylene Blue on Low-Cost Adsorbents: A Review.” *Journal*

of Hazardous Materials 177(1–3):70–80.

Rafique, Muhammad, Muhammad Hamza, Muhammad Shakil, Muneeb Irshad, Muhammad Bilal Tahir, and Mohammad Reda Kabli. 2020. “Highly Efficient and Visible Light–Driven Nickel–Doped Vanadium Oxide Photocatalyst for Degradation of Rhodamine B Dye.” *Applied Nanoscience (Switzerland)* 10(7):2365–74.

Raman, N., S. Ravichandran, and C. Thangaraja. 2004. “Copper(II), Cobalt(II), Nickel(II) and Zinc(II) Complexes of Schiff Base Derived from Benzil-2,4-Dinitrophenylhydrazone with Aniline.” *Journal of Chemical Sciences* 116(4):215–19.

Rastogi, Rajesh P., Datta Madamwar, and Aran Incharoensakdi. 2015. “Bloom Dynamics of Cyanobacteria and Their Toxins: Environmental Health Impacts and Mitigation Strategies.” *Frontiers in Microbiology* 6(NOV):1–22.

Rostamizadeh, Shahnaz, Zahra Daneshfar, and Hamid Moghimi. 2019. “Synthesis of Sulfamethoxazole and Sulfabenzamide Metal Complexes; Evaluation of Their Antibacterial Activity.” *European Journal of Medicinal Chemistry* 171:364–71.

Scarpellini, Marciela, Ademir Neves, Rosmari Hörner, Adailton J. Bortoluzzi, Bruno Szpoganics, César Zucco, René A. Nome Silva, Valderes Drago, Antônio S. Mangrich, Wilson A. Ortiz, Wagner A. C. Passos, Maurício C. B. De Oliveira, and Hernán Terenzi. 2003. “Phosphate Diester Hydrolysis and DNA Damage Promoted by New Cis-Aqua/Hydroxy Copper(II) Complexes Containing Tridentate Imidazole-Rich Ligands.” *Inorganic Chemistry* 42(25):8353–65.

Seabold, Jason A., and Nathan R. Neale. 2015. “All First Row Transition Metal Oxide Photoanode for Water Splitting Based on Cu₃V₂O₈.” *Chemistry of*

Materials 27(3):1005–13.

Shariati, Mohsen, Arasteh Mallakin, Fatemeh Malekmohammady, and Fariba Khosravi-Nejad. 2018. “Inhibitory Effects of Functionalized Indium Doped ZnO Nanoparticles on Algal Growth for Preservation of Adobe Mud and Earthen-Made Artworks under Humid Conditions.” *International Biodeterioration and Biodegradation* 127(October 2017):209–16.

Sharma, Kumar A., Arun Kumar Tiwari, and Amit Rai Dixit. 2015. “Mechanism of Nanoparticles Functioning and Effects in Machining Processes: A Review.” *Materials Today: Proceedings* 2(4–5):3539–44.

Singh, Purushottam Kumar, Pankaj Kumar, Manowar Hussain, Alok Kumar Das, and Ganesh Chandra Nayak. 2016. “Synthesis and Characterization of CuO Nanoparticles Using Strong Base Electrolyte through Electrochemical Discharge Process.” *Bulletin of Materials Science* 39(2):469–78.

Singha, Priyadarshini, Christina D. Workman, Jitendra Pant, Sean P. Hopkins, and Hitesh Handa. 2019. “Zinc-Oxide Nanoparticles Act Catalytically and Synergistically with Nitric Oxide Donors to Enhance Antimicrobial Efficacy.” *Journal of Biomedical Materials Research - Part A* 1425–1433.

Sirelkhatim, Amna, Shahrom Mahmud, Azman Seeni, Noor Haida Mohamad Kaus, Ling Chuo Ann, Siti Khadijah Mohd Bakhori, Habsah Hasan, and Dasmawati Mohamad. 2015. “Review on Zinc Oxide Nanoparticles: Antibacterial Activity and Toxicity Mechanism.” *Nano-Micro Letters* 7(3):219–42.

Sotton, Benoît, Alain Paris, Séverine Le Manach, Alain Blond, Charlotte Duval, Qin Qiao, Arnaud Catherine, Audrey Combes, Valérie Pichon, Cécile Bernard, and Benjamin Marie. 2019. “Specificity of the Metabolic Signatures of Fish from Cyanobacteria Rich Lakes.” *Chemosphere* 226:183–91.

Stringer, Tameryn, Ronnett Seldon, Nicole Liu, Digby F. Warner, Christina Tam,

- Luisa W. Cheng, Kirkwood M. Land, Peter J. Smith, Kelly Chibale, and Gregory S. Smith. 2017. "Antimicrobial Activity of Organometallic Isonicotinyl and Pyrazinyl Ferrocenyl-Derived Complexes." *Dalton Trans.* 9875–85.
- Sun, Dongdong, Weiwei Zhang, Endong Yang, Nuan Li, Haiping Liu, and Weiyun Wang. 2015. "Investigation of Antibacterial Activity and Related Mechanism of a Ruthenium(II) Polypyridyl Complex." *Inorganic Chemistry Communications* 56:17–21.
- Suresh, R., K. Giribabu, R. Manigandan, S. Munusamy, S. Praveen Kumar, S. Muthamizh, A. Stephen, and V. Narayanan. 2014. "Doping of Co into V2O5 Nanoparticles Enhances Photodegradation of Methylene Blue." *Journal of Alloys and Compounds* 598:151–60.
- Szunyogová, Erika, Dagmar Mudroňová, Katarína Györyová, Radomíra Nemcová, Jana Kovářová, and Lenka Píknová-Findoráková. 2007. "The Physicochemical and Biological Properties of Zinc(II) Complexes." *Journal of Thermal Analysis and Calorimetry* 88(2):355–61.
- Taylor, Kathryn M., Francesca Solfa, Arwyn T. Jones, Helen L. Wiggins, Andrew D. Westwell, Stephen E. Hiscox, and Jennifer M. Wymant. 2015. "Disulfiram-Induced Cytotoxicity and Endo-Lysosomal Sequestration of Zinc in Breast Cancer Cells." *Biochemical Pharmacology* 93(3):332–42.
- Vigato, Pietro Alessandro, and Sergio Tamburini. 2004. "The Challenge of Cyclic and Acyclic Schiff Bases and Related Derivatives." *Coordination Chemistry Reviews* 248(17-20 SPEC. ISS.):1717–2128.
- Wang, Yaqin, Ruirui Zhang, Jianbao Li, Liangliang Li, and Shiwei Lin. 2014. "First-Principles Study on Transition Metal-Doped Anatase TiO₂." 1–8.
- Węglarz-Tomczak, Ewelina, Małgorzata Burda-Grabowska, Mirosław Giurg, and

Artur Mucha. 2016. "Identification of Methionine Aminopeptidase 2 as a Molecular Target of the Organoselenium Drug Ebselen and Its Derivatives/Analogues: Synthesis, Inhibitory Activity and Molecular Modeling Study." *Bioorganic and Medicinal Chemistry Letters* 26(21):5254–59.

Wenzel, Michaela, Malay Patra, Christoph Helmut Rudi Senges, Ingo Ott, Jennifer Janina Stepanek, Antonio Pinto, Pascal Prochnow, Cuong Vuong, Sina Langklotz, Nils Metzler-Nolte, and Julia Elisabeth Bandow. 2013. *Analysis of the Mechanism of Action of Potent Antibacterial Hetero-Tri-Organometallic Compounds: A Structurally New Class of Antibiotics*. Vol. 8.

Wilson, Niki. 2018. "Nanoparticles: Environmental Problems or Problem Solvers?" *BioScience* 68(4):241–46.

Yakoob, Javed, Zaigham Abbas, Muhammad Waqas Usman, Safia Awan, Shagufta Naz, Fatima Jafri, Saeed Hamid, and Wasim Jafri. 2014. "Comparison of Antimicrobial Activity of Zinc Chloride and Bismuth Subsalicylate against Clinical Isolates of *Helicobacter Pylori*." *Microbial Drug Resistance* 20(4):305–9.

Yaul, Amit Ramdasji, Sarika Ramdasji Yaul, Jagannath Tulshiram Makode, Nilesh Govindrao Salunkhe, and Avinash Avdhutrao Ramteke. 2020. "Transition Metal Complexes Incorporating with Unsymmetrical N₂O₂-Donor Schiff Base Ligand: Microwave-Assisted Synthesis, Spectroscopic, Thermal, and Biological Aspects." *Macromolecular Symposia* 392(1):1–8.

Yimer, Ali Mohammed. 2014. "Chemical Synthesis, Spectral Characterization and Antimicrobial Studies on Complexes of Ni (II), Cu (II) and Zn (II) with N, N-Di (o-Hydroxybenzenoylmethylene) Ethylenediamine." *American Journal of BioScience* 2(2):22–34.

Yimer, Ali Mohammed. 2015. "Review on Preparation and Description of Some

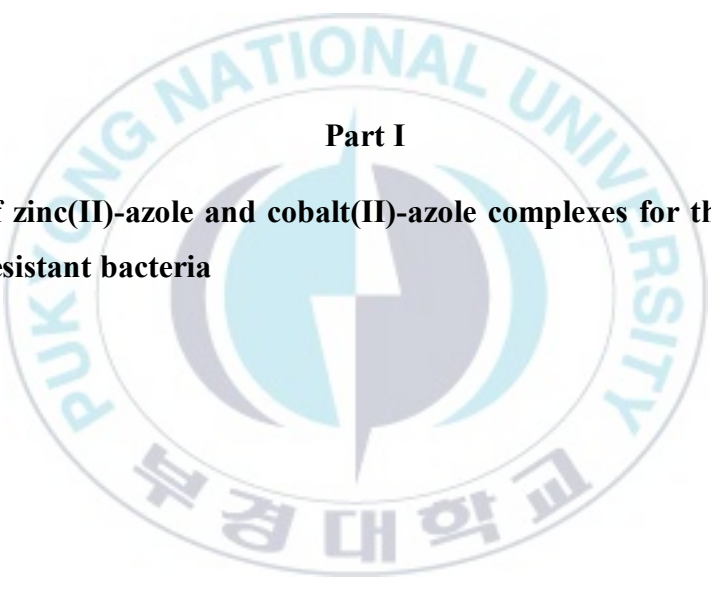
First Series Divalent Transition Metal Complexes with Novel Schiff's Base Ligands." *Review of Catalysts* 2(1):14–25.

Zelege, Misganaw Alemu, and Dong Hau Kuo. 2019. "Synthesis and Application of V₂O₅-CeO₂ Nanocomposite Catalyst for Enhanced Degradation of Methylene Blue under Visible Light Illumination." *Chemosphere* 235:935–44.

Zelenák, V., K. Györyová, and D. Mlynarcík. 2001. "Antibacterial and Antifungal Activity of Zinc(II) Carboxylates with/without N-Donor Organic Ligands." *Metal-Based Drugs* 8(5):269–74.

Zhang, Chi, Yi Li, Danmeng Shuai, Yun Shen, Wei Xiong, and Linqiong Wang. 2019. "Graphitic Carbon Nitride (g-C₃N₄)-Based Photocatalysts for Water Disinfection and Microbial Control: A Review." *Chemosphere* 214:462–79.





Part I

Synthesis of zinc(II)-azole and cobalt(II)-azole complexes for the removal of antibiotic resistant bacteria

Chapter 2

Synthesis and characterization of novel chelation-free Zn(II)-azole complexes: Evaluation of antibacterial, antioxidant and DNA binding activity

2.1 Abstract

In this study, the single-step synthesis of non-chelated Zn(II)-complexes (**Zn1-Zn3**) [ZnCl_2L_2] of non-chelating ligands with L= 2-isopropylimidazole (**L1**), 2-methylbenzimidazole (**L2**), and 2-methylbenzoxazole (**L3**) had been proposed at room temperature. The characterization of **Zn1-Zn3** using UV-Vis spectroscopy, $^1\text{H-NMR}$ spectroscopy, single X-ray crystallography, and elemental analysis confirmed their non-chelated nature. Antibacterial assay disclosed the higher bacteria inhibition efficiency of **Zn1-Zn3** against tested bacteria with minimum inhibitory concentration (MIC) of 100-200 $\mu\text{g/ml}$ than non-chelating ligands. Out of all tested bacteria, **Zn1-Zn3** efficiently inhibited the growth of methicillin-resistant staphylococcus aureus (MRSA). The DNA binding assay revealed that **Zn1-Zn3** could strongly interact with the nucleic acid of bacteria resulting in nonfunctional DNA. Bacteria cannot survive with nonfunctional DNA and eventually die. The induction of nonfunctional DNA may be a plausible antibacterial mechanism of **Zn1-Zn3**. In addition, the good antioxidant activity of **Zn1-Zn3** indicated their anti-inflammatory property. This study disclosed the antibacterial and anti-inflammatory activity of **Zn1-Zn3**, which could be beneficial for advanced biological studies in the future.

2.2 Introduction

The use of unwanted pharmaceutical drugs among peoples and for agricultural works is rapidly increasing. The improper handling of unused drugs leads to their accumulation in water. The microorganism such as bacteria developed resistance to these drugs called antibiotic-resistant bacteria, which is a serious concern for aquatic life and humans (Nandanwar and Kim 2019). Nowadays, the infection due to multidrug-resistant *Staphylococcus aureus* (MRSA)(Kavanagh et al. 2018) is most common among patients and poses challenge for chemists. MRSA is extremely infectious bacteria, causing serious infections to skin and soft tissue, necrotizing pneumonia and death (Moghnieh et al. 2017)³. Out of several beta-lactam antibiotics such as cloxacillin, MRSA developed resistant to erythromycin, clindamycin, aminoglycosides, fluoroquinolones, rifampicin, and cotrimoxazole (Thabit et al. 2019). The development of novel antibacterial compounds is very important to combat these issues.

The nonchelating azole compounds occupy an important position in drug development due to their presence in natural components such as deoxyribonucleic acid, hemoglobin, histidine, Vitamin B12, and histamine (Fodor et al. 2016). Azoles are the vital building-block for the synthesis of antifungal drugs such as ketoconazole, itraconazole, and fluconazole (Leonardi et al. 2018). Out of various azoles, imidazole derivatives occupy the first position for the fabrication of drugs such as antibacterial, anti-inflammatory, antidepressant, antitubercular, anticancer, antileishmanial, and antiviral (Kim et al. 2013). Current research reports revealed the use of imidazolium derivatives after imidazole for the fabrication of novel antibacterial drugs to combat antibiotic-resistant bacteria (Wu et al. 2017; Zheng et al. 2016). To improve the efficiency of existed azole drugs, researchers are coordinating azoles with metal ions. The metal ion is an electron acceptor and can reduce the negative charge

around the azole nucleus to increase cell penetration efficiency of azoles (Bello-Vieda et al. 2018; Bharty et al. 2015).

Zinc is a well-known ancient antibacterial remedy with poor toxicity to mammalian cells (Taylor et al. 2015). Zinc is analogous to famous antibacterial agents silver and copper metals (Singha et al. 2019). The key antibacterial player of the metals is their respective ions released into the solution. Zinc(II) ion has been used in many commercial products, such as toothpaste to sunglasses. Zinc(II) ion has unique antibacterial activity and UV light absorbing properties to protect humans from bacteria and harmful radiations. Zinc(II) ion has strong antibacterial activity against *albicans*, an oral cariogenic bacterium such as *Streptococcus mutants*, *Actinomyces viscosus*, *Lactobacillus casei*, *Staphylococcus aureus*, and *Candida albicans* (Almoudi et al. 2018; Yakoob et al. 2014).

After the discovery of cisplatin, many nonchelated metal complexes of platinum and ruthenium have been developed for anticancer activity. These compounds were tested for antibacterial activity. Due to their high cost and low availability, researchers focused on other metal complexes containing chelating ligands. Many chelated Zn(II)-azole complexes have been tested against antibiotic-resistant strains such as MRSA (Ashraf et al. 2016; Indoria et al. 2016). In the race of developing novel antibacterial agents, researchers ignored the nonchelated metal complexes, resulting in a huge gap in finding novel antibiotics. A literature review showed that no nonchelated Zn(II)-azole complexes have been studied so far for the inhibition of bacteria. In humans, carboxypeptidase-A is a nice example of a biocompatible nonchelated Zn(II)-histidine complex (Vančo et al. 2015). Based on these results, we hypothesized that synthetic nonchelated Zn(II)-azole moieties could be a good antibacterial agent without any injurious effects on humans (Butler et al. 2018).

Most of the antibacterial agents block the functioning nucleic acid of bacteria to combat bacterial infections. Some OC also showed DNA disruption as an

antibacterial mechanism (Papadopoulos et al. 2017). Based on these researches, we hypothesized that DNA disruption could be the antibacterial mechanism of synthesized nonchelated Zn(II)-complexes. Thus, a DNA binding assay of synthesized Zn(II)-complexes was performed against EcDNA and CT-DNA. Additionally, to test their biocompatibility, we performed a free radical scavenging assay as various Zn(II)-complexes showed better antioxidant activities (Devi et al. 2019).



2.3 Materials and Methods

Chemicals used in this work are Zn(II) chloride, 2-isopropylimidazole, 2-methyl benzimidazole, and 2-methyl-benzoxazole, dichloromethane (DCM), acetonitrile, diethyl ether, n-hexane, methanol, DMSO, and dimethylformamide.

2.3.1 General method for the synthesis of complexes:

Metal salts (MCl_2) and ligands (L1-L4) were added in a 1:2 molar ratio into two 100 mL round bottom flasks each. Twenty mL of DCM was added to each flask and kept for stirring at room temperature. After 10 min ligand solution was dropped slowly into metal salt suspension. The stirring was continued for 15 min at room temperature to react the ligands with MCl_2 (scheme 1). The obtained crystal was filtered and washed with DCM for the removal of unreacted ligands. Excess DCM was vaporized using a rotary evaporator and obtained thick solution was air-dried. Obtained product was purified and recrystallized using C_6H_{14} and CH_3CN , respectively. Further, it was characterized by UV-Vis analysis, 1H NMR, elemental analysis, and Single-X-Ray crystallography analysis.

Dichlorobis(2-isopropylimidazole)zinc(II) complex (Zn1): % Yield: 72% (White crystal). Anal. Calcd. for $C_{12}H_{20}N_4Cl_2Zn$ (356.61); C, 40.42; H, 5.65; N, 15.71; Cl, 19.88; Zn, 18.34. Found: C, 40.63; H, 5.44; N, 15.82; Cl, 19.76; Zn, 18.56%. 1H NMR δ 1.24 (6H, d, $J = 6.7$ Hz), 3.01 (1H, sept, $J = 6.7$ Hz), 7.16 (1H, d, $J = 3.3$ Hz), 7.24 (1H, d, $J = 3.3$ Hz). UV-Vis (DMSO) λ_{max} , nm ($\log \epsilon$, $L \text{ mol}^{-1} \text{ cm}^{-1}$): 287 (2.53).

Dichlorobis(2-methylbenzimidazole)zinc(II) complex (Zn2): Yield: 85% (White crystal). Anal. Calcd. For $C_{32}H_{32}Cl_2N_8Zn$ (664.94); C, 57.8; H, 4.85; N, 16.85; Cl, 10.66; Zn, 9.83. Found C, 57.56; H, 4.68; N, 16.58; Cl, 10.48; Zn, 9.62%. 1H NMR – 2.06 (3H, s), 7.20 – 7.15 (4H, ddd), 7.63 (1H, s). UV-Vis (DMSO) λ_{max} , nm ($\log \epsilon$, $L \text{ mol}^{-1} \text{ cm}^{-1}$): 288 (2.49).

Dichlorobis(2-methyl benzoxazole)zinc(II) complex (Zn3): Yield: 64% (White crystal). Anal. Calcd. For $C_{16}H_{14}Cl_2N_2O_2Zn$ (402.59); C, 47.73; H, 3.5; N, 6.96; O, 7.95; Cl, 17.61; Zn, 16.24. Found C, 47.83; H, 7.72; N, 6.78; O, 9.68; Cl, 17.55;

Zn, 16.29%. ¹H NMR - 2.07 - 2.04 (3H, s), 7.58 - 7.42 (2H, 7.32(ddd, J = 8.0, 7.8, 1.6 Hz), 7.37(ddd, J = 8.1, 7.8, 1.8 Hz)), 7.73 - 7.68 (1H, ddd, J = 8.1, 1.6, 0.5 Hz), 8.23 - 8.15 (1H, ddd, J = 8.0, 1.8, 0.5 Hz). UV-Vis (DMSO) λ_{max}, nm (logε, L mol⁻¹ cm⁻¹): 289 (2.71).

2.3.2 Antibacterial assay

The minimum concentration of drugs restricting the visible growth of bacteria is defined as minimum inhibitory concentration. A two-fold serial dilution method was used to perform bacterial growth inhibition assay. The test compounds used were **Zn1-3**, **L1**, and **L2**, and streptomycin (antibiotic control). Two-fold serially diluted solutions of test compounds were prepared 1% DMSO using a standard protocol (Ghosh, Igamberdiev, and Debnath 2018). Hundred μL inoculum of overnight grown Gram-positive bacteria (methicillin-resistant *Staphylococcus aureus* (MRSA), *Staphylococcus aureus*, *Bacillus subtilis*, and *Enterococcus faecalis*) and Gram-negative bacteria (*Escherichia coli*, *Klebsiella pneumonia*, and *Salmonella typhimurium*) at 37 °C was mixed with 100 μL of diluted test solutions in sterile 96 well plate. The final concentration of test compounds and bacteria was 1.562 to 200 μg/mL and ~2 × 10⁵ CFU mL⁻¹. The control of bacteria, %DMSO, and water was used to eliminate background values. These plates were incubated at 37 °C, and the optical density (OD) of the plates was recorded at 650 nm after 18 h. MIC of the test compounds was calculated by subtracting the OD of blank from the OD of the sample.

2.3.3 DNA mobility shift assays

Plasmid DNA was isolated from transformed *E. coli* PET25b using a DNA spin Plasmid DNA purification kit. 16 μg of EcDNA and 0.08 mM CT-DNA (calf thymus DNA) were treated with 1 mM **Zn1-3** solution and incubated at 25 °C for 1 h. The reaction was ended by mixing loading buffer, consisting of 0.25% bromophenol blue, 0.25% xylene cyanol FF, and 30% (v/v) glycerol in water. The electrophoresis of the resulting mixture was performed on agarose gels (0.8% w/v) at low voltage. The gels were visualized in the presence of UV light.

2.3.4 Antioxidant assay

Antioxidant assay of **Zn1-3** was performed according to the known procedure with a slight variation (Li et al. 2014). The standard methanol solution of DPPH ($OD_{517} = \sim 0.416$) was mixed with **Zn1-3** and rutin in a 1:1 ratio and incubated in a dark for 5 hours. An OD_{517} of the resulting solution was measured after 5 h. Antioxidant of various concentrations were calculated using the following equation:

$$\text{Percent inhibition of DPPH radical} = ([A_i - A_f] / A_i) \times 100$$

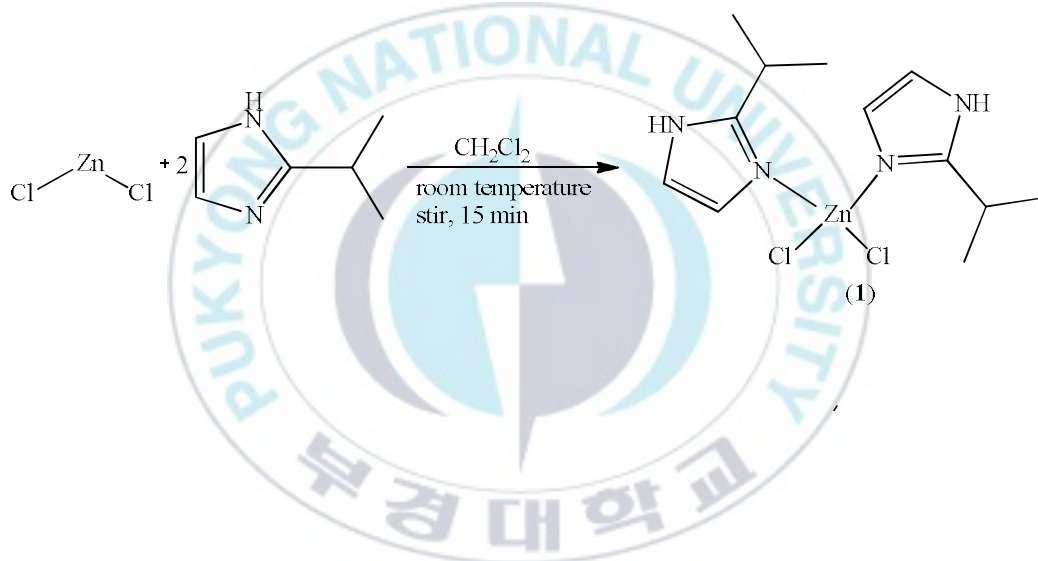
Where A_i and A_f were the absorbance at time zero and 5 h.



2.4 Results and discussion

2.4.1 Synthesis of Zn1-3

Zn1-3 was synthesized using facile procedure and in single step at room temperature. **Zn1-3** has high solubility in 1% DMSO. Literature study showed the preparation of **Zn1-3** with simple ligands was fast, simple, single step, cheap, and energy saving than the Schiff base and chelated azole Zn(II)-complexes (A et al. 2014; Mcginley et al. 2013; Tarte et al. 2008; Vijayakumar et al. 2019). Further, structural elucidation of **Zn1-3** was done by UV-Vis spectroscopy, ¹H-NMR spectroscopy, single X-ray crystallography, and elemental analysis.



Scheme 2.1. Synthesis of Zn(II)-complex (**Zn1-3**).

2.4.2 Molecular structures of Zn(II)-complexes Zn1-3

The single X-ray crystal structures of **Zn1-3** were shown in Figs. 1-3, respectively. The crystallographic data and refinement parameters of **Zn1-3** were summarized in Table 2.1. The coordination geometry around **Zn1-3** was distorted tetrahedral analogous to previously reported Co(II)-complexes (Singh et al. 2017).

The appropriate bond distances and angles of complexes **Zn1-3** were listed in Table 2.2. The hydrogen bonding in complex **Zn1** and **Zn2** was listed in Table 2.3. The crystal structure of **Zn1-3** were orthorhombic, monoclinic, and triclinic, respectively. **Zn1** showed inter-molecular hydrogen bonding between amine hydrogen of one of the 2-isopropylimidazole of first complex and with chlorine atom of another complex N(2)-H(2A)...Cl(1). This indicated that hydrogen bonding in complex **Zn1** offered extra stability to the crystal structure in solid state. **Zn2** displayed three inter-molecular H-bonding, one of which was between amine hydrogen of one of benzimidazole of first complex molecule and nitrogen atom of neighboring benzimidazole ligand N(2)-H(2A)...N(5) and vice versa. Second H-bonding was between the amine hydrogen of benzimidazole ligand and one of the chlorine atoms of first complex N(6)-H(6A)...Cl(1), while third H-bonding was between the iminium hydrogen of the benzimidazole ligand and chlorine atom of first complex [N(7)-H(7A)...Cl(2)#2]. This designated that in **Zn2** each monomer was connected with two neighboring benzimidazole ligands *via* inter-molecular H-bonding providing high stability to the crystal structure in solid state.

Furthermore, N-Zn-N bond angles in **Zn1-3** were 115.91 °, 104.95 °, and 98.61 °, respectively. Cl-Zn-Cl bond angle of **Zn1-3** were 109.74 °, 108.35 °, and 114.19 °, respectively. The suitable reason for higher N-Zn-N bond angle in **Zn1** compared to **Zn2** and **Zn3** could be the repulsion between two bulkier isopropyl substituents. The moderate N-Zn-N bond angle in **Zn2** compared to **Zn1** and **Zn3** may be due to the presence of inter molecular hydrogen bonding with benzimidazole ligands. Bond angle between Cl-Zn-Cl in **Zn1** and **Zn2** was less than **Zn3**, which may be the result of steric hindrance between their respective ligands (2-isopropylimidazole and 2-methylbenzimidazole). **Zn3** had no steric hindrance between 2-methylbenzoxazole. Both Zn-N bond lengths in **Zn1** [1.9980 Å] are symmetric, while that of **Zn2** [2.0176(18) Å and 2.0283(18) Å], and **Zn3** [2.0642(15) Å and 2.0646(16) Å] were more asymmetric. The density of **Zn1-3** was 1.425 mg/m³, 1.349 mg/m³ and 1.595 mg/m³, respectively. The space group of

Zn1-3 were Pbcn, P2(1)/n and P-1, respectively. These results indicated that **Zn1-3** had different nucleation mechanism.

Table 2.1 Crystallographic data and structure refinement for complexes **Zn1-3**

Complexes	Zn1	Zn2	Zn3
Empirical formula	C ₆ H ₁₀ Cl N ₂ Zn _{0.50}	C ₃₂ H ₃₂ Cl ₂ N ₈ Zn	C ₁₆ H ₁₄ Cl ₂ N ₂ O ₂ Zn
Formula weight	178.29	664.93	402.56
Temperature	298(1) K	296(2) K	296(1) K
Wavelength	0.71073 Å	0.71073 Å	0.71073 Å
Crystal system	Orthorhombic	Monoclinic	Triclinic
Space group	Pbcn	P2(1)/n	P-1
Unit cell dimension	a = 11.1941 Å, α = 90° b = 11.3578 Å, β = 90° c = 13.0719 Å, γ = 90°	a = 9.6964 Å, α = 90° b = 22.0789 Å, β = 97.5710° c = 15.424 Å, γ = 90°	a = 6.6357 Å, α = 85.5930° b = 10.3514 Å, β = 79.4650° c = 12.9200 Å, γ = 73.9100°
Volume	1661.97(6) Å ³	3273.46(11) Å ³	838.00(4) Å ³
Z	8	4	2
Density (calculated)	1.425 mg/m ³	1.349 mg/m ³	1.595 mg/m ³
Absorption coefficient	1.792 mm ⁻¹	0.948 mm ⁻¹	1.793 mm ⁻¹
F(000)	736	1376	408
Crystal size	0.22 x 0.16 x 0.12 mm ³	0.25 x 0.20 x 0.10 mm ³	0.38 x 0.38 x 0.20 mm ³
Theta range for data collection	2.99 to 30.12°	1.84 to 28.28°	1.60 to 28.29°
Index ranges	0 ≤ h ≤ 15, 0 ≤ k ≤ 16, 0 ≤ l ≤ 18	-12 ≤ h ≤ 12, 0 ≤ k ≤ 29, 0 ≤ l ≤ 20	-8 ≤ h ≤ 8, -13 ≤ k ≤ 13, 0 ≤ l ≤ 17
Reflections collected	2423	8094	4132
Independent reflections	2423 [R(int) = 0.0000]	8094 [R(int) = 0.0000]	4132 [R(int) = 0.0000]
Completeness to theta = 28.28°	98.8 %	99.8 %	99.3 %
Absorption correction	Multi-scan	Multi-scan	Multi-scan
Max. and min. transmission	0.8137 and 0.6939	0.9111 and 0.7974	0.7156 and 0.5490
Refinement method	Full-matrix least-squares on F ²	Full-matrix least-squares on F ²	Full-matrix least-squares on F ²
Data / restraints /	2423 / 0 / 87	8094 / 0 / 388	4132 / 0 / 211

parameters			
Goodness-of-fit on F^2	1.042	1.034	1.081
Final R indices [$I > 2\sigma(I)$]	R1 = 0.0365, wR2 = 0.0970	R1 = 0.0463, wR2 = 0.1207	R1 = 0.0283, wR2 = 0.0754
R indices (all data)	R1 = 0.0567, wR2 = 0.1074	R1 = 0.0694, wR2 = 0.1351	R1 = 0.0314, wR2 = 0.0794
Largest diff. peak and hole	0.834 and -0.249 e.Å ⁻³	0.740 and -0.293 e.Å ⁻³	0.368 and -0.404 e.Å ⁻³

Table 2.2 Comparison of selected bond lengths (Å) and angles (°) for **Zn1–3**.

Zn1	Zn2	Zn3
Zn(1)-N(1) - 1.9980(16)	Zn(1)-N(1) - 2.0176(18)	Zn(1)-N(2) - 2.0642(15)
Zn(1)-N(1)#1 - 1.9980(16)	Zn(1)-N(3) - 2.0283(18)	Zn(1)-N(1) - 2.0646(16)
Zn(1)-Cl(1) - 2.2598(5)	Zn(1)-Cl(1) - 2.2480(7)	Zn(1)-Cl(2) - 2.2147(5)
Zn(1)-Cl(1)#1 - 2.2599(5)	Zn(1)-Cl(2) - 2.2721(7)	Zn(1)-Cl(1) - 2.2282(5)
N(1)-Zn(1)-N(1)#1 - 115.91(9)	N(1)-Zn(1)-N(3) - 104.95(8)	N(2)-Zn(1)-N(1) - 98.61(6)
N(1)-Zn(1)-Cl(1) - 109.50(5)	N(1)-Zn(1)-Cl(1) - 109.47(6)	N(2)-Zn(1)-Cl(2) - 115.56(5)
N(1)#1-Zn(1)-Cl(1) - 106.07(4)	N(3)-Zn(1)-Cl(1) - 113.79(5)	N(1)-Zn(1)-Cl(2) - 109.93(5)
N(1)-Zn(1)-Cl(1)#1 - 106.07(4)	N(1)-Zn(1)-Cl(2) - 112.56(6)	N(2)-Zn(1)-Cl(1) - 105.81(4)
N(1)#1-Zn(1)-Cl(1)#1 - 109.50(5)	N(3)-Zn(1)-Cl(2) - 107.77(6)	N(1)-Zn(1)-Cl(1) - 111.69(5)
Cl(1)-Zn(1)-Cl(1)#1 - 109.74(3)	Cl(1)-Zn(1)-Cl(2) - 108.35(3)	Cl(2)-Zn(1)-Cl(1) - 114.19(2)

Table 2.3 Hydrogen bonds for complex **Zn1** and **Zn2** [Å and °].

Complex	D-H...A	d(D-H)	d(H...A)	d(D...A)	<(DHA)
1^a	N(2)-H(2A)...Cl(1)#2	0.86	2.51	3.357(19)	166.6
2^b	N(2)-H(2A)...N(5)	0.86	2.01	2.826(3)	157.7
	N(4)-H(4A)...N(8)#1	0.86	1.98	2.810(3)	161.5
	N(6)-H(6A)...Cl(1)#2	0.86	2.55	3.366(2)	159.2
	N(7)-H(7A)...Cl(2)#2	0.86	2.40	3.251(2)	170.3

Symmetry transformations used to generate equivalent atoms:

a = #1 -x, y, -z+1/2 #2 -x+1/2, y-1/2, z

b = #1 x-1, y, z #2 -x+1/2, y+1/2, -z+3/2

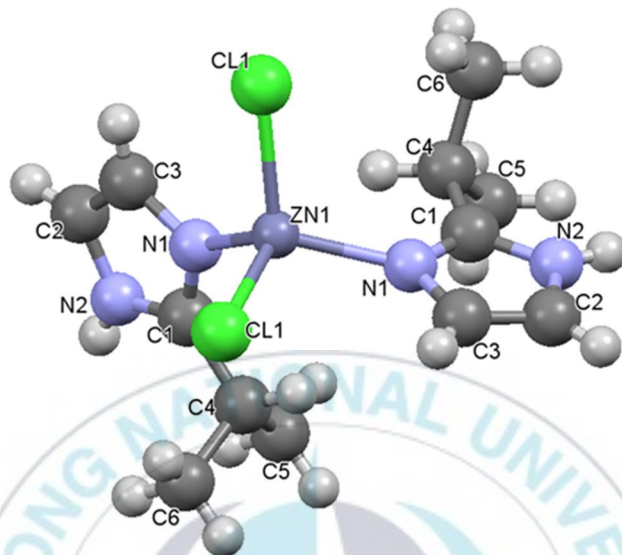


Figure 2.1. Single X-ray crystal structure of dichlorobis(2-isopropylimidazole)zinc(II) complex (**Zn1**).

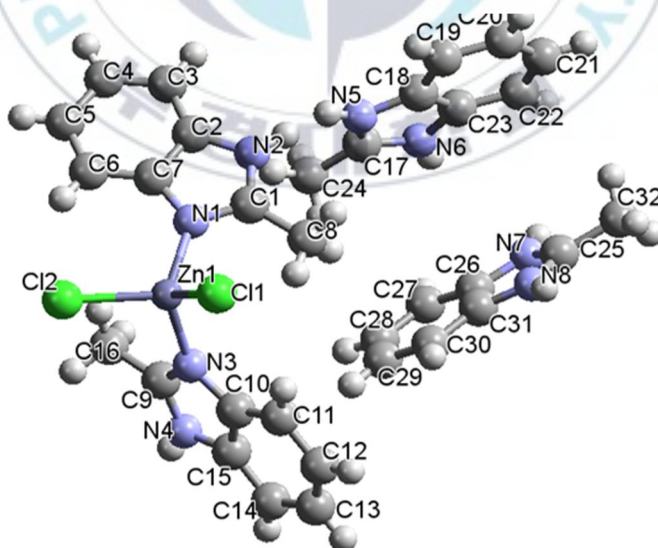


Figure 2.2. Single X-ray crystal structure of dichlorobis(2-methylbenzimidazole)Zn(II) complex (**Zn2**).

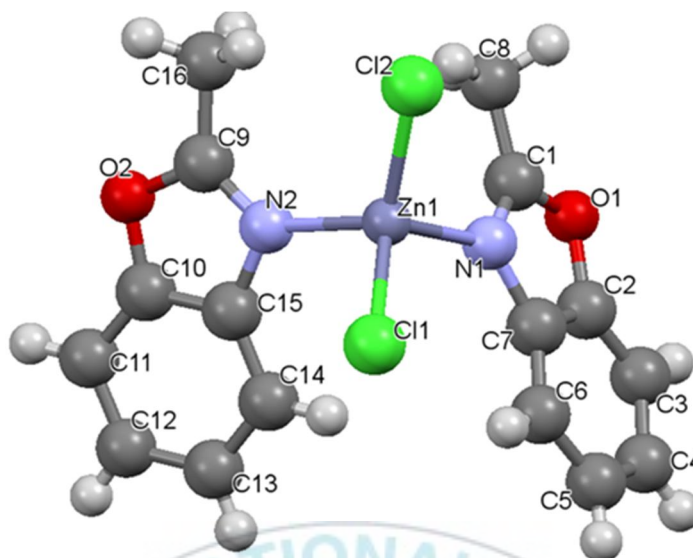


Figure 2.3. Single X-ray crystal structure of dichlorobis(2-methylbenzoxazole)Zn(II) complex (**Zn3**).

2.4.3 Antibacterial activity

The antibacterial activity of test compounds **Zn1-3** was shown in Table 2.4. The antibacterial activity of test compounds was similar against all tested bacteria with MIC value in the range of 50-200 $\mu\text{g}/\text{mL}$. In the case of MRSA **Zn2** and **Zn3** were two-fold active than **Zn1**. Free ligands were inactive against all tested bacteria.

The antibacterial active study showed the effect of coordination of metal with free ligands **L1** and **L2** against tested bacterial. The coordination of metal with free ligands leads to the formation of n metal to ligand charge transfer complex(Mallikarjuna et al. 2018). **Zn1-3** was very active compared to reported metal complexes against bacteria(Ejidike 2018; Poyraz et al. 2008). **Zn1-3** were good antibacterial agent than chelated Zn(II)-benzimidazole complex against MRSA (Gwaram et al. 2012). **Zn1-3** was 2.5 to 5-fold active against MRSA than macrocyclic Zn(II) Schiff base complex (Mcginley et al. 2013). Some zinc complexes were inactive against MRSA (Khajooe Nejad et al. 2018; Tarte et al. 2008).

The metal to ligand charge transfer complexes has a high net positive charge, which helped for their interaction with negatively charged bacterial membrane. The presence of the benzene ring imparts lipophilicity in the complex than free ligands, facilitating the efficient penetration of the complex into the cell wall of microorganisms (Khosravi and Mansouri-torshizi 2018). Once entered in the cell, complexes bind to DNA with high affinity to block its function, lead to the death of bacteria (Khosravi and Mansouri-torshizi 2018; Papadopoulos et al. 2017).

Table 2.4 MIC values of complexes **Zn1–3** and ligands **L1** and **L2** in $\mu\text{g/mL}$.

	Bacteria	Zn1	Zn2	Zn3	L1	L2	Streptomycin
Gram positive	<i>MRSA</i>	100	50	50	> 200	> 200	> 200
	<i>S. aureus</i>	100	100	200	> 200	> 200	1.526
	<i>B. subtilis</i>	200	100	100	> 200	> 200	3.052
	<i>E. faecalis</i>	200	100	200	> 200	> 200	3.052
Gram negative	<i>E. coli</i>	100	100	100	> 200	>200	1.526
	<i>S. typhimurium</i>	100	100	200	> 200	> 200	6.104
	<i>K. pneumoniae</i>	100	200	200	> 200	> 200	3.052

2.4.4 Gel-electrophoresis assay

During the multiplication of bacteria, DNA replication is critically important to step failure of which resulted in bacteria death. Most of the antibacterial drugs worked on the same principle by targeting DNA (Papadopoulos et al. 2017). Most of the metal complexes in cells efficiently switch their coordination from ligand to DNA, leading to the death of bacteria (Li et al. 2017). To investigate the same phenomena in the case of **Zn1-3** DNA gel-electrophoresis assay was performed with plasmid DNA (EcDNA) and calf thymus DNA (CT-DNA).

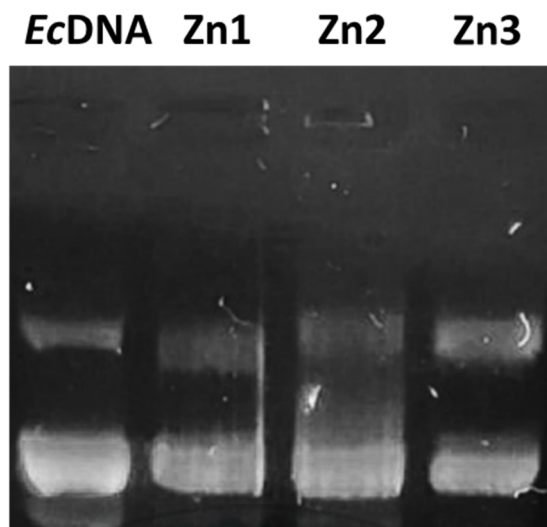


Figure 2.4. Agarose gel electrophoresis pattern of pDNA in the presence of complexes **Zn1–3**. Lane 1, DNA control; lane 2, DNA + **Zn1** (1 mM); lane 3, DNA + **Zn2** (1 mM); lane 4, DNA + **Zn3** (1 mM).

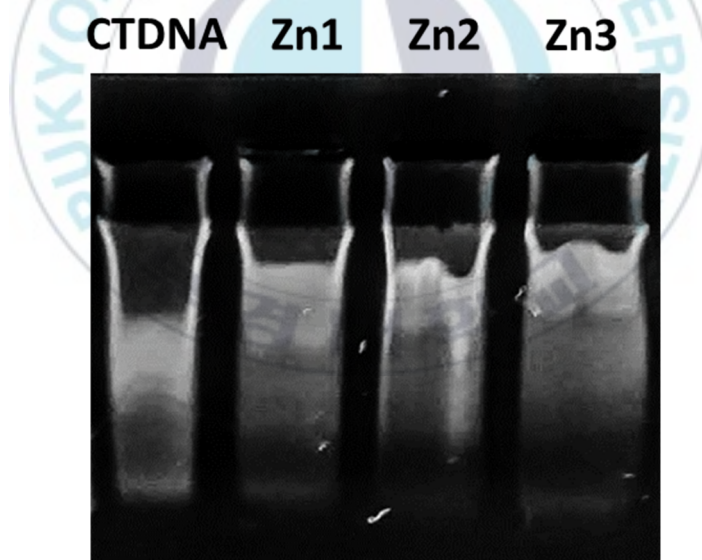


Figure 2.5. Agarose gel electrophoresis pattern of CTDNA in the presence of the synthesized zinc complexes **Zn1-3**. Lane 1, CTDNA control; lane 2, DNA + **Zn1** (1 mM); lane 3, DNA + **Zn2** (1 mM); lane 4, DNA + **Zn3** (1 mM).

The gel-electrophoresis assay of the mixed solution of **Zn1-3** with EcDNA and

CT-DNA showed relatively fast migration of the untreated DNA. The interaction between **Zn1-3** and DNA slowdown the DNA mobility (Huq et al. 2004). Breakdown of a single strand of EcDNA formed the DNA smear upon gel electrophoresis (Li et al. 2018).

In Fig. 2.4 and 2.5, Lane 1 was the free DNA and Lane 2-4 DNA incubated with complexes **Zn1-3**. EcDNA was composed of supercoiled (Lane I) and circular (Lane II) forms. **Zn1** and **Zn2** broke the EcDNA to form DNA smear. **Zn3** had a high binding affinity for EcDNA, forming a thick band in Lane I. **Zn1-3** had a high binding affinity for CT-DNA. The CT-DNA binding affinity of **Zn3** was higher than **Zn2** and **Zn1**. These results indicated that bacterial DNA cleavage was a plausible antibacterial mechanism **Zn1** and **Zn2**, whereas **Zn3** may have some other mechanism.

2.4.5 Antioxidant assay

The aim of this experiment was to determine the anti-inflammatory activity of **Zn1-3** in comparison to rutin (Udilova, Kozlov, and Bieberschulte 2003). DPPH formed a stable free radical having strong purple color in methanol (Figure 2.6). It plays the role of acceptor in the presence of hydrogen radical and electron donor moiety resulting in a yellow-colored product. The results showed the higher antioxidant activity of **Zn2** than **Zn1**, **Zn3**, and rutin. The reducing antioxidant activity of **Zn1-3** and rutin was as follows: **Zn2** > R > **Zn3** > **Zn1**.

The antioxidant mechanism of **Zn1-3** may be the acceptance of active hydrogen of amine and/or methyl group (Al-amiery 2016). The electron withdrawing nature of aromatic ring weaken the benzylic and imine hydrogen, which could be easily reacted with H-accepter (Wu et al. 2012).

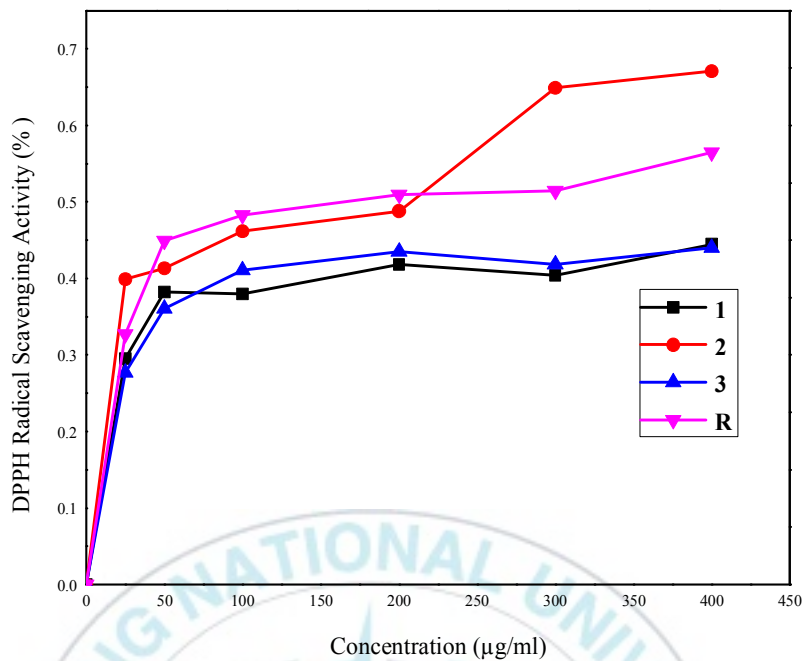
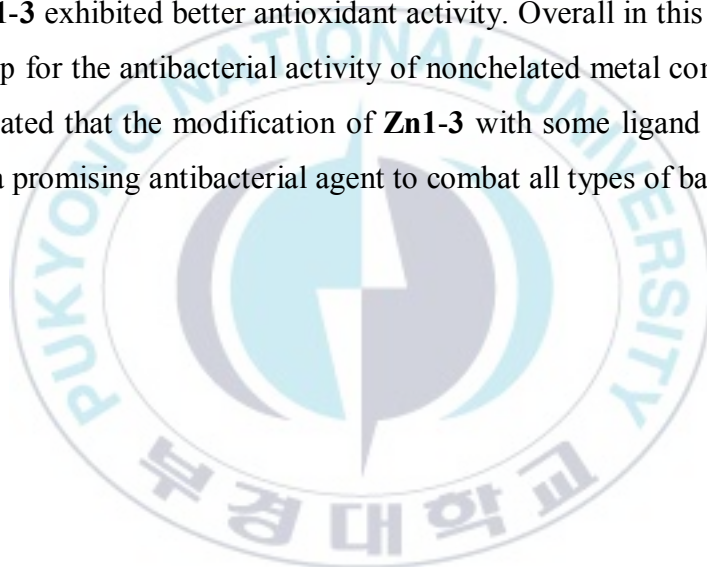


Figure 2.6: Antioxidant activity of complexes **Zn1-3**.

2.5 Conclusion

In this study, we attempted to synthesize and characterize novel nonchelated **Zn1-3**. UV-Vis spectroscopy, ¹H-NMR spectroscopy, single X-ray crystallography, and elemental analysis confirmed the nonchelated nature of **Zn1-3** with pseudo-tetrahedral geometry. **Zn1-3** showed similar antibacterial activity in contrast to all tested bacterial strains. In particular, **Zn2** and **Zn3** were two-fold active against MRSA with MIC value of 50 µg/mL than **Zn1**. DNA gel-electrophoresis results showed that **Zn1** and **Zn3** degraded EcDNA, while **Zn3** had a high affinity for EcDNA. **Zn1-3** showed a high binding affinity to CT-DNA. Further, **Zn1-3** exhibited better antioxidant activity. Overall in this work, we tried to fill the gap for the antibacterial activity of nonchelated metal complexes. These results indicated that the modification of **Zn1-3** with some ligand or substituents can lead to a promising antibacterial agent to combat all types of bacteria.



2.6 References

- A, A. S. Stella Shalini, M. Amaladasan, N. Prasannabalaji, J. Revathi, and G. Muralitharan. 2014. "Synthesis , Characterization and Antimicrobial Studies on 13-Membered-N 6 -Macrocyclic Transition Metal Complexes Containing Trimethoprim." *ARABIAN JOURNAL OF CHEMISTRY*.
- Al-amier, Ahmed. 2016. "Green Antioxidants: Synthesis and Scavenging Activity of Coumarin- Thiadiazoles as Potential Antioxidants Complemented by Molecular Modeling Phcog . Net An Official Publication of Phcog . Net & SciBiolMed . Org." (March).
- Almoudi, Manal Mohamed, Alaa Sabah Hussein, Mohamed Ibrahim Abu Hassan, and Nurhayati Mohamad Zain. 2018. "A Systematic Review on Antibacterial Activity of Zinc against Streptococcus Mutans." *Saudi Dental Journal* 30(4):283–91.
- Ashraf, Adnan, Waseeq Ahmad Siddiqui, Jamshed Akbar, Ghulam Mustafa, Harald Krautscheid, Nazif Ullah, Bushra Mirza, Falak Sher, Muhammad Hanif, and Christian G. Hartinger. 2016. "Metal Complexes of Benzimidazole Derived Sulfonamide: Synthesis, Molecular Structures and Antimicrobial Activity." *Inorganica Chimica Acta* 443(2016):179–85.
- Bello-Vieda, Nestor J., Homero F. Pastrana, Manuel F. Garavito, Alba G. Ávila, Adriana M. Celis, Alvaro Muñoz-Castro, Silvia Restrepo, and John J. Hurtado. 2018. "Antibacterial Activities of Azole Complexes Combined with Silver Nanoparticles." *Molecules* 23(2):1–17.
- Bharty, M. K., R. K. Dani, P. Nath, A. Bharti, N. K. Singh, Om Prakash, Ranjan K. Singh, and R. J. Butcher. 2015. "Syntheses, Structural and Thermal Studies on Zn(II) Complexes of 5-Aryl-1,3,4-Oxadiazole-2-Thione and Dithiocarbamates: Antibacterial Activity and DFT Calculations." *Polyhedron*

98:84–95.

Butler, Jonathan A., Xin Li, Robert K. Poole, and John Grant Collins. 2018. “The Antimicrobial Activity of Mononuclear Ruthenium(II) Complexes Containing the Dppz Ligand.” *ChemPlusChem* 83(7):643–50.

Devi, J., M. Yadav, D. Kumar, L. S. Naik, and D. K. Jindal. 2019. “Some Divalent Metal(II) Complexes of Salicylaldehyde-Derived Schiff Bases: Synthesis, Spectroscopic Characterization, Antimicrobial and in Vitro Anticancer Studies.” *Applied Organometallic Chemistry* 33(2):1–22.

Ejidike, Ikechukwu P. 2018. “Cu(II) Complexes of 4-[(1E)-N-{2-[(Z)-Benzylidene-Amino]Ethyl} Ethanimidoyl]Benzene-1,3-Diol Schiff Base: Synthesis, Spectroscopic, In-Vitro Antioxidant, Antifungal and Antibacterial Studies.” (Ii):1–18.

Fodor, Csaba, Tímea Stumphauser, Ralf Thomann, Yi Thomann, and Béla Iván. 2016. “Poly(N -Vinylimidazole)- 1 -Poly(Propylene Glycol) Amphiphilic Conetworks and Gels: Molecularly Forced Blends of Incompatible Polymers with Single Glass Transition Temperatures of Unusual Dependence on the Composition.” *Polymer Chemistry* 7(34):5375–85.

Ghosh, Amrita, Abir U. Igamberdiev, and Samir C. Debnath. 2018. “Thidiazuron-Induced Somatic Embryogenesis and Changes of Antioxidant Properties in Tissue Cultures of Half-High Blueberry Plants.” *Scientific Reports* (June):1–11.

Gwaram, Nura Suleiman, Hapipah Mohd Ali, Siti Munirah Saharin, Mahmood Ameen Abdulla, Thong Kwai Lin, Chai Lay Ching, and Cher Lin Ooi. 2012. “Synthesis , Characterization , and Biological Applications of Some 2-Acetylpyridine and Acetophenone Derivatives.” 2(12):27–38.

Huq, Fazlul, Jun Qing Yu, Hassan Dagheriri, and Philip Beale. 2004. “Studies on

Activities, Cell Uptake and DNA Binding of Four Trans-Planaramineplatinum(II) Complexes of the Form: $\text{Trans-PtL}(\text{NH}_3)_2\text{Cl}_2$, Where $\text{L} = 2\text{-Hydroxypyridine, Imidazole, 3-Hydroxypyridine and Imidazo}(1,2\text{-}\alpha)\text{Pyridine}$.” *Journal of Inorganic Biochemistry* 98(8):1261–70.

Indoria, Shikha, Tarlok S. Lobana, Henna Sood, Daljit S. Arora, Geeta Hundal, and Jerry P. Jasinski. 2016. “Synthesis, Spectroscopy, Structures and Antimicrobial Activity of Mixed-Ligand Zinc(II) Complexes of 5-Nitro-Salicylaldehyde Thiosemicarbazones.” *New Journal of Chemistry* 40(4):3642–53.

Kavanagh, Kevin, Helge Müller-Bunz, Cillian O’Beirne, Matthias Tacke, Oyinlola Dada, Yannick Ortin, Hessah T. Althani, Jennifer Cassidy, and Xiangming Zhu. 2018. “Novel Derivatives of the Antibiotic NHC–Ag(I) Drug Candidate SBC3: Synthesis, Biological Evaluation and ^{109}Ag NMR Studies.” *Polyhedron* 149:95–103.

Khajooee Nejad, Fateme, Mehrji Khosravan, S. Yousef Ebrahimipour, and Franco Bisceglie. 2018. “A Mixed-Ligand Quinazoline-Based Ni(II) Schiff Base Complex: Synthesis, Characterization, Crystal Structure, Antimicrobial Investigation and Catalytic Activity for the Synthesis of 2H-Indazolo[2,1-b]Phthalazine-Triones.” *Applied Organometallic Chemistry* 32(1):1–9.

Khosravi, Fatemeh, and Hassan Mansouri-torshizi. 2018. “Antibacterial Combination Therapy Using Co, Cu, Zn and Pd Complexes: Their Calf Thymus DNA Binding Studies.” *Journal of Biomolecular Structure and Dynamics* 1102:1–20.

Kim, Hong Seok, Jyoti R. Jadhav, Sung Ji Jung, and Jin Hwan Kwak. 2013. “Synthesis and Antimicrobial Activity of Imidazole and Pyridine Appended Cholestane-Based Conjugates.” *Bioorganic and Medicinal Chemistry Letters* 23(15):4315–18.

- Leonardi, Darío, Vera A. Alvarez, Natalia L. Calvo, Ariel D. Quiroga, Laura A. Svetaz, and María C. Lamas. 2018. "Chitosan-Hydroxypropyl Methylcellulose Tioconazole Films: A Promising Alternative Dosage Form for the Treatment of Vaginal Candidiasis." *International Journal of Pharmaceutics* 556(September 2018):181–91.
- Li, Rachel E., Y. Robert Li, Hong Zhu, and Zhenquan Jia. 2018. "Graphene Quantum Dots Potently Block Copper-Mediated Oxidative DNA Damage: Implications for Cancer Intervention." *React Oxyg Species (Apex)* 6(18):406–13.
- Li, Shuo, Jia-xuan Chen, Qing-xiang Xiang, Li-qun Zhang, and Cheng-he Zhou. 2014. "The Synthesis and Activities of Novel Mononuclear or Dinuclear Cyclen Complexes Bearing Azole Pendants as Antibacterial and Antifungal Agents." *European Journal of Medicinal Chemistry* 84:677–86.
- Li, Si Tong, Zhong Ying Ma, Xin Liu, Jin Lei Tian, and Shi Ping Yan. 2017. "Synthesis, Crystal Structures, DNA/Bovine Serum Albumin Binding, DNA Cleavage and Cytotoxicity of Five Mononuclear Zinc(II) Complexes." *Applied Organometallic Chemistry* 31(11):1–14.
- Mallikarjuna, N. M., J. Keshavayya, M. R. Maliyappa, R. A. Shoukat Ali, and Talavara Venkatesh. 2018. "Synthesis, Characterization, Thermal and Biological Evaluation of Cu (II), Co (II) and Ni (II) Complexes of Azo Dye Ligand Containing Sulfamethaxazole Moiety." *Journal of Molecular Structure* 1165:28–36.
- Mcginley, John, Malachy Mccann, Kaijie Ni, Theresa Tallon, Kevin Kavanagh, Michael Devereux, Xiaomei Ma, and Vickie Mckee. 2013. "Imidazole Schiff Base Ligands : Synthesis , Coordination Complexes and Biological Activities." *Polyhedron* 55:169–78.

- Moghnieh, Rima, Adel F. Alothman, Abdulhakeem O. Althaqafi, Madonna J. Matar, Thamer H. Alenazi, Fayassal Farahat, Shelby L. Corman, Caitlyn T. Solem, Nirvana Raghbir, Cynthia Macahilig, and Jennifer M. Stephens. 2017. "Epidemiology and Outcome of Invasive Fungal Infections and Methicillin-Resistant Staphylococcus Aureus (MRSA) Pneumonia and Complicated Skin and Soft Tissue Infections (CSSTI) in Lebanon and Saudi Arabia." *Journal of Infection and Public Health* 10(6):849–54.
- Nandanwar, Sondavid K., and Hak Jun Kim. 2019. "Anticancer and Antibacterial Activity of Transition Metal Complexes." *ChemistrySelect* 4(5):1706–21.
- Papadopoulos, Athanasios N., Ioanna Zoi, Catherine P. Raptopoulou, Dimitris P. Kessissoglou, Alketa Tarushi, Vassilis Psycharis, Chrisoula Kakoulidou, and George Psomas. 2017. "Zinc Complexes of Diflunisal: Synthesis, Characterization, Structure, Antioxidant Activity, and in Vitro and in Silico Study of the Interaction with DNA and Albumins." *Journal of Inorganic Biochemistry* 170:85–97.
- Poyraz, Mehmet, Musa Sarı, Ertan Şahin, Ayse Güney, Fatih Demirci, and Seref Demirayak. 2008. "Synthesis, Characterization and Antimicrobial Activity of a Zn(II) Complex with 1-(1H-Benzoimidazol-2-Yl)-Ethanone Thiosemicarbazone." *Journal of Coordination Chemistry* 61(20):3276–83.
- Singh, Kiran, Yogender Kumar, Parvesh Puri, and Chetan Sharma. 2017. "Antimicrobial , Spectral and Thermal Studies of Divalent Cobalt , Nickel , Copper and Zinc Complexes with Triazole Schiff Bases." *Arabian Journal of Chemistry* 10:S978–87.
- Singha, Priyadarshini, Christina D. Workman, Jitendra Pant, Sean P. Hopkins, and Hitesh Handa. 2019. "Zinc-Oxide Nanoparticles Act Catalytically and Synergistically with Nitric Oxide Donors to Enhance Antimicrobial Efficacy." *Journal of Biomedical Materials Research - Part A* 1425–1433.

- Tarte, Naresh H., Seong Ihl Woo, Liqiang Cui, Young Dae Gong, and Young Ho Hwang. 2008. "Novel Non-Chelated Cobalt(II) Benzimidazole Complex Catalysts: Synthesis, Crystal Structures and Cocatalyst Effect in Vinyl Polymerization of Norbornene." *Journal of Organometallic Chemistry* 693(4):729–36.
- Taylor, Kathryn M., Francesca Solfa, Arwyn T. Jones, Helen L. Wiggins, Andrew D. Westwell, Stephen E. Hiscox, and Jennifer M. Wymant. 2015. "Disulfiram-Induced Cytotoxicity and Endo-Lysosomal Sequestration of Zinc in Breast Cancer Cells." *Biochemical Pharmacology* 93(3):332–42.
- Thabit, Abrar K., Dania F. Fatani, Maryam S. Bamakhrama, Ola A. Barnawi, Lana O. Basudan, and Shahad F. Alhejaili. 2019. "Antibiotic Penetration into Bone and Joints: An Updated Review." *International Journal of Infectious Diseases : IJID : Official Publication of the International Society for Infectious Diseases* 81:128–36.
- Udilova, Natalia, Andrey V Kozlov, and Werner Bieberschulte. 2003. "The Antioxidant Activity of Caroverine." 65:59–65.
- Vančo, Ján, Zdeněk Šindelář, Zdeněk Dvořák, and Zdeněk Trávníček. 2015. "Iron-Salophen Complexes Involving Azole-Derived Ligands: A New Group of Compounds with High-Level and Broad-Spectrum in Vitro Antitumor Activity." *Journal of Inorganic Biochemistry* 142:92–100.
- Vijayakumar, Vijayaparthasarathi, Jegathalaprathaban Rajesh, Irudayaraj Bernadette Amali, Gurusamy Rajagopal, N. Indra Gandhi, and Mookkandi Palsamy Kesavan. 2019. "Structural Analysis, Antimicrobial and Cytotoxic Studies on New Metal(II) Complexes Containing N2O2 Donor Schiff Base Ligand." *Journal of Molecular Structure* 1183(Ii):342–50.
- Wu, Huilu, Jingkun Yuan, Ying Bai, Hua Wang, Guolong Pan, and Jin Kong. 2012.

“Journal of Photochemistry and Photobiology B: Biology A Seven-Coordinated Manganese (II) Complex with V-Shaped Ligand Bis (N - Benzylbenzimidazol-2-Ylmethyl) Benzylamine: Synthesis , Structure , DNA-Binding Properties and Antioxidant Activities.” *Journal of Photochemistry & Photobiology, B: Biology* 116:13–21.

Wu, Xiaohu, Gao-Xue Wang, Yufeng Shen, Yang Hu, and Xiao Tu. 2017. “Synthesis and Biological Evaluation of Coumarin Derivatives Containing Imidazole Skeleton as Potential Antibacterial Agents.” *European Journal of Medicinal Chemistry* 143:958–69.

Yakoob, Javed, Zaigham Abbas, Muhammad Waqas Usman, Safia Awan, Shagufta Naz, Fatima Jafri, Saeed Hamid, and Wasim Jafri. 2014. “Comparison of Antimicrobial Activity of Zinc Chloride and Bismuth Subsalicylate against Clinical Isolates of Helicobacter Pylori.” *Microbial Drug Resistance* 20(4):305–9.

Zheng, Zhiqiang, Qiming Xu, Jiangna Guo, Jing Qin, Hailei Mao, Bin Wang, and Feng Yan. 2016. “Structure-Antibacterial Activity Relationships of Imidazolium-Type Ionic Liquid Monomers, Poly(Ionic Liquids) and Poly(Ionic Liquid) Membranes: Effect of Alkyl Chain Length and Cations.” *ACS Applied Materials and Interfaces* 8(20):12684–92.

Chapter 3

Cobalt(II) Benzazole Derivative Complexes: Synthesis, Characterization, Antibacterial Activity, Synergistic Activity with Antibiotics and Its Mechanism of Action

3.1 Abstract

Here, the single-step synthesis of non-chelated Co(II)-complexes (**Co1-Co3**) [ZnCl₂L₂] of non-chelating ligands with L= 2-methylbenzimidazole (**L1**), 2-methylbenzoxazole (**L2**), and 2-methylbenzothiazole (**L3**) had been proposed at room temperature. The characterization of **Co1-Co3** using UV-Vis spectroscopy, ¹H-NMR spectroscopy, single X-ray crystallography, and elemental analysis confirmed their non-chelated nature. Antibacterial assay disclosed the higher bacteria inhibition efficiency of **Co1-Co3** against tested bacteria with minimum inhibitory concentration (MIC) of 12.5-200 µg/ml than non-chelating ligand. **Co2** and **Co3** efficiently inhibited the growth of *S. aureus* at a concentration of 12.5 µg/mL. The tremendous change in antibacterial efficiency of **Co1-Co3** in the presence of ampicillin (**AMP**) is called a synergistic effect. **Co2** and **Co3** efficiently inhibited the growth of MRSA in presence of ampicillin, whereas ampicillin alone had no effect on the growth of MRSA. Investigation of the antibacterial mechanism of **Co1-Co3** and **Co1-Co3+AMP** revealed that only **Co2+AMP** and **Co3+AMP** crossed the cell wall MRSA, indicating the bacteria cell wall disruption ability of **Co2+AMP** and **Co3+AMP**. This study disclosed that **Co1-Co3** could combat the growth of bacteria, which could be beneficial for advanced biological studies in the future.

Keywords: Antibacterial activity • Bioinorganic Chemistry • Synergy with Antibiotics • Membrane disruption • Medicinal Bioinorganic Chemistry

3.2 Introduction

Organometallic complexes are imperative for various industrial applications such as pharma industries and efficiently inhibited the growth of a collection of bacteria counting *S. aureus* (Schatzschneider 2019). Recently, the investigation of the bactericidal property of synthetic OC is rising among researchers (Abdel-Wahab, Awad, and Badria 2011; Patel, Dosi, and Bhatt 2012; Vlaicu et al. 2019). OC is a vital drug candidate with great diversity in bactericidal action. OC synthesis is not a straightforward process; noteworthy efforts are needed for the synthesis of an efficient bactericidal entity. The main objective of researchers is to fabricate an efficient bactericidal entity for controlling pathogenic bacteria (Nandanwar and Kim 2019).

Cobalt is a vital trace metal present in humans (Moll and Davis 2017). It occupies a central position in naturally occurring cobalamin, a regulator of DNA and proteins in nerve cells (Moll and Davis 2017). Cobalt is also found in protein like methionine aminopeptidase 2 (Węglarz-Tomczak et al. 2016). Cobalt can switch the medicinal activity of metal-coordinating drugs (Malik et al. 2018). Cobalt can efficiently deliver cancer-preventing nitrogen mustard drugs in hypoxic regions of solid tumors, which impart high importance to cobalt for the development of the potential drugs (Munteanu and Suntharalingam 2015). A large number of synthetic cobalt complexes were tested as a remedy for microbes (El-Sawaf et al. 2018), virus (Abu-Dief and Mohamed 2015), fungus (Abu-Dief and Mohamed 2015), inflammatory (Abu-Dief and Mohamed 2015), mycobacteria (Datta et al. 2015), parasite (Hubin et al. 2014), thrombolite (Akhtar et al. 2016), and tumor (Khan et al. 2019) due to their occurrence in the biological system and enhanced activity in the presence of other medications (Bello-Vieda et al. 2018). A literature survey revealed that very few nonchelated cobalt complexes were synthesized for the investigation of their antibacterial activity, which offered a great opportunity for the development of biologically active nonchelated cobalt complexes.

For the synthesis of organic drugs, the first choice of the researcher is a benzimidazole ring containing compounds(Lai et al. 2019; Luo et al. 2016; Yadav and Ganguly 2015). Due to the presence of benzimidazole nucleus in countless natural components such as vitamin B12, DNA, RNA, metalloenzymes, hemoglobin, and corrin ring, it has gained higher importance for the fabrication of drugs such as enviroxime. Several novel benzimidazole drugs are available in the market such as anthelmintic albendazole, fenbendazole, oxfenbendazole, thiabendazole, mebendazole, etc. Still, it is the best choice for the discovery of novel drugs(Yadav and Ganguly 2015). The reactive nitrogen of the benzimidazole ring can coordinate easily with metals, resulting in the formation of its metal complexes. These metal complexes are well known documented for their medicinal properties to cure bacterial infection (Mahmood et al. 2019) and cancer (NAMI-A)(El-Wakiel, El-Keiy, and Gaber 2015). The coordination of the benzimidazole ring with metal transfers the charge from metal to ligand, which increases the cell wall binding affinity of benzimidazole. Later, benzimidazole can easily penetrate the cell membrane. Such metal complexes have high antimicrobial activity than the ligands alone(Kumar et al. 2016).

Water pollution intensifies the growth of harmful bacteria, which is a developing risk to human health(Behravesh et al. 2011). The poor management of unwanted medicine among peoples and for agricultural works increases the concentration of drugs in water bodies. Bacteria exposed to such conditions developed multidrug resistance. The control over such bacteria is a major challenge for researchers. The common antibiotic resistance bacteria is MRSA, which causes several untreatable skin infections such as pneumonia(Brahma et al. 2019). The unwanted growth of difficult-to-treat pathogens is a serious issue for the future. Researchers are modifying the existed antibiotics to enhance their antibacterial efficiency. The treatment of resistant pathogens with the combination of multiple drugs is a conceivable methodology to address this issues(Cherian et al. 2017; Kaka et al. 2006). Another possible strategy is the use of metal like Co(II) with existing

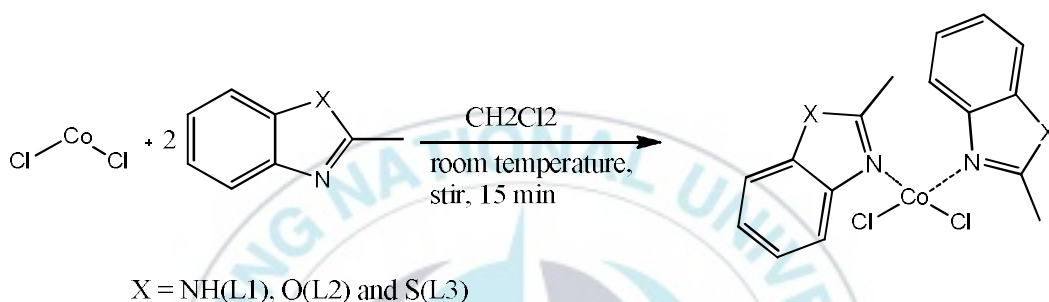
antibiotics to cope with these issues (STRAIT, DUFRENOY, and PRATT 1948; Zhang et al. 2013). It was found that the bactericidal activity of penicillin enhanced against *S. aureus*, *B. subtilis*, *E. coli*, and *Proteus vulgaris* after coordinating to Co(II) ion (STRAIT et al. 1948). Co(II)-penicillin combination inhibited the growth of *S. aureus* 4- to 8-fold faster than penicillin alone. The combination of benzimidazole derivative with Chloromycin (2 mg/mL) or Norfloxacin (0.25 mg/mL) intensify the growth of MRSA (Zhang et al. 2013). The use of the combination of Co(II) complexes with antibiotics may be the plausible way to cope up with the discussed challenges. The resulting mixture may give positive, negative, or no results.

There are four bactericidal mechanisms of antibiotics such as interruption of the synthesis of the cell membrane, destruction of the cell membrane, blocking of nucleic acid multiplication, and blocking of protein synthesis (Nandanwar and Kim 2019). The investigation of the antibacterial mechanism of a few synthetic Co(II) complexes reveals that they cross the membrane of bacteria and coordinate with the nucleophilic site of enzyme (Chang, Simmers, and Knight 2010). The study shows that the bactericidal metal complexes with highly aromatic rings can pass the lipid membrane of bacteria (Abu-Dief and Mohamed 2015). These results indicate that the aromatic ring is crucial for increasing the membrane permeability of bactericidal metal complexes. Therefore, it is significant to investigate the membrane permeability of metal complexes.

In this study, attempts have been made to synthesize and characterize Co(II)-azole derivative complexes (**Co1-3**) using UV-vis, FT-IR spectroscopy, and X-ray crystallography. Later, their bactericidal activity, synergistic activity, and bactericidal mechanism were evaluated.

3.3 Results and Discussion

3.3.1 Synthesis: The Co(II)-azole complexes **Co1-3** with a general formula of $[\text{CoCl}_2\text{L}_2]$ (L= 2-methylbenzimidazole (**L1**), 2-methylbenzoxazole (**L2**), and 2-methylbenzthiazole (**L3**)) were synthesized using facile synthetic procedure (Scheme 3.1). **Co1-3** was successfully characterized by UV-vis spectroscopy, FT-IR spectroscopy, and X-ray crystallography.



Scheme 3.1. Synthesis of complexes **Co1-3** from benzazole ligands **L1-L3**.

3.3.2 Crystal structures: The X-ray crystal structure of **Co1** (Figure 3.1-3.3, Table 3.1-3.3) was elucidated in the previously published paper (Sánchez-Guadarrama et al. 2009; Tarte et al. 2008). The X-ray crystal structures of **Co2** and **Co3** are revealed in Figure 2 and Figure 3, respectively. The crystallographic data and refinement parameters of **Co2** and **Co3** are summarized in Table 1. The coordination geometry of the **Co2** and **Co3** are distorted tetrahedral geometry, similar to the analogous Ni(II)-complexes reported in a published paper (Tarte, Cho, and Woo 2007). Table 2 lists the relevant bond distances and angles of **Co2** and **Co3**. The crystal structure of both the **Co2** and **Co3** is triclinic. **Co2** and **Co3** are monomeric, and the ligands 2-methylbenzoxazole and 2-methylbenzothiazole behave as monodentate ligands and coordinated to cobalt *via* the amide nitrogen. In the structure of the **Co2** and **Co3**, the Co(II) ion occupy the center of symmetry and being coordinated to four ligands related by the inversion center. Thus, the

Co(II) ion in the **Co2** and **Co3** is tetracoordinate, and as a result of the inversion center, it displays a distorted tetrahedral geometry.

Table 3.1. Crystallographic data and structure refinement for complexes **Co1–3**

Complexes	Co1	Co2	Co3
Empirical formula	C ₁₆ H ₁₆ Cl ₂ Co N ₄	C ₁₆ H ₁₄ Cl ₂ Co N ₂ O ₂	C ₁₆ H _{13.5} Cl ₂ Co N ₂ S ₂
Formula weight	394.16	396.12	427.74
Temperature	296 K	296 K	296 K
Wavelength	0.71073 Å	0.71073 Å	0.71073 Å
Crystal system	Monoclinic	Triclinic	Triclinic
Space group	<i>P2(1)/n</i>	<i>P1</i>	<i>P1</i>
Unit cell dimension	a = 12.7017 Å, α = 90 ° b = 9.8602 Å, β = 111.868 ° c = 14.7287 Å, γ = 90 °	a = 8.0377 Å, α = 86.364 ° b = 8.8055 Å, β = 78.823 ° c = 12.198 Å, γ = 76.812 °	a = 8.4268 Å, α = 72.744 ° b = 9.0981 Å, β = 78.657 ° c = 12.8867 Å, γ = 69.751 °
Volume	1711.91 Å ³	824.447 Å ³	880.33 Å ³
Z	4	2	2
Density (calculated)	1.529 mg/m ³	1.596 mg/m ³	1.614 mg/m ³
Absorption coefficient	1.317 mm ⁻¹	1.374 mm ⁻¹	1.513 mm ⁻¹
F(000)	804	402.0	433
Crystal size	0.26 × 0.23 × 0.04 mm ³		0.2 × 0.2 × 0.15 mm ³
Theta range for data collection	1.81 to 28.39 °	0.973 to 32.58 °	1.66 to 28.87 °
Index ranges	-16 ≤ h ≤ 16 -13 ≤ k ≤ 13 -19 ≤ l ≤ 19	-12 ≤ h ≤ 12 -13 ≤ k ≤ 13 -18 ≤ l ≤ 18	-11 ≤ h ≤ 11 -12 ≤ k ≤ 12 -17 ≤ l ≤ 17
Reflections collected	17581	6002	27599
Independent reflections	4270 [R(int) = 0.0255]		8764 [R(int) = 0.0379]
Completeness to theta = 28.87 °	99.3 %		98.1 %
Absorption correction	None		Semi-empirical from equivalents
Max. and min. transmission	0.9492 and 0.7257	0.930 and 0.941	0.940 and 0.931
Refinement method	Full-matrix least-squares on F ²		Full-matrix least-squares on F ²
Data / restraints / parameters	4270 / 0 / 208	//210	8764 / 3 / 418
Goodness-of-fit on F ²	1.028	1.013	1.074
Final R indices [I > 2σ(I)]	R1 = 0.0308, wR2 = 0.0826	R1 = 0.0390, wR2 = 0.1017	R1 = 0.0362, wR2 = 0.0696
R indices (all data)	R1 = 0.0455, wR2 = 0.0905		R1 = 0.0753, wR2 = 0.0828
Largest diff. peak and hole	0.327 and -0.288 e.Å ⁻³		0.510 and -0.382 e.Å ⁻³

Table 3.2. Comparison of selected bond lengths (Å) and angles (°) of **Co1-3**.

Co1	Co2	Co3
Co-N(1) - 2.035(15)	Co-N(1) - 2.064(1)	Co-N(1) - 2.10(1)
Co-N(11) - 2.036(16)	Co-N(2) - 2.061(1)	Co-N(2) - 2.067(8)
Co-Cl(1) - 2.264(6)	Co-Cl(1) - 2.2439(7)	Co-Cl(1) - 2.251(3)
Co-Cl(2) - 2.244(6)	Co-Cl(2) - 2.2241(8)	Co-Cl(2) - 2.240(2)
N(1)-Co-N(11) - 104.15(6)	N(1)-Co-N(2) - 109.00(5)	N(1)-Co-N(2) - 101.7(3)
N(1)-Co-Cl(1) - 105.15 (5)	N(1)-Co-Cl(1) - 103.08(4)	N(1)-Co-Cl(1) - 115.3(2))
N(1)-Co-Cl(2) - 117.15(5)	N(1)-Co-Cl(2) - 111.39(4)	N(1)-Co-Cl(2) - 110.6(2)
N(11)-Co-Cl(2) - 105.77(5)	N(2)-Co-Cl(1) - 111.13(4)	N(2)-Co-Cl(1) - 104.9(2)

N(1)-Co-Cl(1) - 114.73(5)	N(2)-Co-Cl(2) - 104.66(4)	N(2)-Co-Cl(2) - 115.7(2)
Cl(1)-Co-Cl(2) - 110.14(3)	Cl(1)-Co-Cl(2) - 117.52(2)	Cl(1)-Co-Cl(2) - 108.6(1)

Table 3.3. Hydrogen bonding of **Co1** [\AA and $^\circ$].

Complex	D-H...A	d(D-H)	d(H...A)	d(D...A)	\angle (DHA)
1^a	N-H...1	0.86	2.37	3.195(16)	162.2

Symmetry transformations used to generate equivalent atoms:

$$a = \#1 \ x-1/2, -y+1/2, z-1/2$$

Furthermore, the Co-N bond lengths in **Co2** and **Co3** are less than the Co-Cl bond lengths, confirming the distortion from a regular tetrahedron. The N-Co-N bond angle in the **Co2** and **Co3** are $109.00(5)^\circ$ and $101.7(3)^\circ$, respectively. The Cl-Co-Cl bond angle of complexes **2** and **3** are $117.52(2)^\circ$, and $108.6(1)^\circ$, respectively. The density of the **Co2** and **Co3** are 1.596 mg/m^3 and 1.614 mg/m^3 , respectively. The space group of the **Co2** and **Co3** is P-1. These results indicate that the **Co2** and **Co3** may have a similar nucleation mechanism.

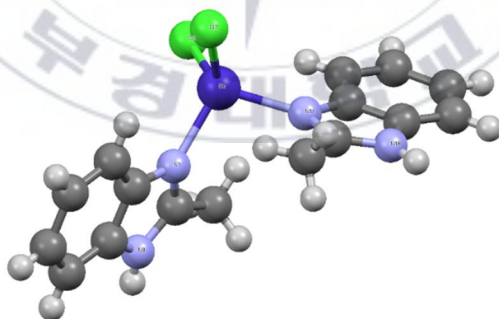


Figure 3.1. X-ray structure of dichloro-bis(2-methylbenzimidazole)cobalt(II) **Co1**.

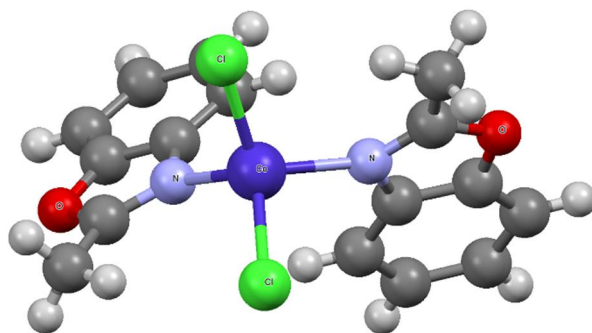


Figure 3.2. X-ray structure of dichloro-bis(2-methylbenzoxazole)cobalt(II) Co2.

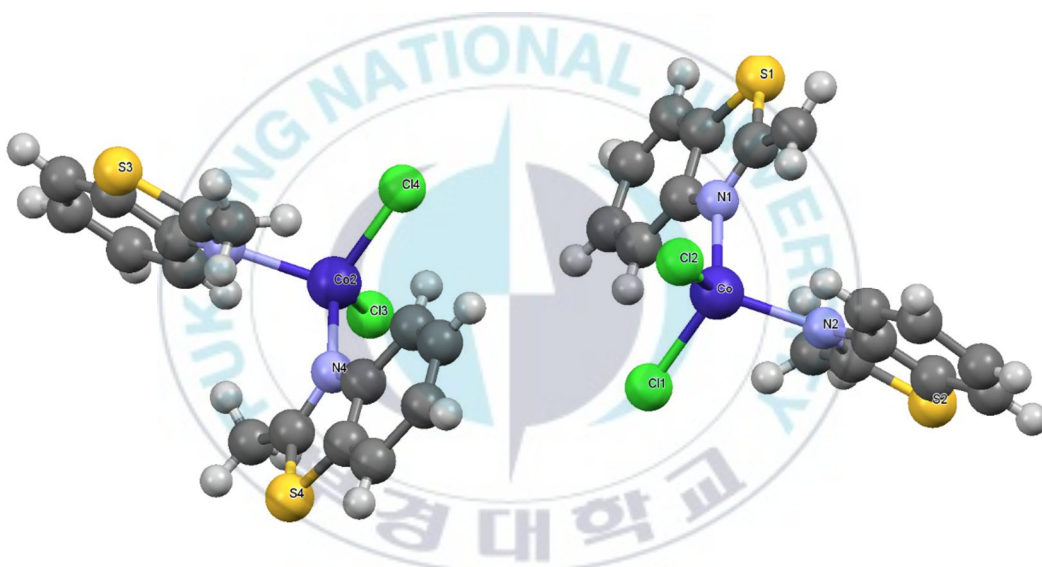


Figure 3.3. X-ray structure of dichloro-bis(2-methylbenzothiazole) cobalt(II) Co3.

3.3.3 Determination of minimal inhibitory concentration: The MICs of Co1-3 were summarized in Table 3.4. Gram-positive and Gram-negative bacteria have dissimilar outer membrane. Gram-positive bacteria have a thick membrane made up of peptidoglycan and teichoic acids. Gram-negative bacteria have a thin membrane comprising a few peptidoglycan layers surrounded by the outer lipid membrane containing lipopolysaccharides and lipoproteins. Therefore, the

reactivity of unlike compounds has diverse interactions with Gram-positive and Gram-negative bacteria (Asekunowo et al. 2015; El-Sherif 2010).

Ligands **L1**, **L2**, and **L3** were ineffective against tested strains of bacteria. The coordination of **L1**, **L2**, and **L3** with Co(II) improved their bacteriostatic activity. **CoCl₂** was bacteriostatic against all the tested strains of bacteria, excluding *L. monocytogenes*. The bacteriostatic activity of **CoCl₂** was high against *S. aureus*, moderate against MRSA, *E. faecalis*, and *K. pneumoniae*, but low against *B. subtilis*, *E. coli*, *S. Typhimurium*, and *V. parahaemolyticus*. **Co1-3** were bacteriostatic against MRSA, *S. aureus*, *B. subtilis*, *E. faecalis*, *S. typhimurium*, and *V. parahaemolyticus*, but ineffective against *E. coli* and *K. pneumoniae*. **Co1-3** were more bacteriostatic against MRSA compared to streptomycin. The bacteriostatic activity of **Co2**, **Co3**, and streptomycin was parallel against *S. aureus*. The bacteriostatic activity of **Co1** was twice against *S. aureus* than against MRSA, *E. faecalis*, *S. typhimurium*, and *V. parahaemolyticus*. The bacteriostatic activity of **Co2** and **Co3** was similar against the tested bacteria, excluding *L. monocytogenes*. The bacteriostatic activity of **Co2** and **Co3** maximum against MRSA, *S. aureus*, *B. subtilis*, and *V. parahaemolyticus*. The bacteriostatic activity of **Co2** and **Co3** was low against *E. faecalis* and *S. typhimurium*. Overall, the bacteriostatic activity of **Co2** and **Co3** were 4-fold against MRSA, *S. aureus*, and *V. parahaemolyticus* than **Co1**. The bacteriostatic activity of **Co2** and **Co3** was highest against *S. aureus* than other tested bacteria.

The bacteriostatic activity of **Co1-3** was improved significantly in comparison to their ligands **L1-L3**, respectively. Similarly, **Co2** and **Co3** showed high bacteriostatic activity compared to a **CoCl₂** against MRSA, *S. aureus*, *B. subtilis*, and *V. parahaemolyticus*. The heteroatom of the azole ring might play important role in the bacteriostatic activity of **Co1-3** due to its well-known cell membrane interacting ability. The MIC values of **Co2** and **Co3** were low against *S. aureus* and *B. subtilis* in comparison to the cobalt complexes reported in the literature (Vlaicu et al. 2019). Therefore, **Co1-3** may be considered as promising antibacterial agents.

Table 3.4. MIC ($\mu\text{g/mL}$) values of the complexes **Co1-3**.

Bacteria		Co1	Co2	Co3	L1	L2	L3	CoCl ₂	STR
Gram Positive Bacteria	MRSA	200 \pm 0.006	50 \pm 0.016	50 \pm 0.005	-	-	-	100 \pm 0.001	-
	<i>S. aureus</i>	50 \pm 0.007	12.5 \pm 0.005	12.5 \pm 0.002	-	-	-	50 \pm 0.003	12.5 \pm 0.008
	<i>B. subtilis</i>	-	25 \pm 0.008	25 \pm 0.001	-	-	-	200 \pm 0.007	6.25 \pm 0.001
	<i>E. faecalis</i>	200 \pm 0.005	200 \pm 0.001	200 \pm 0.0003	-	-	-	100 \pm 0.016	6.25 \pm 0.003
	<i>L. monocytogenes</i>	-	-	200 \pm 0.003	-	-	-	-	1.526 \pm 0.0003
	<i>E. coli</i>	-	-	-	-	-	-	200 \pm 0.005	6.25 \pm 0.050
Gram Negative Bacteria	<i>S. typhimurium</i>	200 \pm 0.005	200 \pm 0.011	200 \pm 0.0002	-	-	-	200 \pm 0.003	12.5 \pm 0.002
	<i>K. pneumoniae</i>	-	-	-	-	-	-	100 \pm 0.006	12.5 \pm 0.005
	<i>V. parahaemolyticus</i>	200 \pm 0.001	50 \pm 0.017	50 \pm 0.0006	-	-	-	200 \pm 0.014	1.526 \pm 0.001

3.3.4 Synergistic effect: The synergistic effect of the test compounds (ligands **L1-L3**, **CoCl₂**, and complexes **Co1-3**) and antibiotics AMP, CHL, NEO, KAN, PEN, and STR against MRSA is presented in Table 3.5. The results of the checkerboard assay showed that the MIC was reduced ≥ 2 -fold in all combinations, producing a synergistic effect between the combinations as follows: **Co1** with AMP, KAN, NEO, and STR, **Co2** with AMP, NEO, PEN, and STR, and **Co3** with AMP, NEO, and STR, **L1** with CHL, KAN, NEO, and PEN, **L2** with NEO, **L3** with KAN, NEO and STR, and **CoCl₂** with AMP, KAN, PEN, and STR, having a fractional inhibitory concentration index (FICI) ranging from 0.035 to 0.5. The combinations of **Co1** with PEN, **Co2** with CHL and KAN, and **Co3** with CHL, KAN, and PEN showed a partial synergy with FICI ranging from 0.515 to 0.75. An additive effect was found in the combination of **Co1** and CHL with a FICI value of 1.

Co2, **CoCl₂**, and ligand **L1** showed synergy with PEN, whereas **Co1** and **Co3**, and ligands **L2** and **L3** showed partial synergy with PEN. Strait *et al.* found the 4- to 8- fold more antibacterial activity of penicillin against *S. aureus* in combination with a trace amount of **CoCl₂.6H₂O** (STRAIT *et al.* 1948). Similarly, penicillin in the combination of **Co2**, **CoCl₂**, and ligand **L1** showed 4, 4, and 8- fold increase in antibacterial activity against MRSA, respectively. **Co1-3** exhibited an 8-fold more synergy with AMP compared to anhydrous **CoCl₂**. Ligands **L1-L3** did not show synergy with AMP. The strong synergy of **Co1-3** with AMP may be caused by the formation of a new complex (Deng *et al.* 2016). According to the synergistic results, the combination of **Co1-3** with AMP was selected for the mechanical study.

Table 3.5. Synergistic activity of the complexes **Co1-3** against MRSA.

Combination		MRSA		
Antibiotic	Complexes	FIC	FICI	Remark
Ampicillin	Co1	0.004 / 0.031	0.035	Synergy
Chloramphenicol		0.500 / 0.500	1.000	Additive
Kanamycin		0.250/ 0.062	0.312	Synergy
Neomycin		0.250 / 0.125	0.375	Synergy
Penicillin		0.250 / 0.500	0.750	Partial Synergy
Streptomycin		0.015 /0.125	0.140	Synergy
Ampicillin	Co2	0.008 / 0.031	0.039	Synergy
Chloramphenicol		0.500 / 0.031	0.531	Partial Synergy
Kanamycin		0.250 / 0.500	0.750	Partial Synergy
Neomycin		0.125 / 0.250	0.375	Synergy
Penicillin		0.250 / 0.250	0.500	Synergy
Streptomycin		0.031 / 0.250	0.281	Synergy
Ampicillin	Co3	0.008 / 0.031	0.039	Synergy
Chloramphenicol		0.242 / 0.500	0.742	Partial Synergy
Kanamycin		0.015 / 0.500	0.515	Partial Synergy
Neomycin		0.250 / 0.250	0.500	Synergy
Penicillin		0.030 / 0.500	0.530	Partial Synergy
Streptomycin		0.125 / 0.031	0.156	Synergy
Ampicillin	L1	1.000/0.063	1.063	Indifference
Chloramphenicol		0.004/1.000	1.004	Indifference
Kanamycin		0.063/0.063	0.126	Synergy
Neomycin		0.063/0.063	0.126	Synergy
Penicillin		0.063/0.260	0.323	Synergy
Streptomycin		0.063/0.125	0.188	Synergy
Ampicillin	L2	0.039/1.000	1.039	Indifference
Chloramphenicol		0.016/1.000	1.016	Indifference
Kanamycin		0.039/1.000	1.039	Indifference
Neomycin		0.063/0.250	0.313	Synergy
Penicillin		0.500/0.250	0.750	Partial Synergy
Streptomycin		0.500/0.125	0.625	Partial Synergy
Ampicillin	L3	0.039/1.000	1.039	Indifference
Chloramphenicol		0.125/0.500	0.625	Partial Synergy
Kanamycin		0.063/0.063	0.126	Synergy
Neomycin		0.250/0.125	0.375	Synergy

Penicillin		0.063/0.500	0.563	Partial Synergy
Streptomycin		0.250/0.125	0.375	Synergy
Ampicillin	CoCl ₂	0.063/0.250	0.313	Synergy
Chloramphenicol		0.063/0.500	0.563	Partial Synergy
Kanamycin		0.125/0.063	0.188	Synergy
Neomycin		0.500/0.030	0.530	Partial Synergy
Penicillin		0.125/0.125	0.250	Synergy
Streptomycin		0.250/0.125	0.375	Synergy

3.3.5 SYTOX green uptake assay: A few OC showed bacterial membrane disruption as their antibacterial mechanism (Nandanwar and Kim 2019). SYTOX green assay was performed to find the cell membrane destruction behavior of **Co1-3** and **Co1-3 + AMP**. SYTOX green dye has a strong affinity for DNA but lacks the ability to cross the bacterial membrane. Only in the presence of broken bacteria SYTOX green dye can interact with bacterial DNA and show fluorescence. There is a direct relation between the rise in fluorescence of SYTOX green dye and membrane crossing. The rise in fluorescence represents the damaged membrane of bacteria (Li et al. 2012).

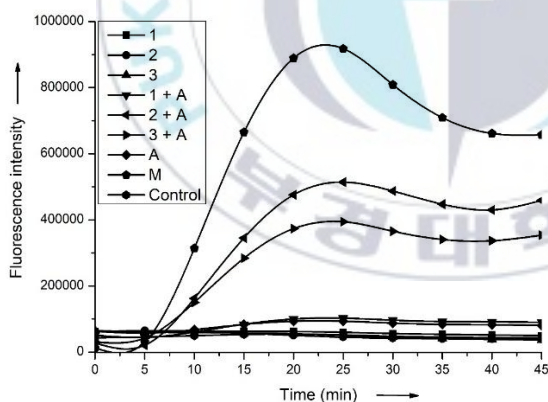


Figure 3.4. Kinetics of MRSA membrane crossing by the Co1-3, AMP, and Co1-3 + AMP at $3 \times \text{MIC}$. The positive control melittin is also shown.

In this assay, a well-known membrane crossing peptide, melittin, was kept as positive control (Rajasekaran, Kim, and Shin 2017). The positive control displayed higher fluorescence intensity (Figure 3.4) within 22 min of incubation. Fluorescence intensity was also enhanced in presence of Co2 + AMP and Co3 +

AMP, indicating their membrane crossing behavior. **Co1-3**, AMP, and **Co1 + AMP** did not show any rise in fluorescence. The fluorescence intensity of **Co1-3** was steady up to 10 min of incubation, which decreased later below control and continued at the same level (Taute et al. 2015). These results revealed the different antibacterial mechanism of a **Co1-3**.

The coordination of AMP to Co(II) ion may reduce the polarity of Co(II) ion (Fekri et al. 2017). The reduction of polarity introduces lipophilicity in the complex. Lipophilic complexes can easily cross the lipid membrane of bacteria, leading to the death of bacteria. Therefore, bacterial cell membrane disruption is the possible antibacterial mechanism of **Co2 + AMP** or **Co3 + AMP**.

3.4 Conclusion

In this study, the cobalt(II) complexes **Co1-3** were successfully synthesized and characterized by UV-vis spectroscopy, FT-IR spectroscopy, and X-ray crystallography. Our investigation has shown that the **Co1-3** were bacteriostatic against tested bacteria, except for *E. coli* and *K. pneumoniae*. **Co1-3** had higher bacteriostatic activity against MRSA compared to streptomycin. **Co2** and **Co3** had parallel bacteriostatic activity compared to streptomycin against *S. aureus*. **Co1-3** exhibited synergy, partial synergy, and additive effect with antibiotics against MRSA. Further, **Co2 + AMP** and **Co3 + AMP** had membrane destruction as a possible mechanism of action. **Co1-3** and **Co1-3 + antibiotic** significant growth inhibition of antibiotic-resistant bacteria, which could be beneficial for advanced biological studies in the future.

3.5 Experimental Section

3.5.1 Materials, instrumentation, and physical measurements: The chemicals used for this study are anhydrous cobalt(II) chloride (CoCl_2), 2-methylbenzimidazole (**L1**), 2-methylbenzoxazole (**L2**), 2-methylbenzothiazole (**L3**), dichloromethane (DCM), ampicillin (AMP), penicillin (PEN), streptomycin (STR), kanamycin (KAN), chloramphenicol (CHL), neomycin (NEO), acetonitrile, Luria Bertani broth (LB), trisodium citrate, sodium chloride (NaCl), melittin, and SYTOX green dye.

3.5.2 General method for the synthesis of Co1-3

Metal salts (MCl_2) and ligands (**L1-L3**) were mixed in a 1:2 molar ratio into two 100 mL round bottom flasks each. Twenty mL of DCM was added to each flask and kept for stirring at room temperature. After 10 min ligand solution was dropped slowly into metal salt suspension. The stirring was continued for 15 min at room temperature to react the ligands with MCl_2 (scheme 1). The obtained crystal was filtered and washed with DCM for the removal of unreacted ligands. Excess DCM was vaporized using a rotary evaporator and obtained thick solution was air-dried. Obtained crystals were washed three times with hexane, filtered, and recrystallized with acetonitrile at room temperature. Then, the crystals were characterized by UV-Vis analysis, and Single-X-Ray analysis for molecular structure determination.

Dichloro-bis(2-methylbenzimidazole)cobalt(II) (Co1): Yield: 81 % (Blue crystals). Anal. Calcd. C 48.75, H 4.09, Cl 17.99, Co 14.95, N 14.21. IR (solid state): $\nu(\text{C}=\text{N}) \text{ cm}^{-1}$ 1537, 1554, 1578, 1595, 1604, $\nu(\text{C}=\text{C}) \text{ cm}^{-1}$ 1386, 1416, $\nu(\text{C}-\text{N}) \text{ cm}^{-1}$ 1247, 1271, $\nu(\text{Co}-\text{N}) \text{ cm}^{-1}$ 481, 499, $\nu(\text{C}-\text{H}/\text{CH}_3 \text{ aliphatic}) \text{ cm}^{-1}$ 2918, $\nu(\text{C}-\text{H aromatic}) \text{ cm}^{-1}$ 2996, (KBr disk); UV-vis (1 % DMSO) λ_{max} , nm ($\log \epsilon$, $\text{L mol}^{-1} \text{ cm}^{-1}$): 241 (4.34), 273 (4.37).

Dichloro-bis(2-methylbenzoxazole)cobalt(II) (Co2): Yield: 90 % (Blue

crystals). Anal. Calcd. C, 48.51; H, 3.56; Cl, 17.90; Co, 14.88; N, 7.07; O, 8.08. IR (solid state): $\nu(\text{C}=\text{N}) \text{ cm}^{-1}$ 1456, 1473, 1515, 1557, 1602, $\nu(\text{C}=\text{C}) \text{ cm}^{-1}$ 1340, 1359, $\nu(\text{C}-\text{N}) \text{ cm}^{-1}$ 1242, 1301, $\nu(\text{C}-\text{O}) \text{ cm}^{-1}$ 1149, 1165, 1180 $\nu(\text{Co}-\text{N}) \text{ cm}^{-1}$ 499, $\nu(\text{C}-\text{H}/\text{CH}_3 \text{ aliphatic}) \text{ cm}^{-1}$ 2913, 2942, $\nu(\text{C}-\text{H aromatic}) \text{ cm}^{-1}$ 3012, 3038, (KBr disk); UV-vis (1 % DMSO) λ_{max} , nm ($\log \epsilon$, $\text{L mol}^{-1} \text{ cm}^{-1}$): 218 (4.31).

Preparation of dichloro-bis(2-methylbenzothiazole)cobalt(II) (Co3): Yield: 91 % (Blue crystals). Anal. Calcd. C, 44.87; H, 3.29; Cl, 16.56; Co, 13.76; N, 6.54; S, 14.97. IR (solid state): $\nu(\text{C}=\text{N}) \text{ cm}^{-1}$ 1532, 1541, 1567, 1591, 1608, $\nu(\text{C}=\text{C}) \text{ cm}^{-1}$ 1379, 1437, $\nu(\text{C}-\text{N}) \text{ cm}^{-1}$ 1242, 1284, 1322, $\nu(\text{C}-\text{S}) \text{ cm}^{-1}$ 669, 709, $\nu(\text{Co}-\text{N}) \text{ cm}^{-1}$ 478, 511, $\nu(\text{C}-\text{H}/\text{CH}_3 \text{ aliphatic}) \text{ cm}^{-1}$ 2913, $\nu(\text{C}-\text{H aromatic}) \text{ cm}^{-1}$ 3000, (KBr disk); UV-vis (1 % DMSO) λ_{max} , nm ($\log \epsilon$, $\text{L mol}^{-1} \text{ cm}^{-1}$): 252 (4.24).

3.5.3 Antibacterial assay:

The minimum concentration of drugs restricting the visible growth of bacteria is defined as minimum inhibitory concentration. A two-fold serial dilution method was used to perform bacterial growth inhibition assay. The test compounds used were ligands **L1-L3**, **Co1-3**, **CoCl₂**, and streptomycin (antibiotic control). Two-fold serially diluted solutions of test compounds were prepared 1% DMSO using standard protocol²². Hundred μL inoculum of overnight grown Gram-positive bacteria (methicillin-resistant *S. aureus* (MRSA), *S. aureus*, *B. subtilis*, and *E. faecalis*) and Gram-negative bacteria (*E. coli*, *K. pneumonia*, and *S. typhimurium*) at 37 °C was mixed with 100 μL of diluted test solutions in sterile 96 well plate. The final concentration of test compounds and bacteria was 1.562 to 200 $\mu\text{g}/\text{mL}$ and $\sim 2 \times 10^5 \text{ CFU mL}^{-1}$. The control of bacteria, %DMSO, and water was used to eliminate background value. These plates were incubated at 37 °C, and the optical density (OD) of the plates was recorded 650 nm after 18 h. MIC of the test compounds was calculated by subtracting the OD of blank from the OD of the sample. The experiments were carried out in three replicates, and the data are presented as mean standard error (SE).

3.5.4 Checkerboard dilution test: The combination effects between test compounds (ligands **L1-L3**, **CoCl₂**, and **Co1-3**) and antibiotics (AMP, CHL, NEO, KAN, PEN, and STR) for growth inhibition of *MRSA* were estimated using micro-broth checkerboard test (Mun et al. 2013). 1:1 (v/v) ratio of serially two-fold diluted aliquots of test compounds and antibiotics were mixed with the LB broth in the 96-well microtiter plate. Hundred μL inoculum of *MRSA* suspension was added to the above solution to give a final cell concentration of 2×10^6 CFU/mL. **Co1-3** and inoculum controls were kept in the last two wells. The MIC was determined after 18 hours of incubation at 37 °C. Fractional inhibitory concentration (FIC) was calculated for the first clear well in each row of the microtiter plate containing all antimicrobial agents. The FIC index (FICI) was calculated using the following formula:

$$\text{FIC index} = \text{FICA} + \text{FICB} = [\text{A}] / \text{MICA} + [\text{B}] / \text{MICB}$$

where [A] and [B] are the concentrations of drugs A and B, respectively, MICA and MICB are the minimum inhibitory concentrations of A and B for the organism, and FICA and FICB are fractional inhibitory concentrations of A and B, respectively. The calculated FIC index was elucidated as the following: $\text{FICI} \leq 0.5$ indicating synergy, $\text{FICI} = 0.5\text{-}0.75$ indicating partial synergy, $\text{FICI} = 0.76\text{-}1$ indicating an additive effect, $\text{FICI} = 1\text{-}4$ indicating indifference, and $\text{FICI} >4$ indicating antagonism.

3.5.5 SYTOX green uptake assay: It was performed to determine the membrane crossing ability of the compounds (Borkar et al. 2019; Rajasekaran et al. 2019). Briefly, the overnight grown culture of *MRSA* was washed with standard buffer. The washed cells were suspended into the same buffer. The cell suspensions were mixed with 0.5 μM SYTOX green dye and incubated for 15 min at 37 °C in the dark. The above mixture was treated with **Co1-3**, AMP, and **Co1-3** + AMP to give a final concentration equal to $3 \times \text{MIC}$. The kinetics of treated samples were

supervised on Microplate Reader with filter wavelengths of 485 and 535 nm for excitation and emission, respectively. Control experiments were performed under the same conditions without the addition of any tested compound, and the corresponding results were subtracted from those obtained with the complexes studied. Melittin (a toxin from bee venom) was used as a positive control.



3.6 References

- Abdel-Wahab, Bakr F., Ghada E. A. Awad, and Farid A. Badria. 2011. "Synthesis, Antimicrobial, Antioxidant, Anti-Hemolytic and Cytotoxic Evaluation of New Imidazole-Based Heterocycles." *European Journal of Medicinal Chemistry* 46(5):1505–11.
- Abu-Dief, Ahmed M., and Ibrahim M. A. Mohamed. 2015. "A Review on Versatile Applications of Transition Metal Complexes Incorporating Schiff Bases." *Beni-Suef University Journal of Basic and Applied Sciences* 4(2):119–33.
- Akhtar, Muhammad Nadeem, William T. A. Harrison, Muhammad Shahid, Islam Ullah Khan, Ejaz, and Javed Iqbal. 2016. "Synthesis, Crystal Structure and Biological Activity of a Cobalt(II) Complex of N,N,N',N'-Tetrakis(2-Hydroxypropyl) Ethylenediamine." *Transition Metal Chemistry* 41(3):325–30.
- Asekunowo, Patrick O., Rosenani A. Haque, Mohd R. Razali, and Srinivasa Budagumpi. 2015. "Benzimidazole-Based Silver(I)-N-Heterocyclic Carbene Complexes as Anti-Bacterials: Synthesis, Crystal Structures and Nucleic Acids Interaction Studies." *Applied Organometallic Chemistry* 29(3):126–37.
- Behravesh, Casey Barton, Timothy F. Jones, Duc J. Vugia, Cherie Long, Ruthanne Marcus, Kirk Smith, Stephanie Thomas, Shelley Zansky, Kathleen E. Fullerton, Olga L. Henao, and Elaine Scallan. 2011. "Deaths Associated with Bacterial Pathogens Transmitted Commonly through Food: Foodborne Diseases Active Surveillance Network (FoodNet), 1996-2005." *Journal of Infectious Diseases* 204(2):263–67.
- Bello-Vieda, Nestor J., Homero F. Pastrana, Manuel F. Garavito, Alba G. Ávila, Adriana M. Celis, Alvaro Muñoz-Castro, Silvia Restrepo, and John J. Hurtado. 2018. "Antibacterial Activities of Azole Complexes Combined with Silver Nanoparticles." *Molecules* 23(2):1–17.

- Borkar, Shweta Bharat, Sondavid K. Nandanwar, Jun Hyuck Lee, and Hak Jun Kim. 2019. "Characterization of Four Liver-Expressed Antimicrobial Peptides from Antarctic Fish and Their Antibacterial Activity." *Applied Sciences* 9(October):4299.
- Brahma, Umarani, Paresh Sharma, Shweta Murthy, Savitri Sharma, Shalini Chakraborty, Sundarapu Naga Appalaraju, and Vasundhra Bhandari. 2019. "Decreased Expression of FemXAB Genes and Fnbp Mediated Biofilm Pathways in OS-MRSA Clinical Isolates." *Scientific Reports* 9(1):1–8.
- Chang, Eddie L., Christa Simmers, and D. Andrew Knight. 2010. "Cobalt Complexes as Antiviral and Antibacterial Agents." *Pharmaceuticals* 3(6):1711–28.
- Cherian, Philip T., Aditi Deshpande, Martin N. Cheramie, David F. Bruhn, Julian G. Hurdle, and Richard E. Lee. 2017. "Design, Synthesis and Microbiological Evaluation of Ampicillin-Tetramic Acid Hybrid Antibiotics." *Journal of Antibiotics* 70(1):65–72.
- Datta, Amitabha, Kuheli Das, Chandana Sen, Nirmal Kumar Karan, Jui Hsien Huang, Chia Her Lin, Eugenio Garribba, Chittaranjan Sinha, Tulin Askun, Pinar Celikboyun, and Sandeep B. Mane. 2015. "Doubly End-on Azido Bridged Mixed-Valence Cobalt Trinuclear Complex: Spectral Study, VTM, Inhibitory Effect and Antimycobacterial Activity on Human Carcinoma and Tuberculosis Cells." *Spectrochimica Acta - Part A: Molecular and Biomolecular Spectroscopy* 148(April):427–34.
- Deng, Hua, Danielle McShan, Ying Zhang, Sudarson S. Sinha, Zikri Arslan, Paresh C. Ray, and Hongtao Yu. 2016. "Mechanistic Study of the Synergistic Antibacterial Activity of Combined Silver Nanoparticles and Common Antibiotics." *Environmental Science and Technology* 50(16):8840–48.

- Devi, J., M. Yadav, D. Kumar, L. S. Naik, and D. K. Jindal. 2019. "Some Divalent Metal(II) Complexes of Salicylaldehyde-Derived Schiff Bases: Synthesis, Spectroscopic Characterization, Antimicrobial and in Vitro Anticancer Studies." *Applied Organometallic Chemistry* 33(2):1–22.
- El-Sawaf, Ayman K., Farag El-Essawy, Amal A. Nassar, and El Sayed A. El-Samanody. 2018. "Synthesis, Spectral, Thermal and Antimicrobial Studies on Cobalt(II), Nickel(II), Copper(II), Zinc(II) and Palladium(II) Complexes Containing Thiosemicarbazone Ligand." *Journal of Molecular Structure* 1157:381–94.
- El-Sherif, Ahmed A. 2010. "Synthesis, Solution Equilibria and Antibacterial Activity of Co(II) with 2-(Aminomethyl)-Benzimidazole and Dicarboxylic Acids." *Journal of Solution Chemistry* 39(10):1562–81.
- El-Wakiel, Nadia, Mai El-Keiy, and Mohamed Gaber. 2015. "Synthesis, Spectral, Antitumor, Antioxidant and Antimicrobial Studies on Cu(II), Ni(II) and Co(II) Complexes of 4-[(1H-Benzoimidazol-2-Ylimino)-Methyl]-Benzene-1,3-Diol." *Spectrochimica Acta - Part A: Molecular and Biomolecular Spectroscopy* 147:117–23.
- Fekri, Roghayeh, Mehdi Salehi, Asadollah Asadi, and Maciej Kubicki. 2017. "DNA/BSA Interaction, Bio-Activity, Molecular Docking Simulation Study and Electrochemical Properties of Hydrazone Schiff Base Derived Cu(II)/Ni(II) Metal Complexes: Influence of the Nuclearity and Metal Ions." *Polyhedron* 128:175–87.
- Hubin, Timothy J., Prince N. A. Amoyaw, Kimberly D. Roewe, Natalie C. Simpson, Randall D. Maples, Tarynn N. Carder Freeman, Amy N. Cain, Justin G. Le, Stephen J. Archibald, Shabana I. Khan, Babu L. Tekwani, and M. O. Faru. Khan. 2014. "Synthesis and Antimalarial Activity of Metal Complexes of Cross-Bridged Tetraazamacrocyclic Ligands." *Bioorganic and Medicinal*

Chemistry 22(13):3239–44.

- Kaka, Anjum S., Adriana M. Rueda, Samuel A. Shelburne, Kristina Hulten, Richard J. Hamill, and Daniel M. Musher. 2006. “Bactericidal Activity of Orally Available Agents against Methicillin-Resistant *Staphylococcus Aureus*.” *Journal of Antimicrobial Chemotherapy* 58(3):680–83.
- Khan, Huzaifa Yasir, Mohd Owais Ansari, G. G. H. A. Shadab, Sartaj Tabassum, and Farukh Arjmand. 2019. “Evaluation of Cytotoxic Activity and Genotoxicity of Structurally Well Characterized Potent Cobalt(II) Phen-Based Antitumor Drug Entities: An in Vitro and in Vivo Approach.” *Bioorganic Chemistry* 88(April):102963.
- Kumar, Amit, Ashish Kumar, Rakesh Kumar Gupta, Rajendra Prasad Paitandi, Krishna Beer Singh, Surendra Kumar Trigun, Maninder Singh Hundal, and Daya Shankar Pandey. 2016. “Cationic Ru(II), Rh(III) and Ir(III) Complexes Containing Cyclic π -Perimeter and 2-Aminophenyl Benzimidazole Ligands: Synthesis, Molecular Structure, DNA and Protein Binding, Cytotoxicity and Anticancer Activity.” *Journal of Organometallic Chemistry* 801:68–79.
- Lai, Xiaoxu, Ronghui Guo, Jianwu Lan, Liang Geng, Shaojian Lin, Shouxiang Jiang, Yong Zhang, Hongyan Xiao, and Cheng Xiang. 2019. “Flexible Reduced Graphene Oxide/Electroless Copper Plated Poly(Benzo)-Benzimidazole Fibers with Electrical Conductivity and Corrosion Resistance.” *Journal of Materials Science: Materials in Electronics* 30(3):1984–92.
- Li, Lirong, Yonghui Shi, Guanfang Su, and Guowei Le. 2012. “Selectivity for and Destruction of *Salmonella Typhimurium* via a Membrane Damage Mechanism of a Cell-Penetrating Peptide PpTG20 Analogue.” *International Journal of Antimicrobial Agents* 40(4):337–43.
- Luo, Tao, Oana David, Youri Gendel, and Matthias Wessling. 2016. “Porous

Poly(Benzimidazole) Membrane for All Vanadium Redox Flow Battery.” *Journal of Power Sources* 312:45–54.

Mahmood, Khalid, Waleed Hashmi, Hammad Ismail, Bushra Mirza, Brendan Twamley, Zareen Akhter, Isabel Rozas, and Robert J. Baker. 2019. “Synthesis, DNA Binding and Antibacterial Activity of Metal(II) Complexes of a Benzimidazole Schiff Base.” *Polyhedron* 157:326–34.

Malik, Manzoor Ahmad, Ovas Ahmad Dar, Parveez Gull, Mohmmad Younus Wani, and Athar Adil Hashmi. 2018. “Heterocyclic Schiff Base Transition Metal Complexes in Antimicrobial and Anticancer Chemotherapy.” *MedChemComm* 9:409–36.

Moll, Rachel, and Bernard Davis. 2017. “Iron, Vitamin B12 and Folate.” *Medicine (United Kingdom)* 45(4):198–203.

Mun, Su Hyun, Dae Ki Joung, Yong Sik Kim, Ok Hwa Kang, Sung Bae Kim, Yun Soo Seo, Youn Chul Kim, Dong Sung Lee, Dong Won Shin, Kee Tae Kweon, and Dong Yeul Kwon. 2013. “Synergistic Antibacterial Effect of Curcumin against Methicillin-Resistant Staphylococcus Aureus.” *Phytomedicine* 20(8–9):714–18.

Munteanu, Catherine R., and K. Suntharalingam. 2015. “Advances in Cobalt Complexes as Anticancer Agents.” *Dalton Transactions* 44(31):13796–808.

Nandanwar, Sondavid K., and Hak Jun Kim. 2019. “Anticancer and Antibacterial Activity of Transition Metal Complexes.” *ChemistrySelect* 4(5):1706–21.

Patel, Mohan N., Promise A. Dosi, and Bhupesh S. Bhatt. 2012. “Nucleic Acid Interaction and Antibacterial Behaviours of a Ternary Palladium(II) Complexes.” *Spectrochimica Acta - Part A: Molecular and Biomolecular Spectroscopy* 86:508–14.

Rajasekaran, Ganesan, S. Dinesh Kumar, Jiyoung Nam, Dasom Jeon, Yangmee

- Kim, Chul Won Lee, Il Seon Park, and Song Yub Shin. 2019. "Antimicrobial and Anti-Inflammatory Activities of Chemokine CXCL14-Derived Antimicrobial Peptide and Its Analogs." *Biochimica et Biophysica Acta - Biomembranes* 1861(1):256–67.
- Rajasekaran, Ganesan, Eun Young Kim, and Song Yub Shin. 2017. "LL-37-Derived Membrane-Active FK-13 Analogs Possessing Cell Selectivity, Anti-Biofilm Activity and Synergy with Chloramphenicol and Anti-Inflammatory Activity." *Biochimica et Biophysica Acta - Biomembranes* 1859(5):722–33.
- Sánchez-Guadarrama, Obdulia, Horacio López-Sandoval, Francisco Sánchez-Bartéz, Isabel Gracia-Mora, Herbert Höpfl, and Noráh Barba-Behrens. 2009. "Cytotoxic Activity, X-Ray Crystal Structures and Spectroscopic Characterization of Cobalt(II), Copper(II) and Zinc(II) Coordination Compounds with 2-Substituted Benzimidazoles." *Journal of Inorganic Biochemistry* 103(9):1204–13.
- Schatzschneider, Ulrich. 2019. *Antimicrobial Activity of Organometal Compounds*. Elsevier Inc.
- STRAIT, L. A., J. DUFRENOY, and R. PRATT. 1948. "Enhancement of Penicillin Effectiveness by Traces of Cobalt." *Journal of the American Pharmaceutical Association. American Pharmaceutical Association* 37(4):133–35.
- Tarte, Naresh H., Hyun Yong Cho, and Seong Ihl Woo. 2007. "Efficient Route for Cyclic Olefin Polymerization: Nonchelated Monodentate Benzimidazole Nickel(II) Complex Catalysts for Vinyl Polymerization of Norbornene." *Macromolecules* 40(23):8162–67.
- Tarte, Naresh H., Seong Ihl Woo, Liqiang Cui, Young Dae Gong, and Young Ho Hwang. 2008. "Novel Non-Chelated Cobalt(II) Benzimidazole Complex Catalysts: Synthesis, Crystal Structures and Cocatalyst Effect in Vinyl

Polymerization of Norbornene.” *Journal of Organometallic Chemistry* 693(4):729–36.

Taute, Helena, Megan J. Bester, Albert W. H. Neitz, and Anabella R. M. Gaspar. 2015. “Investigation into the Mechanism of Action of the Antimicrobial Peptides Os and Os-C Derived from a Tick Defensin.” *Peptides* 71(6):179–87.

Vlaicu, Ioana Dorina, Rodica Olar, Cătălin Maxim, Mariana Carmen Chifiriuc, Coralia Bleotu, Nicolae Stănică, Gina Vasile Scăețeanu, Constanța Dulea, Speranța Avram, and Mihaela Badea. 2019. “Evaluating the Biological Potential of Some New Cobalt (II) Complexes with Acrylate and Benzimidazole Derivatives.” *Applied Organometallic Chemistry* (April):1–13.

Węglarz-Tomczak, Ewelina, Małgorzata Burda-Grabowska, Mirosław Giurg, and Artur Mucha. 2016. “Identification of Methionine Aminopeptidase 2 as a Molecular Target of the Organoselenium Drug Ebselen and Its Derivatives/Analogues: Synthesis, Inhibitory Activity and Molecular Modeling Study.” *Bioorganic and Medicinal Chemistry Letters* 26(21):5254–59.

Yadav, Geeta, and Swastika Ganguly. 2015. “Structure Activity Relationship (SAR) Study of Benzimidazole Scaffold for Different Biological Activities: A Mini-Review.” *European Journal of Medicinal Chemistry* 97(1):419–43.

Zhang, Hui Zhen, Guri L. V. Damu, Gui Xin Cai, and Cheng He Zhou. 2013. “Design, Synthesis and Antimicrobial Evaluation of Novel Benzimidazole Type of Fluconazole Analogues and Their Synergistic Effects with Chloromycin, Norfloxacin and Fluconazole.” *European Journal of Medicinal Chemistry* 64:329–44.



Part II Algal growth inhibition and dye degradation efficiency of synthetic MoZnO and Cu-VO



Chapter 4

Synthesis, Characterization, and Anti-algal Activity of Molybdenum Doped Metal Oxides

4.1 Abstract: In this study, we attempted to synthesize visible light active nano-sized photocatalysts using metal oxides such as zinc oxide, zirconium oxide, tungsten oxide, and strontium titanium oxide with $(\text{MoCl}_5)_2$ as a dopant by the simple ball-milling method. FT-IR data confirmed the presence of M-O-Mo linkage (M= Zn, Zr, W, and SrTi) in all the molybdenum-doped metal oxides (MoMOs), but only MoZnO inhibited the growth of the bloom-forming *Microcystis aeruginosa* under visible light in a concentration-dependent manner up to 10 mg/L. Further, structural characterization of MoZnO using FESEM and XRD exhibited the formation of typical hexagonal wurtzite nanocrystals of approximately 4 nm. Hydroxyl radical ($\cdot\text{OH}$), reactive oxygen species (ROS), and lipid peroxidation assays revealed $\cdot\text{OH}$ generated by MoZnO under the visible light seemed to cause peroxidation of the lipid membrane of *M. aeruginosa*, which lead to an upsurge of intracellular ROS and consequently introduced agglomeration of cyanobacteria. These results demonstrated that nano-sized MoZnO photocatalyst can be easily synthesized in a cost-effective ball-mill method and be utilized for biological applications such as the reduction of harmful algal blooms. Further, our study implies that a simple ball-milling method can provide an easy, green, and scalable route for the synthesis of visible light active doped metal oxides.

4.2 Introduction

Photocatalysts are vital photoactive materials that could help eliminate the global energy crisis and mitigate environmental pollution (Theerthagiri et al. 2019). Photocatalysts generate electrons in the conduction band and holes in the valence band upon illumination with higher light energy compared to its bandgap (Lebedev et al. 2018). These photogenerated electrons and holes can oxidize or reduce surrounding pollutants with suitable redox potentials. However, some photocatalysts such as zinc oxide (ZnO), zirconium oxide (ZrO₂), and strontium-titanium oxide (SrTiO₃) have higher photocatalytic efficiency under ultraviolet (UV) light compared to visible light (Ding et al. 2019; Shu, Jiao, and Chen 2012; Yan et al. 2013), meaning an external energy source is needed to activate these photocatalysts. Tungsten oxide (WO₃) has also a poor activity under visible light (Kalanur and Seo 2018). Therefore, it is important to synthesize visible light active photocatalysts for practical applications.

Zinc oxide (ZnO), tungsten oxide (WO₃), and zirconium oxide (ZrO₂), strontium-titanium oxide (SrTiO₃) nanoparticles (NPs) are significant semiconductor material and of great interest due to their high stability, harmlessness, excellent optical and electrical properties, and high oxidizing potential (Autefage et al. 2019; Ebrahimi et al. 2019; Ghasempour et al. 2015; Gouda 2012; Yan et al. 2013). Especially, ZnO NPs are used in various products such as sunscreens, toothpaste, beauty products, rubber, and medicine (Hou et al. 2018). Doping of metal oxides with 4d transition metals, such as molybdenum, is a proven method to improve the practical applications of metal oxide. A remarkable increase in photoelectrochemical (PEC) performance of WO₃ NPs and in the bioactivity of hydroxyapatite was observed upon doping with molybdenum (Abutalib and Yahia 2017; Kalanur and Seo 2018). The improved photocatalytic activity of ZnO was observed with an increased percentage of the molybdenum dopant (Reddy, Reddy, and Reddy 2011). Thus, the molybdenum dopant can play

an important role in the increasing photocatalytic performance of metal oxides under visible light.

There are several methods for the preparation of doped photocatalysts, such as the sol-gel (Khaki et al. 2017), hydrothermal (Khaki et al. 2017), co-precipitation (Nasir et al. 2017), and flame spray pyrolysis (Boningari et al. 2018) methods, all of which require multiple steps and precise reaction conditions. These days, the preparation of doped photocatalyst using the easy, rapid, and more environmentally friendly ball-milling method has been increasing in popularity (Lonkar, Pillai, and Abdala 2019). The ball mill instruments are cheaper and easy to handle. Notably, they have the capability to synthesize size-controlled nanoparticles with a simple operating procedure (Ahadi, Moalej, and Sheibani 2019). The mechanical energy of ball mills can develop dislocations and vacancies in crystals, alter particle sizes, increase specific surface area of particles, and change the photocatalyst framework, thus increasing reactive edge sites (Shafei, Salarpour, and Sheibani 2019). Further, solvent-free synthesis of desired doped photocatalyst increases the usability of the ball-milling method.

Recently, photocatalysts have been applied for the control of harmful algal bloom extensively (Aruoja et al. 2009; Du et al. 2019; Oukarroum, Halimi, and Siaj 2019). ZnO NPs have been critically investigated for anti-algal (Halbus, Horozov, and Paunov 2020) and antimicrobial activity (Silva et al. 2019), compared to WO₃ and ZrO₂ NPs. Photocatalysts generate reactive oxygen species such as hydroxyl free radicals ($\cdot\text{OH}$) in the presence of light (Ding et al. 2016). The produced $\cdot\text{OH}$ has high oxidizing power and can oxidize cellular lipid into lipid peroxide, destroy cell morphology, and ultimately exterminate the species (Li et al. 2015). Several studies have indicated that photocatalysts can cause oxidative stress in algal cells by increasing the intracellular ROS level, which can damage DNA, RNA, proteins, and lipids, resulting in cell death (Brynildsen et al. 2013; Kalanur and Seo 2018; Suman, Radhika Rajasree, and Kirubakaran 2015). Additionally, the release of

metal ion (Aruoja et al. 2009; Du et al. 2019; Oukarroum et al. 2019) and aggregation of the photocatalyst (Joonas et al. 2019; Sousa, Soares, and Soares 2019) in the medium can affect the growth of algae.

In the present study, we attempted to synthesize molybdenum-doped zinc oxide (MoZnO), molybdenum-doped zirconium oxide (MoZrO), molybdenum-doped tungsten oxide (MoWO), and molybdenum-doped strontium titanium oxide (MoSrTiO) using the ball-milling method. The biological activity of the synthesized molybdenum-doped metal oxides against bloom-forming *Microcystis aeruginosa* was examined under the visible light. Based on the results of FT-IR analysis and preliminary anti-algal activity, MoZnO was subjected to further characterizations by FESEM, EDX, XRD, and FT-IR spectroscopy. Furthermore, the mechanisms of action of MoZnO were investigated in terms of the production of extracellular hydroxyl radical and intracellular ROS, lipid peroxidation, the effect of metal oxides and their combinations on the inhibition of algal growth.

4.3 Results

4.3.1 Synthesis, morphological and microstructural analysis of MoZnO

MoZnO was successfully synthesized by ball milling of ZnO and $(\text{MoCl}_5)_2$ powder. Change in the color of white ZnO to brown indicated the synthesis of MoZnO. The product yield of MoZnO was 65%. However, no color change was observed during the synthesis of MoZrO, MoWO, and MoSrTiO, and the yield of MoZrO, MoWO, and MoSrTiO was 20%, 34%, and 33%, respectively.

Shape and particle-size distribution of ZnO and MoZnO were analyzed using FESEM (Figure 4.1). The FESEM image shows that ZnO particles were mostly rod-shaped with some irregularity (Figure 4.1A), while MoZnO particles were largely arranged into an irregular morphology (Figure 4.1B). The majority of the ZnO particles had a size of up to 300-500 nm (Figure 4.1C). The average particle size of ZnO was 392 nm, and the particle size decreased upon doping ZnO with Mo (Figure 4.1D). Most particles had a size of 23-45 nm. The average particle size of MoZnO was 40 nm. It was found that particle shape and size were strongly altered by ball milling and doping. The average particle size decreased 9.8-fold with ball milling and Mo doping. The decrease in particle size increased the surface area, energy, and reactivity of particles.

Atomic% in MoZnO was analyzed using EDX. EDX spectrum analysis was performed to determine the composition of elements present in MoZnO. The EDX spectrum of MoZnO showed the presence of Zn, Mo, O, and Cl elements (Figure 4.2). The linkage of $(\text{MoCl}_5)_2$ to ZnO was confirmed by the coexistence of Mo and Cl on the surface of MoZnO. The weight% and atomic% of the elements present in MoZnO are shown in Table 4.1. The atomic% of Zn, Mo, O, and Cl elements are 28.25, 3.23, 61.66, and 6.87, respectively.

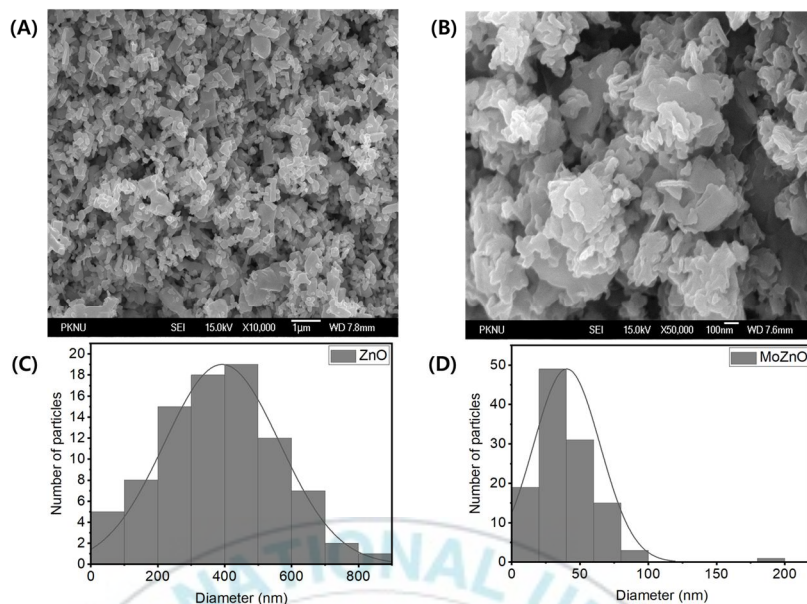


Figure 4.1. FESEM image of (A) ZnO, and (B) MoZnO, particle size distribution of (C) ZnO, and (D) MoZnO.

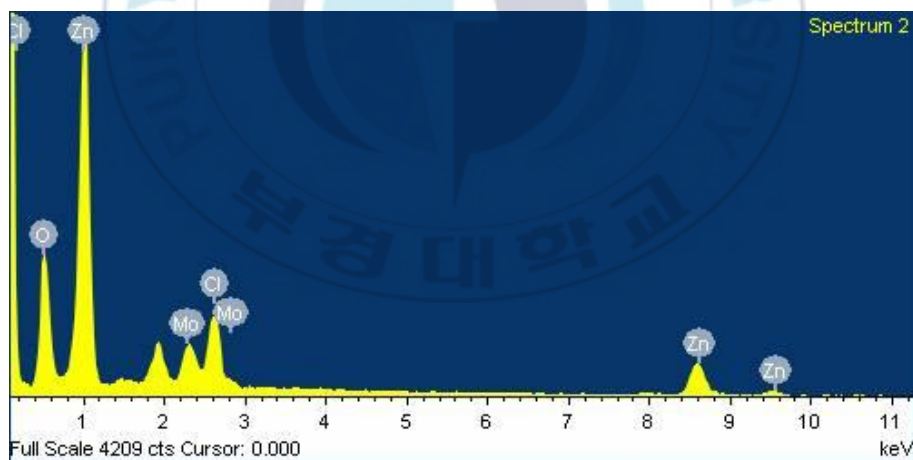


Figure 4.2. EDX spectrum of MoZnO. EDX spectrum displayed the atomic composition of MoZnO. EDX spectrum of MoZnO showed the presence of Zn, Mo, O, and Cl elements.

Table 4.1. Element proportion analysis of MoZnO.

Element	Weight%	Atomic%
O	29.1	61.6
Cl	7.1	6.8
Zn	54.5	28.2
Mo	9.1	3.2

4.3.2 Structural analysis of MoZnO

The doping of Mo into ZnO strongly affected the peak intensity and showed the coexistence of two phases in the XRD pattern (Figure 4.3). The weak diffraction peaks related to (100), (002), (101), (102), (110), (103), (200), (112), (201), (004), and (202) reflections in MoZnO showed the existence of the wurtzite phase of ZnO, whereas (021), (111), (150), and (180) reflections indicated the presence of orthorhombic MoO₃. The XRD peak for (MoCl₅)₂ was appeared at ~17° (Kim et al. 2019). A decrease in the crystallite size of ZnO was observed upon doping with Mo. The calculated crystallite size of ZnO and MoZnO was 45.461 nm and 4.481 nm (Table 4.2), respectively. The calculated crystallite size decreased 10 times upon ball milling and doping with Mo. These results matched well with FESEM and EDX data. MoZnO showed a small alteration in the position of the diffraction peaks towards slightly higher angles, similar to the standard ZnO crystal, indicating that molybdenum substitutes for zinc in the hexagonal lattice (Shatnawi et al. 2016; Xiu et al. 2007).

The calculated values of $TC(hkl)$ for seven main peaks are shown in Table 4.3. Both ZnO and MoZnO had $TC(hkl)$ values somewhat different from one. This indicates that both ZnO and MoZnO had preferential orientation along all planes. This was supported by the values of c/a shown in Table 4.2. The obtained c/a values for ZnO and MoZnO were just as reported standard c/a values for the wurtzite structure, which was about 1.63 (Rusu, Rusu, and Luca 2011). Therefore, it was expected that crystallites were oriented along all planes.

A sharp decline in peak intensity of ZnO was observed upon doping with Mo. This could arise from the different ionic radii of zinc and molybdenum, which led to lattice disorder and strain that occurred in the ZnO crystal after the Zn exchanged with Mo at the Zn lattice sites (Swapna and Santhosh Kumar 2013).

Table 4.2 shows the measured values of the lattice constant. The values of both *a* and *c* were slightly larger compared to bulk ZnO values (0.3242 nm and 0.5194 nm, respectively, for *a* and *c*, JCPDS-75–0576) (Swapna and Santhosh Kumar 2013). The calculated values of the lattice strain are shown in Table 4.2. The lattice strain value of ZnO increased from 0.130 to 4.560 upon doping with Mo, which may be related to the nucleation process of ZnO. High Mo concentration enhanced the number of nucleations of ZnO, resulting in limited grain size and greater lattice strain (Boukhachem et al. 2012).

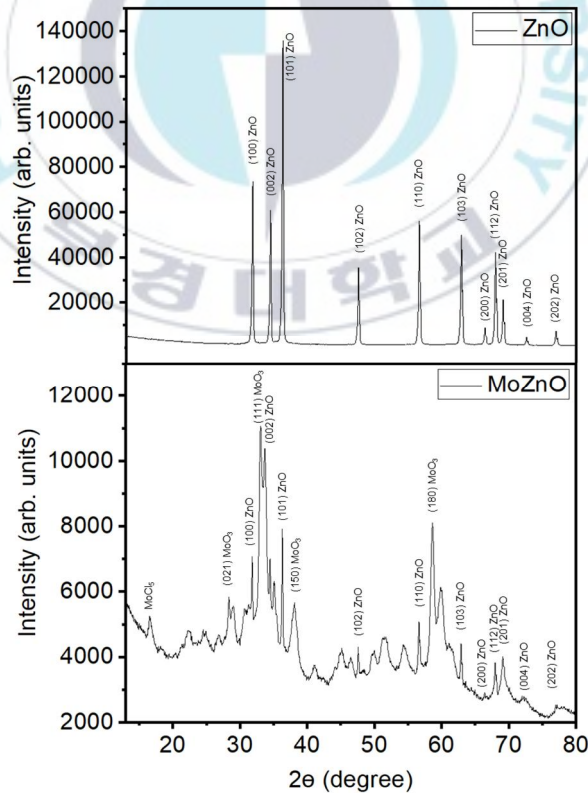


Figure 4.3. X-ray diffraction patterns of the (A) ZnO and (B) MoZnO.

Table 4.2. Calculated crystallite size, lattice constants, and microstrain values of ZnO and MoZnO.

Material	Dopant atomic%	Crystallite size (nm)	Lattice constant (Å)		c/a	Lattice strain (ϵ)
			c	a		
ZnO	0	45 ± 3.5	5.2 ± 0.01	3.2 ± 0.002	1.6	0.10 ± 0.03
MoZnO	3.2	4.4 ± 0.61	5.2 ± 0.02	3.2 ± 0.002	1.6	4.5 ± 0.5

Table 4.3. Calculated texture coefficients of MoZnO for the seven main peaks.

Material	Dopant%	TC(hkl)						
		(100)	(002)	(101)	(102)	(110)	(103)	(112)
ZnO	0	0.91	0.97	0.95	1.07	1.23	1.21	0.65
MoZnO	3.23	0.85	1.07	0.55	1.28	1.08	1.03	1.13

ZnO, ZrO₂, WO₃, and SrTiO₃ were characterized by FT-IR spectroscopy (Figure 4.4). The FT-IR spectrum of ZnO shows a stretched band of zinc and oxygen at 439 cm⁻¹ (Azizi et al. 2014). The FT-IR spectrum of Na₂MoO₄·2H₂O shows broad bands in the regions of 3000–3600 cm⁻¹, which indicates the presence of hydroxyl groups bonded to the metal at the surface (Nakagaki et al. 2008). Notably, the characteristic bands of Mo-O in Na₂MoO₄·2H₂O appeared at 833 cm⁻¹. The FT-IR spectrum of MoZnO shows the characteristic bands for ZnO and Mo-O at 467 cm⁻¹ and 867 cm⁻¹, respectively. The FT-IR spectrum of MoZnO shows a new band corresponding to Zn-O-Mo linkage at 1038 cm⁻¹ (indicated with an arrow), which was not present in the spectra of ZnO or Na₂MoO₄·2H₂O (Yu et al. 2012). Bands at 867 cm⁻¹, 906 cm⁻¹, 1618 cm⁻¹, 3454 cm⁻¹, and 3501 cm⁻¹ indicate the presence of MoO₃ in MoZnO (Yu et al. 2012). FT-IR spectra matched well with the XRD results, suggesting the existence of MoO₃ on the surface of the catalyst. The FT-IR spectrum of MoZrO, MoWO, and MoSrTiO showed the presence of respective metal oxide peaks i.e. 721 cm⁻¹ (Zr-O) (Afanasiev, Geantet, and Kerridge 1995), 1174 cm⁻¹ (W-O) (Kim et al. 2019), 563 cm⁻¹ (Ti-O) (Craciun and Singh 2000). The FT-IR spectrum of MoSrTiO did not show the peak of Sr-O. The FT-IR spectrum of MoZrO, MoWO, and MoSrTiO (Figure S3) shows a new band at

983 cm^{-1} , 953 cm^{-1} , and 954 cm^{-1} (indicated with an arrow), which may correspond to Zr–O–Mo (Afanasiev et al. 1995), W–O–Mo (Kim et al. 2019), and SrTi–O–Mo linkages, respectively.

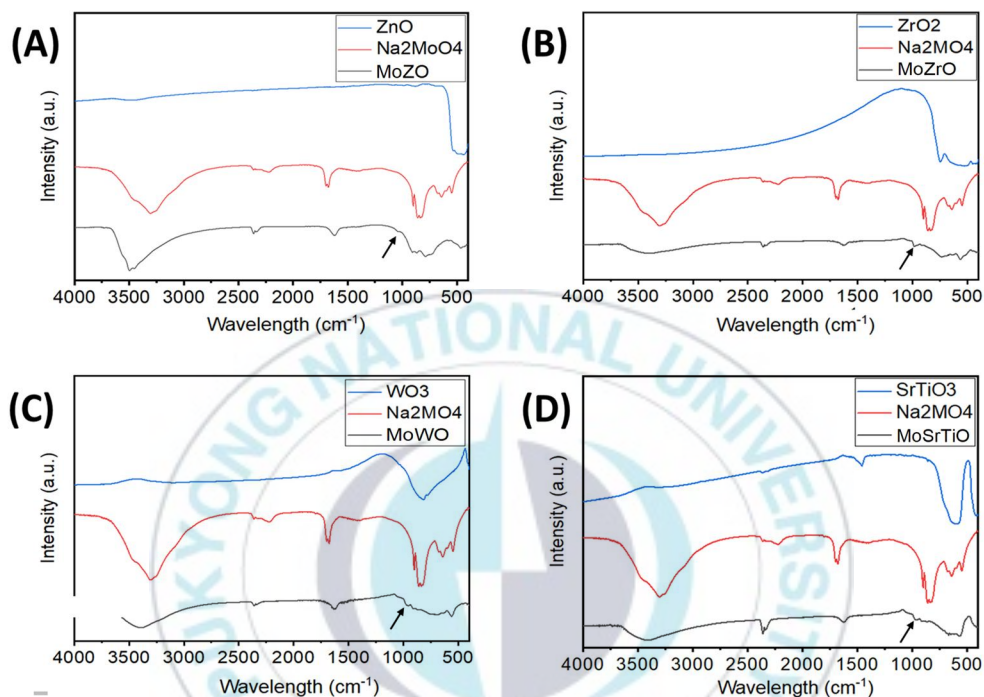


Figure 4.4. FT-IR spectra of A) ZnO, $\text{Na}_2\text{MoO}_4 \cdot 2\text{H}_2\text{O}$, and MoZnO, B) ZrO_2 , $\text{Na}_2\text{MoO}_4 \cdot 2\text{H}_2\text{O}$, and MoZrO, C) WO_3 , $\text{Na}_2\text{MoO}_4 \cdot 2\text{H}_2\text{O}$, and MoWO, D) ZrSrTiO_3 , $\text{Na}_2\text{MoO}_4 \cdot 2\text{H}_2\text{O}$, and MoSrTiO.

4.3.3 Anti-algal Assay

A preliminary study revealed that only MoZnO inhibited the growth of *M. aeruginosa* cells as function of concentration while others did not (Figure 4.5). MoZnO showed a linear relationship between the initial rate of reaction and the concentration of photocatalyst, which was one of the characteristics of an ideal photocatalyst (Figure 4.6). Based on the obtained results, MoZnO was used for further study. A change in the pigment of *M. aeruginosa* suspension was observed

after incubating with various concentrations of MoZnO (Figure 4.7A), and this change was dependent on the concentration of MoZnO. The *M. aeruginosa* cultures with 5 mg/L and 10 mg/L of MoZnO exhibited a change within 2 h of incubation, whereas those with 1 mg/L and 2.5 mg/L of MoZnO exhibited a change in pigment within 3-4 h of incubation.

OD680 value of *M. aeruginosa* was decreased in a concentration-dependent manner (Figure 4.7B). Incubating algal cells with 1 mg/L MoZnO caused an increase of OD680 value initially, but this value then slowly decreased over the incubation time. The exposure of *M. aeruginosa* to 2.5, 5, and 10 mg/L MoZnO brought about the monotonic decrease of OD680 with time. We also examined the anti-algal activity of metal salts, metal oxides, and their combinations against *M. aeruginosa* to rule out their contribution to the anti-algal activity of synthesized photocatalysts (Figure 4.8). As speculated, they did not show any anti-algal activity.

MoZnO showed a concentration-dependent inhibition rate of *M. aeruginosa* (Figure 4.7C). The initial inhibition rate was low for 1, 2.5, and 5 mg/L of MoZnO, whereas a high inhibition rate was observed for 10 mg/L of MoZnO. The inhibition rate of the incubated suspension of *M. aeruginosa* with 1 mg/L of MoZnO decreased for up to 2 h and then increased with time. The inhibition rate of 1 mg/L MoZnO increased gradually with time, whereas the inhibition rate of 2.5, 5, and 10 mg/L MoZnO stabilized at specific times. The final percent inhibition rate of 1 mg/L MoZnO was about 318%. The stabilized percent inhibition rate of 2.5, 5, and 10 mg/L MoZnO was about 375 to 385%, which may be due to the extensive death of *M. aeruginosa* cells. Overall, the suppression of *M. aeruginosa* growth due to the presence of MoZnO was justified in this work, and the minimum inhibitory concentration (MIC) was found to be 1.0 mg/L.

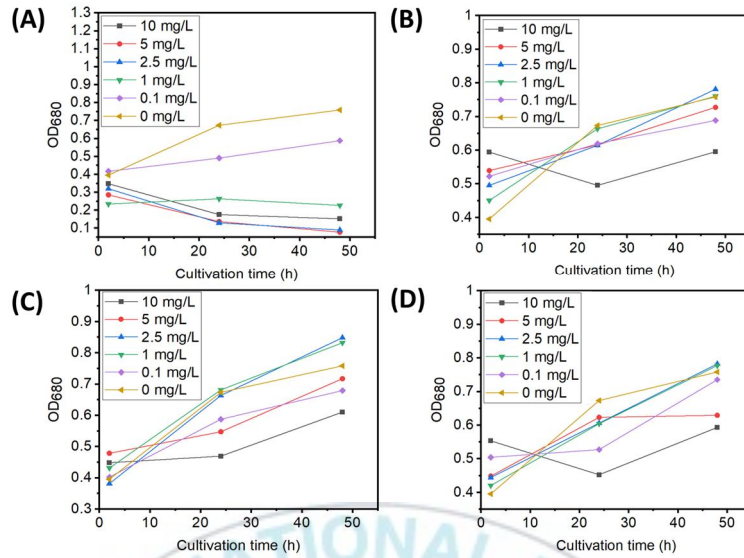


Figure 4. 5. Preliminary anti-algal activity of molybdenum-doped metal oxides at 2 h, 24 h, and 48 h (A) MoZnO, (B) MoZrO₂, (C) MoWO₃, and (D) MoSrTiO₃.

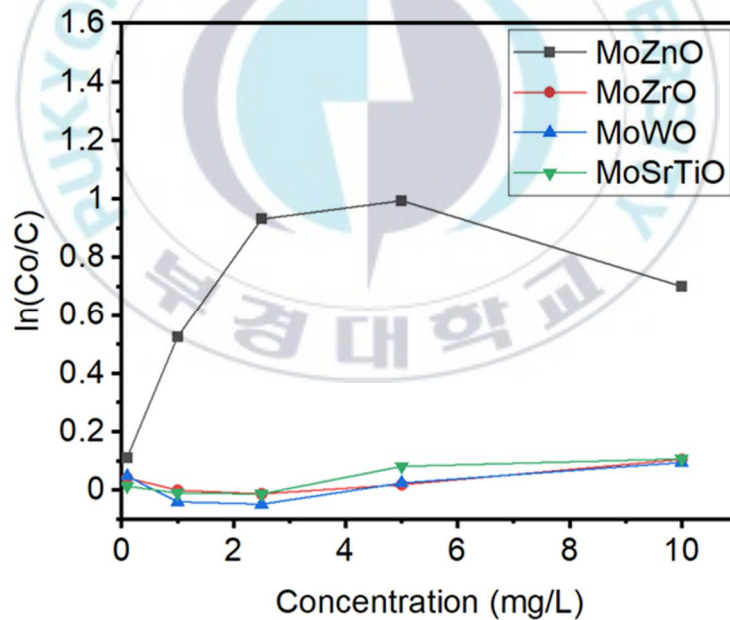


Figure 4. 6. Plot of pseudo first order rate versus concentration of molybdenum-doped metal oxides (obtained from preliminary anti-algal activity).

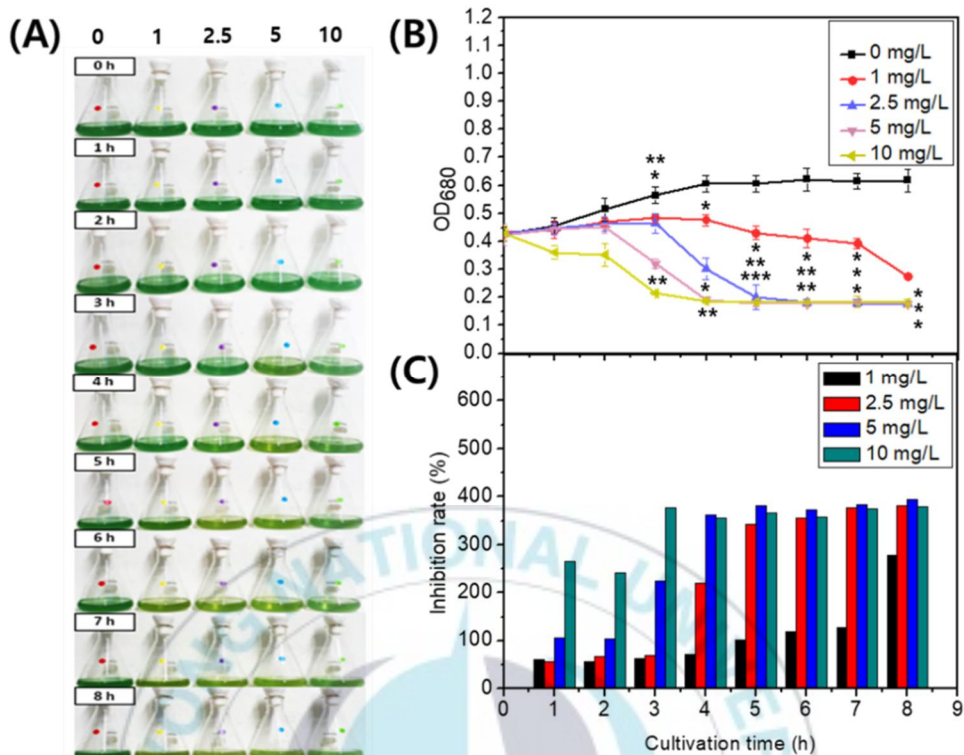


Figure 4.7. Growth inhibition of *M. aeruginosa* by MoZnO with time. (A) Change in pigment of *M. aeruginosa* suspension. (B) Change in OD₆₈₀ of *M. aeruginosa*, and (C) Inhibition rate (%) of *M. aeruginosa*. Statistical significance (determined by paired t-test) is shown by * = $p < 0.05$, ** = $p < 0.001$, *** = $p < 0.0001$, when compared to control (0).

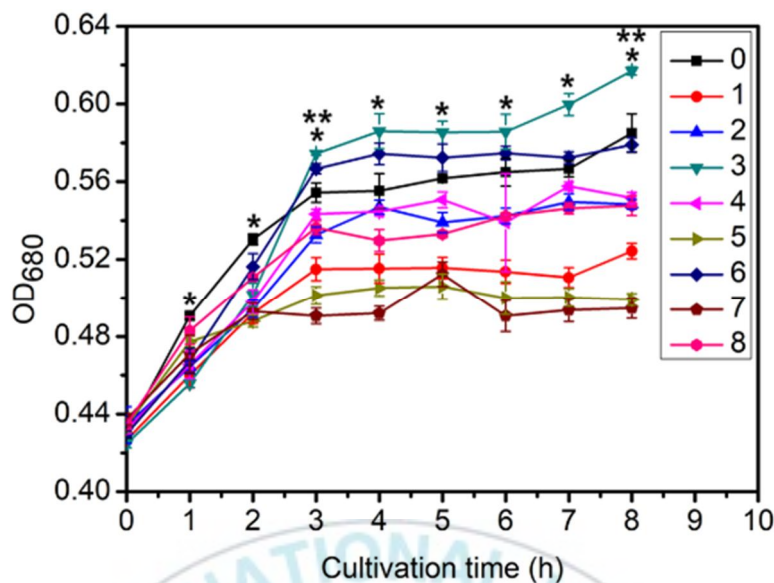
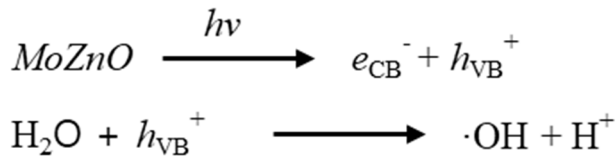


Figure 4. 8. Effect of ZnSO_4 (1), $(\text{MoCl}_5)_2$ (2), ZnO (3), $\text{Na}_2\text{MoO}_4 \cdot 2\text{H}_2\text{O}$ (4), and their combinations $\text{ZnSO}_4 + \text{Na}_2\text{MoO}_4 \cdot 2\text{H}_2\text{O}$ (5), $\text{ZnO} + \text{Na}_2\text{MoO}_4 \cdot 2\text{H}_2\text{O}$ (6), $\text{ZnSO}_4 + (\text{MoCl}_5)_2$ (7), and $\text{ZnO} + (\text{MoCl}_5)_2$ (8) on the growth of *M. aeruginosa*. Statistical significance (determined by paired t-test) is shown by $* = p < 0.05$, $** = p < 0.001$, when compared to control (0).

4.3.4 Mechanisms of Algae Growth Inhibition

Generation of extracellular $\cdot\text{OH}$ by MoZnO in BGM, under direct illumination with visible light (C, EX) and under the shading of *M. aeruginosa* medium (SC, SEX), was investigated using $\cdot\text{OH}$ (Figure 4.9). The fluorescence intensity of the control groups (C, SC) was lower than that of the experimental groups (EX, SEX). Isopropanol scavenged the $\cdot\text{OH}$ formed by nanomaterials, thus decreasing the $\cdot\text{OH}$ fluorescence intensity of the control group (Phongarthit, Amornpitoksuk, and Suwanboon 2019). The shading of *M. aeruginosa* had a sizable impact on the $\cdot\text{OH}$ production efficiency of MoZnO (Figure 4.10). Upon shading, the fluorescence intensity of both control and experimental groups decreased by 1.2 and 2.7-fold, respectively.

The plausible steps for the generation of $\cdot\text{OH}$ free radical by MoZnO are given as follows:



The irradiation of MoZnO with visible light caused the generation of a negatively charged conduction band (e_{CB}^-) and positively charged valence band (h_{VB}^+) (Quek et al. 2018). The h_{VB}^+ extracted electrons from nearby water molecules, producing hydroxyl radicals and protons. The high oxidation potential of the generated $\cdot\text{OH}$ can damage harmful cyanobacteria.

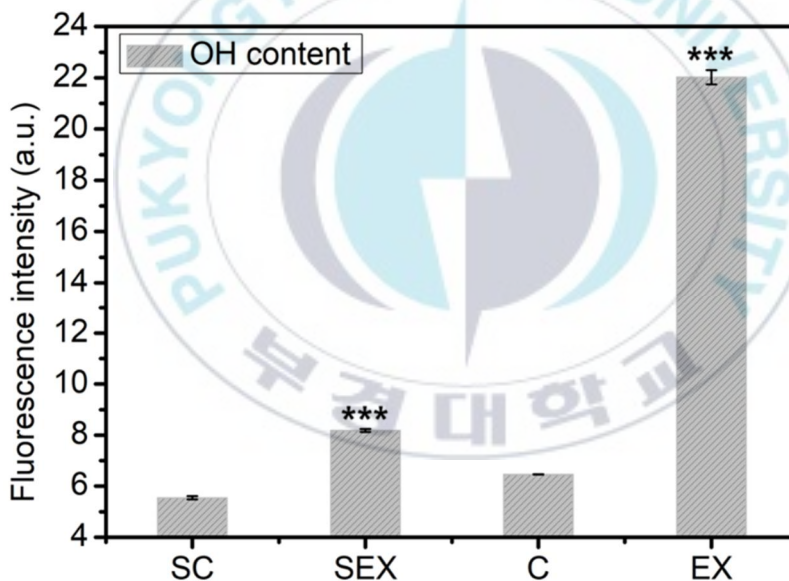


Figure 4.9. Fluorescence intensity of extracellular $\cdot\text{OH}$ generated at 4 h. C and SC are control groups under open air and shading of *M. aeruginosa*, and EX and SEX experimental groups under open air and shading of *M. aeruginosa*. Statistical significance (determined by paired t-test) is shown by *** = $p < 0.0001$, when compared to control (0).

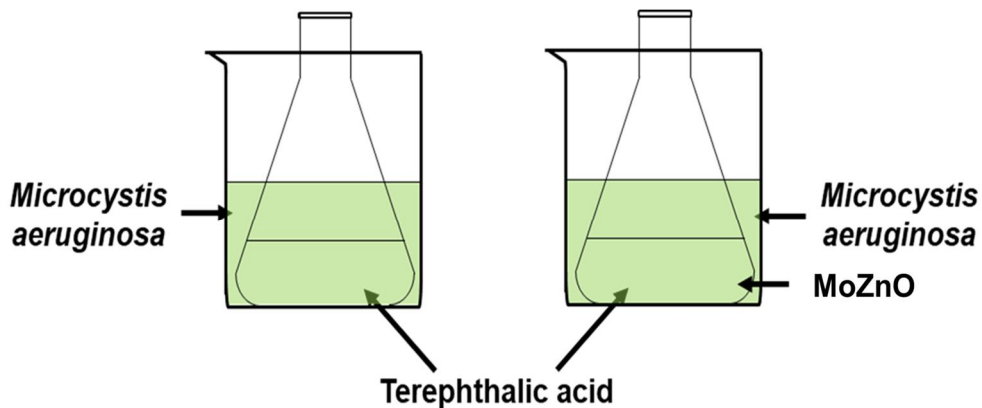


Figure 4.10. $\cdot\text{OH}$ assay under the shading of *M. aeruginosa*. TA (0.5 mM; 100 mL) was poured in two 250 mL conical flasks. After setting the conical flasks in two 500 mL beaker respectively, the beaker was filled with *M. aeruginosa* culture. One was labeled as an experimental group (SEX) and another one as the control group (SC).

Intracellular ROS induced by various concentrations of MoZnO in the *M. aeruginosa* cells was measured up to 4 h (Figure 4.11). *M. aeruginosa* cells showed concentration-dependent intracellular ROS production. For *M. aeruginosa* cells treated with 1 mg/L of MoZnO, the ROS level fluctuated at every 1 h interval. For the *M. aeruginosa* cells treated with 2.5, 5, and 10 mg/L, ROS content was substantially greater than in cells without MoZnO. The ROS content decreased after 2 h. It was determined that a higher concentration of MoZnO caused enormous algal cell death. Detection of ROS was not possible in dead cells.

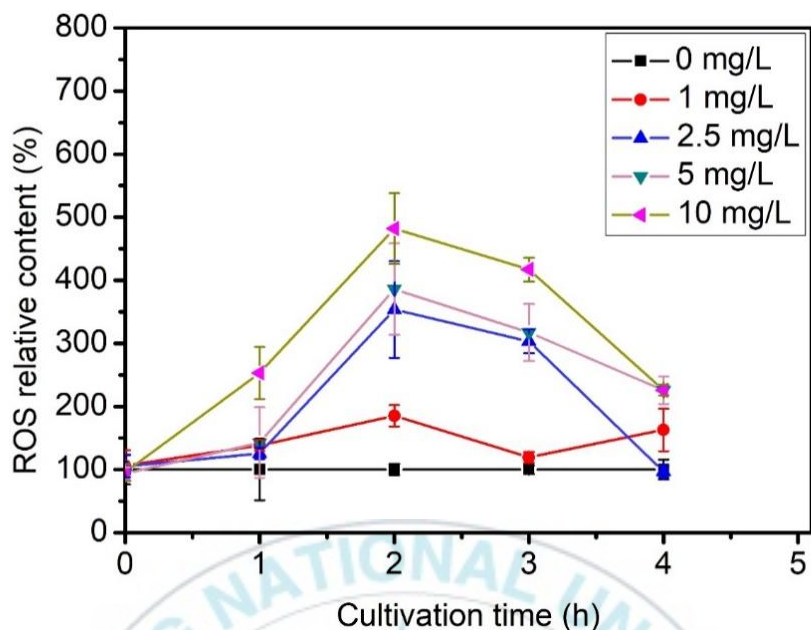


Figure 4.11. Intracellular ROS induced by MoZnO in the *M. aeruginosa* cells.

The membrane integrity was evaluated using lipid peroxidation assay. The MDA content in the treated cells was increased 1.8 to 2-fold more than in the control group, which indicates that the lipid was more exposed to the $\cdot\text{OH}$ in the treated groups (Figure 4.12). The optical microscope and SEM images of *M. aeruginosa* treated with MoZnO showed a concentration-dependent agglomeration in algal cells (Figure 4.13 and 4.14). The control group did not show any agglomeration. In SEM analysis, organic matter on the surface of algal cells was pointed by an arrow.

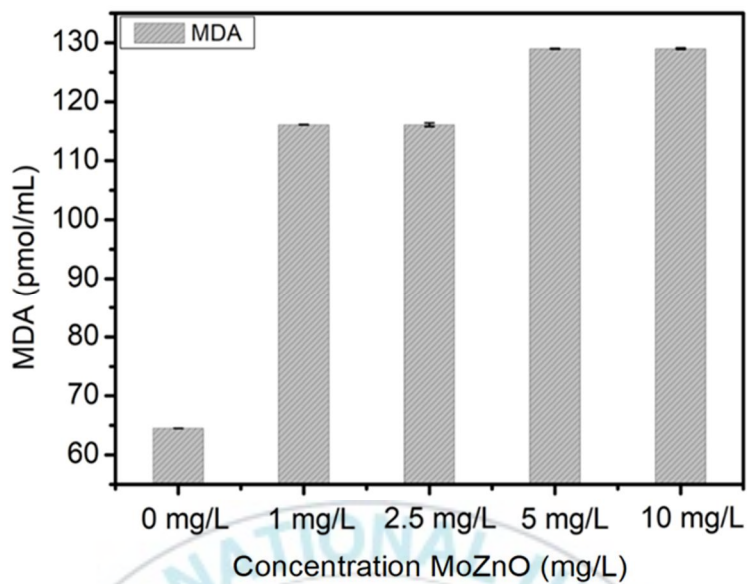


Figure 4. 12. Lipid peroxidation of *M. aeruginosa* cells at 4 h.

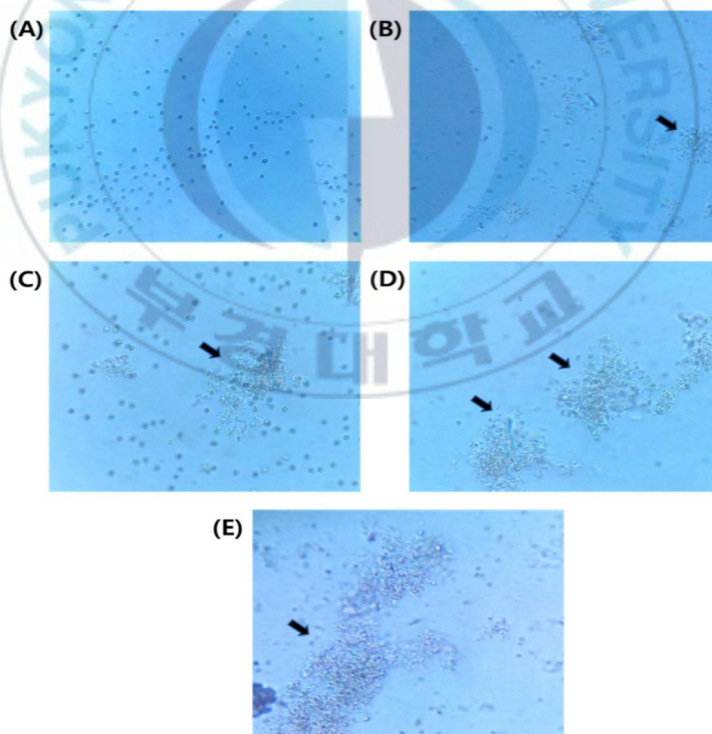


Figure 4. 13. Optical microscope images of *M. aeruginosa* cells after incubation with MoZnO up to 4 h: (A) 0 mg/L; (B) 1 mg/L; (C) 2.5 mg/L; (D) 5 mg/L; (E) 10 mg/L.

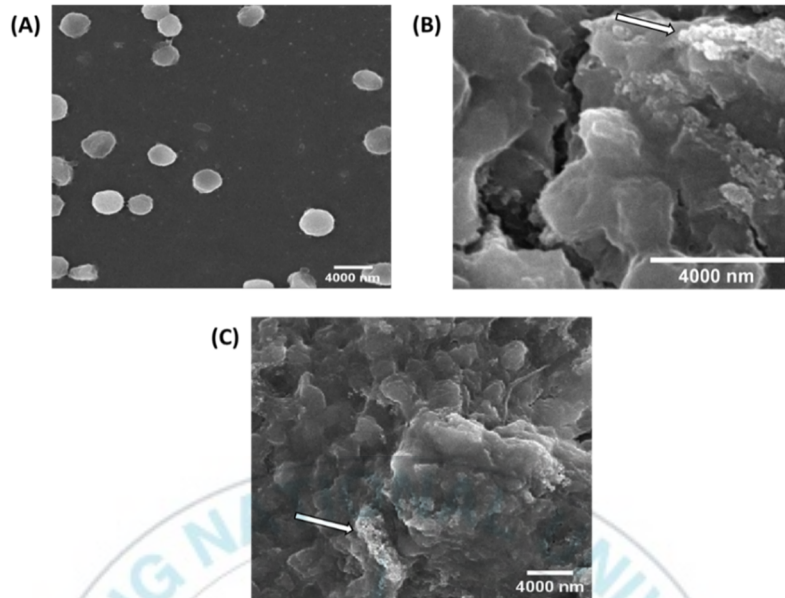


Figure 4.14. SEM images of *M. aeruginosa* cells after incubation with MoZnO up to 4 h: (A) 0 mg/L; (B) 5 mg/L; (C) 10 mg/L.

4.4 Discussion

In the present study, we synthesized molybdenum-doped metal oxides (MoZnO, MoZrO, MoWO, and MoSrTiO) using the solvent-free ball-milling method. The decrease in the crystallite size of ZnO was observed upon doping with Mo. Swapna et al. (Swapna and Santhosh Kumar 2013) obtained similar results for Mo-doped ZnO thin films synthesized by spray pyrolysis method. This indicates that the degradation of the crystallinity of MoZnO is a result of doping with high Mo concentration. The lower product yield of MoZrO, MoWO, and MoSrTiO indicate that the solvent-free ball milling may not be a suitable method for the synthesis of these photocatalysts. The molar ratio of metal oxides was lower in MoZrO, MoWO, and MoSrTiO, but was higher in MoZnO, which could be the plausible reason for the low yield of MoZrO, MoWO, and MoSrTiO. The higher molar ratio of ZnO may increase the chances of the interaction of ZnO with $(\text{MoCl}_5)_2$ and result in higher product yield and doping of Mo. In this context, precipitation (Xie et al. 2000), RF magnetron sputtering (Madhavi et al. 2014), and hydrothermal (Nosaka et al. 2012; Yin et al. 2017) methods could be more efficient than solvent-free ball mill method for the synthesis of MoZrO, MoWO, and MoSrTiO.

Fan et al. (Fan, Bao, et al. 2019) used 1 mg/L Cu-MOF-74 and Yu et al. (Yu et al. 2010) used AgBiO_3 , AgNO_3 , and NaNO_3 to inhibit the growth of *M. aeruginosa*. They noticed that the growth of algal cells was inhibited after 24 and 96 h, respectively. The synthesized MoZnO showed rapid growth inhibition of *M. aeruginosa* at a minimum concentration of 2.5 mg/L after 4 h. ZrO_2 , WO_3 , and SrTiO_3 did not show growth inhibition of *M. aeruginosa* (Figure S1). Ideal photocatalysts have a linear relationship between the initial rate of reaction and the concentration of photocatalyst (Hoque and Guzman 2018). Initially, the concentration of photocatalyst is directly proportional to an absorbed photon flux. After achieving the maximum rate, the rate of reaction may remain constant, or in some cases, it may decrease with an increase in the concentration of photocatalyst.

The decrease in rate may be due to the increased scattering of the visible light. Out of the MoZnO, MoZrO, MoWO, and MoSrTiO, only MoZnO had a linear relationship between the initial rate of reaction and the concentration of photocatalyst (Figure S2). The rate of reaction of MoZnO was decreased at higher concentrations, which may be due to the increased scattering of the incident light. It was observed that doping of the low percentage of Mo in WO₃ increased the bandgap of the resulting product (Alan May et al. 2007). An increase in the bandgap decreased the reactivity of metal oxides, which may be the possible reason for the inactivity of MoWO. Chary et al. (Chary et al. 2004) found that the catalytic activity of MoO₃/ZrO₂ increased with the increase in Mo dopant. Nosaka et al. (Nosaka et al. 2012) found that Mo doping in SrTiO₃ increased the recombination of generated electron and hole under visible light. A low percentage of Mo in MoZrO and electron-hole pair recombination in MoSrTiO could be a possible reason for their inactivity. Du et al. (Du et al. 2019) noticed that 0.71 mg/L Zn²⁺ ion and 1 mg/L ZnO NP promote the growth of *M. aeruginosa*. Similar results are obtained after incubating *M. aeruginosa* with 2.5 mg/L ZnO and ZnO+Na₂MoO₄·2H₂O for 8 h. However, Zn²⁺ ion from 2.5 mg/L ZnSO₄ treatment does not have any significant effect on *M. aeruginosa* growth. We performed the ·OH and ROS assay to confirm the generation of extracellular ·OH and intracellular ROS in *M. aeruginosa*. MoZnO generates extracellular ·OH, which has high oxidation potential. Ding et al. (Ding et al. 2016) found that nano-ZnS-montmorillonite caused concentration-dependent production of ·OH radicals. Additionally, we found that *M. aeruginosa* has a shading effect on ·OH production efficiency of MoZnO, decreasing the actual efficiency of MoZnO. Though the shading of *M. aeruginosa* cells decreased the efficiency of ·OH production, ·OH-mediated growth inhibition of algal cells is considered an important mechanism of inhibition by MoZnO (Quek et al. 2018). MoZnO shows the concentration-dependent generation of intracellular ROS, which increases for up to 2 h and then decreases. The reason may be that MoZnO at higher concentrations causes widespread death of algal cells. ROS detection is impossible

in dead cells. Concentrations higher than 1 mg/L MoZnO increased the ROS content and the internal oxidative stress in *M. aeruginosa* cells, suggesting that MoZnO causes oxidative damage to algal cells. He et al. (He et al. 2019) obtained similar results, in which nano-ThO₂ demonstrated the concentration-dependent generation of intracellular ROS in *Chlorella pyrenoidosa* after 48 h. Intracellular ROS and extracellular ·OH produced by the presence of MoZnO can cause lipid peroxidation in *M. aeruginosa*. Vicente et al. found that ZnO at 1, 5, and 10 mg/L causes peroxidation of model cyanobacteria *Synechococcus elongates* (Anne Vicente, Bénédicte Sohm, Justine Flayac, Philippe Rousselle, Pascale Baudal 2019). MoZnO increases the MDA content in the *M. aeruginosa* suspension at 1, 2.5, 5, and 10 mg/L, indicating that MoZnO causes peroxidation of lipids in algal cells. Peroxidation of algal cells may be the cause of oxidative stress generated by MoZnO-mediated ROS. Fan et al. (Fan, Bao, et al. 2019) and Zhou et al. (Zhou et al. 2014) found that the treatment of *M. aeruginosa* with Cu-MOF-74 and potassium ferrate (VI) induced the aggregation of the algal cell with the release of internal organic matter. MoZnO induced the agglomeration of *M. aeruginosa* in a concentration-dependent manner. SEM image showed the release of organic matter by *M. aeruginosa* incubated with MoZnO. MoZnO generated ·OH radical in the BG-11 medium, which oxidized the lipid membrane of algal cells, resulting in cell damage. The discharge of organic matter from damage cells in BGM diminishes the stability of the algal suspension, facilitating agglomeration. Therefore, agglomeration can be considered an anti-algal mechanism of MoZnO.

4.5. Materials and Methods

4.5.1 Preparation of MoZnO

Molybdenum-doped zinc oxide (MoZnO) photocatalyst was synthesized in the liquid-free medium in a vacuum planetary ball mill (QM-1F, Nanjing University Instrument Plant, Nanjing, China). 1000 mg of ZnO powder was mixed with agate ball in a 1:10 ratio in the agate ball milling tank, and then a 500 mg of $(\text{MoCl}_5)_2$ was added. $(\text{MoCl}_5)_2$ is a highly unstable metal chloride which can react efficiently with stable metal oxides to produce the molybdenum-doped metal oxide (Kim et al. 2019). The mixture was milled for 2 h with the milling rate of 300 rpm. The resulting powder was rinsed four times with deionized water and three times absolute ethanol and then kept at 353 K up to 6 h in an oven. In addition, we used zirconium oxide (ZrO_2), tungsten oxide (WO_3), and strontium titanate (SrTiO_3) to synthesize respective molybdenum-doped metal oxides (MoZrO, MoWO, and MoSrTiO) using same reaction conditions. The molar ratio of ZnO, ZrO_2 , WO_3 , and SrTiO_3 to $(\text{MoCl}_5)_2$ were 6.8, 4.5, 2.4, and 3.2, respectively.

4.5.2 Characterization

4.5.2.1 Morphological and microstructural analysis

The shape and size of MoZnO were analyzed using field emission scanning electron microscopy (FESEM). FESEM was performed at an accelerating voltage of 0.5~30 KV (JSM-6700F, JEOL, Tokyo, Japan). The elemental proportion of MoZnO was analyzed using an energy dispersive X-ray spectrometer (EDX, INCAx-sight, Oxford).

4.5.2.2 Structural analysis

4.5.2.2.1 XRD analysis

The crystallinity of MoZnO was analyzed using an X-ray diffractometer (Rigaku

Ultima IV, Rigaku, Japan), with Cu K α radiation (wavelength = 15.4 nm) operated at 40 kV and 40 mA. The crystallite size D of ZnO and MoZnO was calculated using the Scherrer equation (Mitran et al. 2019):

$$D = \frac{k\lambda}{\beta \cos \theta}$$

where D is the crystalline size; k is the shape factor (0.9); λ is the wavelength of X-ray (1.54056 Å); β is the Full Width at Half Maximum (FWHM) of the diffraction peak (in radians); θ is the diffraction angle of the reflection.

Texture coefficients (TC) were calculated to understand the orientation of doped Mo in MoZnO using the 36–1451 JCPDS-ICDD card for all the peaks except (200) peak (Znaidi et al. 2013). The equation of texture coefficient is as follows (Znaidi et al. 2013):

$$TC(hkl) = \frac{I(hkl)/I_0(hkl)}{(1/N)\sum_{h'k'l'} [I(h'k'l')/I_0(h'k'l')]}$$

where $I(hkl)$ is the measured relative intensity of (hkl) plane, $I_0(hkl)$ is the theoretical intensity of the same plane taken from the 36–1451 JCPDS-ICDD card, and N is the number of reflections. The random orientation of doped material has $TC(hkl)$ value equal to 1, whereas value other than 1 indicates the preferred orientation.

The lattice constants a and c were measured by applying the following equation (Swapna and Santhosh Kumar 2013):

$$\frac{1}{d^2} = \frac{4}{3} \left(\frac{h^2 + hk + k^2}{a^2} \right) + \frac{l^2}{c^2}$$

The lattice strain (ϵ) was measured using the tangent formula (Boukhachem et al. 2012):

$$\varepsilon = \frac{\beta}{4 \tan \theta}$$

4.5.2.2.2 FT-IR analysis

Types of bonding present in molybdenum doped metal oxides (MoZnO, MoZrO, MoWO, and MoSrTiO) was analyzed using Fourier transform infrared (FT-IR). FT-IR spectra was measured with a FT-IR spectrometer (JASCO FT/IR-4100, Tokyo, Japan).

4.5.3 Algae Growth Inhibition

4.5.3.1 Algae culture

A strain of *M. aeruginosa* (No. FBCC000002) was received from the Nakdonggang National Institute of Biological Resources (Sangju, Korea). The MA was cultured in 2-liter conical flask having BG-11 medium (BGM) (pH 7.0) at 298±1K (Zhao et al. 2018), exposed to ~2,000 lx of incandescent lamp with light-dark cycle of 12:12 h. The conical flask was shaken every hour to prevent deposition of the cells.

4.5.3.2 Algae growth inhibition assay

A preliminary study was performed to determine the anti-algal activity of synthesized molybdenum doped metal oxides (MoZnO, MoZrO, MoWO, and MoSrTiO). Different concentrations of molybdenum doped metal oxides were used for growth inhibition of *M. aeruginosa*. Based on the result, MoZnO was used for further study (Figure S1). The stock of MoZnO (1000 mg/L) was prepared in a new BG-11 medium. The resulting solution was ultrasonicated for 15 min to homogenize the MoZnO. *M. aeruginosa* cultures were washed three times and resuspended in fresh culture medium to obtain an eventual concentration of 6.48×10^3 cell/mL (OD680 \approx 0.43), which was nearly equal to the number of toxic concentration of MA blooms occurred in the freshwater bodies (Fan, You, et al. 2019). The MoZnO stock solution was mixed with the *M. aeruginosa* culture to achieve the eventual concentration of 0, 1, 2.5, 5, and 10 mg/L. The resulting

solution was incubated according to the conditions given in section 4.3.1. Next, samples were drawn after successive 1h time-intervals (1-8 h), and the number of algal cells per milliliter was calculated from OD680 using a UV-Vis spectrophotometer (Bio Drop). The growth inhibition rate of algae was calculated using an inhibitory rate equation (Fan, Bao, et al. 2019).

Algae inhibition rate was calculated as follows:

$$\mu_{a-b} = \frac{\ln X_b - \ln X_a}{t_b - t_a}$$

$$I_r = \frac{\mu_0 - \mu_e}{\mu_0} \times 100\%$$

where, μ_{a-b} is the specific growth rate from t_a (h) to t_b (h); X_a is the OD680 value at t_a (h); X_b is the OD680 value at t_b (h); I_r (%) is the inhibition rate based on the specific growth rate; μ_0 is the average of the specific growth rate of the control group; μ_e is the specific growth rate of the experimental group; t_a and t_b are initial and final time measured at 1h interval.

4.5.4 Effect of metal salts, metal oxides and their combinations

The effect of ZnSO₄ (1), (MoCl₅)₂ (2), ZnO (3), Na₂MoO₄·2H₂O (4), and their combinations ZnSO₄+Na₂MoO₄·2H₂O (5), ZnO+Na₂MoO₄·2H₂O (6), ZnSO₄+(MoCl₅)₂ (7), and ZnO+(MoCl₅)₂ (8) was examined on *M. aeruginosa* culture. The ZnSO₄, (MoCl₅)₂, ZnO, or Na₂MoO₄·2H₂O was mixed with *M. aeruginosa* culture to give an eventual concentration of 2.5 mg/L. For combination effect, a 1:1 weight ratio of each component was mixed with *M. aeruginosa* culture to give an eventual concentration of 2.5 mg/L. The control group (0) was set as *M. aeruginosa* culture without any test compound. The resulting solution was incubated according to the conditions given in section 4.3.1. Next, samples were drawn after successive 1h time-intervals (1-8 h), and the number of algal cells per milliliter was calculated from OD680 using a UV-Vis spectrophotometer.

4.5.5 Experiments on Algae Growth Inhibition Mechanisms

4.5.5.1 ·OH assay

Terephthalic acid (TA) is a nonfluorescent compound, which upon oxidation by hydroxyl radical converted into fluorescent compound 2-hydroxyterephthalic acid. Therefore, the fluorescence intensity is directly proportional to the concentration of ·OH. TA (0.5 mM) was dissolved with excess NaOH (2 g/L) in a 100 mL BGM. Then, the BGM was neutralized by adding HCl, and the BGM was equally distributed into two conical flasks (Table 4.4). One group was labelled as control (C) and the other one as experimental group (EX). 1 mM isopropyl alcohol (Ip) was poured to the C group, and MoZnO was mixed with both EX and C groups to achieve the eventual concentration of 10 mg/L, respectively. The EX and C groups were exposed to ~2,000 lx of incandescent lamps for 4 h. The solutions of both EX and C groups were centrifuged at 4500 rpm for 10 minutes. Finally, the fluorescence spectrum of supernatant was analyzed at excitation and emission wavelengths of 350 and 500 nm. The obtained fluorescence intensity was used to compare the ·OH free radicals formed in EX and C groups. The same experiment was performed under the *M. aeruginosa* to study the effect of the shading of algal cells on the efficiency of MoZnO (Figure S8). The experimental (SEX) and control groups (SC) were illuminated with ~2,000 lx of incandescent lamps up to 4 h. The rest procedure was the same to find the ·OH free radical.

Table 4.4. Experimental grouping

Group	Components
EX	BGM + 0.5 mM TA + 10 mg/L MoZnO
SEX	BGM + 0.5 mM TA + 10 mg/L MoZnO
C	BGM + 0.5 mM TA + 1mM Ip +10 mg/L MoZnO
SC	BGM + 0.5 mM TA + 1mM Ip + 10 mg/L MoZnO

4.5.5.2 ROS assay

The intracellular ROS produced in *M. aeruginosa* incubated with MoZnO was evaluated employing 2', 7'-Dichlorofluorescein diacetate (DCFH-DA, Sigma-

Aldrich, USA), which is a nonfluorescent dye. In the cell, esterase catalyzed DCFH-DA to another nonfluorescent 2', 7'-dichlorodihydrofluorescein (DCFH) dye. DCFH further oxidized by $\cdot\text{OH}$ to the extremely fluorescent 2', 7'-dichlorofluorescein (DCF). In detail, 5 mL of *M. aeruginosa* culture was drawn in 15 mL falcon tube from all flasks, at successive time-interval of 1 h. The DCFH-DA solution was mixed with the *M. aeruginosa* culture to make an eventual concentration of 5 μM . Next, wrapped all the tubes with aluminum foil and incubated at 30 °C up to 1 h. Finally, the fluorescence spectrum of *M. aeruginosa* culture was analyzed at excitation and emission wavelengths of 488 and 525 nm, respectively, by making use of a fluorescence spectrometer (F-7000, HITACHI, Japan). The obtained fluorescence intensity was used to calculate the relative ROS content.

4.5.5.3 Lipid peroxidation assay

Lipid peroxidation assay was performed according to Metzler's malondialdehyde (MDA) method (Metzler, Erdem, and Huang 2018). Sample and 10% trichloroacetic acid (TCA) were mixed in the volume ratio of 1:2. The resulting mixture was centrifuged at 11,000 g for 45 min. The supernatant was collected and mixed with 3 mL of 6.7 g/L 2-thiobarbituric acid (TBA). Next, the resulting solution was boiled on the water bath up to 10 min. After the temperature of the solution came to room temperature, the absorbance was measured at the wavelengths of 532 and 600 nm. The obtained value at 600 nm was subtracted from the value at 532 nm. Lipid peroxidation was expressed in terms of mg MDA/kg sample, using molar extinction coefficient for MDA of $1.56 \times 10^5 \text{ M}^{-1} \text{ cm}^{-1}$ (Carmona et al. 2015).

4.5.5.4 Effect of agglomeration

4.5.5.4.1 Optical microscope analysis

A standard experiment was performed to examine the consequence of agglomeration on the multiplication of *M. aeruginosa*. The *M. aeruginosa* culture was incubated with different MoZnO concentrations (0, 1, 2.5, 5, and 10 mg/L) up

to 4 h. The incubated *M. aeruginosa* was analyzed using an optical microscope to detect the aggregated algal cells.

4.5.5.4.2 SEM analysis

SEM analysis was performed to investigate the aggregation of *M. aeruginosa* incubated with 0, 5, and 10 mg/L of MoZnO up to 4 h. *M. aeruginosa* cultures were washed 3-times with double-distilled water and pelleted by centrifugation at 3000 rpm for 10 min. Obtained pellets were fixed with 4% formaldehyde for 1 h at room temperature. Fixed pellets were serially dehydrated with 30% to 100% ethanol. 30 μ L of each sample was put on a glass slide and dried overnight in the open air at room temperature. The SEM analysis of the prepared samples was performed using a (JSM-6490LV, JEOL, Tokyo, Japan) at an accelerating voltage of 0.2 - 30 KV.

4.5.6 Statistical analysis

The experiments were carried out in triplicate, and the data are presented as mean and standard deviation (SD). Significant differences between means were identified using the paired t-test. Statistical significance was evaluated using significance levels at 0.05.

4.6 Conclusions

MoZnO nanoparticles were successfully synthesized by a facile surfactant-free ball-milling method. This method seemed not to be suitable for the synthesis of MoZrO, MoWO, and MoSrTiO in high yield. Out of the MoZnO, MoZrO, MoWO, and MoSrTiO, only MoZnO had a linear relationship between the initial rate of reaction and the concentration of photocatalyst (Preliminary data). Preliminary data indicated that MoZnO was an ideal photocatalyst. Characterization by FESEM, EDX, XRD, and FT-IR measurements indicated that MoZnO contained typical hexagonal wurtzite nanocrystals of approximately 4 nm. The FT-IR spectrum of MoZrO, MoWO, and MoSrTiO showed the presence of a new peak, which may indicate the formation of the M–O–Mo bond (M= Zr, W, and SrTi). FESEM analysis showed that the average particle size of MoZnO was 40 nm. Particle shape and size were found to be strongly altered by ball milling and doping. EDX analysis indicated the presence of Zn, Mo, O, and Cl elements in MoZnO with atomic% of 28.25, 3.23, 61.66, and 6.87, respectively. FT-IR analysis showed the presence of Zn–O–Mo linkage (1038 cm^{-1}) in MoZnO. Investigation of photocatalytic growth inhibition of algal cells showed that the synthesized MoZnO had superior growth-inhibition properties, with MIC value of 1 mg/L under visible light. MoZrO, MoWO, and MoSrTiO were found inactive to control the growth of *M. aeruginosa*. The pristine ZnSO_4 , $(\text{MoCl}_5)_2$, ZnO, $\text{Na}_2\text{MoO}_4\cdot 2\text{H}_2\text{O}$, and their various combinations of $\text{ZnSO}_4+\text{Na}_2\text{MoO}_4\cdot 2\text{H}_2\text{O}$, $\text{ZnO}+\text{Na}_2\text{MoO}_4\cdot 2\text{H}_2\text{O}$, $\text{ZnSO}_4+(\text{MoCl}_5)_2$, and $\text{ZnO}+(\text{MoCl}_5)_2$ did not affect the growth of *M. aeruginosa* significantly. Extracellular $\cdot\text{OH}$ and intracellular ROS oxidized the algal cells, which was supported by lipid peroxidation assay. The shading effect of *M. aeruginosa* decreased the anti-algal efficiency of MoZnO. Extracellular $\cdot\text{OH}$ generated by MoZnO induced the lysis of the *M. aeruginosa* membrane, which leaked the internal organic matter and caused the agglomeration of algal cells. The main mechanism for inhibiting *M. aeruginosa* growth by MoZnO included the

generation of intracellular ROS, extracellular $\cdot\text{OH}$, and oxidative damage to algal cells.



4.7 References

- Abutalib, M. M., and I. S. Yahia. 2017. "Novel and Facile Microwave-Assisted Synthesis of Mo-Doped Hydroxyapatite Nanorods: Characterization, Gamma Absorption Coefficient, and Bioactivity." *Materials Science and Engineering C* 78:1093–1100.
- Afanasiev, P., C. Geantet, and D. H. Kerridge. 1995. "Products of Reactions of Mo and Zr Compounds in Molten Nitrate." *Journal of Materials Chemistry* 5(2):347–52.
- Ahadi, Sina, Nikta S. Moalej, and Saeed Sheibani. 2019. "Characteristics and Photocatalytic Behavior of Fe and Cu Doped TiO₂ Prepared by Combined Sol-Gel and Mechanical Alloying." *Solid State Sciences* 96(August):105975.
- Alan May, R., Lilia Kondrachova, Benjamin P. Hahn, and Keith J. Stevenson. 2007. "Optical Constants of Electrodeposited Mixed Molybdenum-Tungsten Oxide Films Determined by Variable-Angle Spectroscopic Ellipsometry." *Journal of Physical Chemistry C* 111(49):18251–57.
- Anne Vicente, Bénédicte Sohm, Justine Flayac, Philippe Rousselle, Pascale Baudal, Christophe Pagnout. 2019. "Toxicity Mechanisms of ZnO UV-Filters Used in Sunscreens toward the Model Cyanobacteria *Synechococcus Elongatus* PCC 7942." *Environmental Science and Pollution Research* 12(6):1669–77.
- Aruoja, Villem, Henri Charles Dubourguier, Kaja Kasemets, and Anne Kahru. 2009. "Toxicity of Nanoparticles of CuO, ZnO and TiO₂ to Microalgae *Pseudokirchneriella Subcapitata*." *Science of the Total Environment* 407(4):1461–68.
- Autefage, H., F. Allen, H. M. Tang, C. Kallepitis, E. Gentleman, N. Reznikov, K.

- Nitiputri, A. Nommeots-Nomm, M. D. O'Donnell, C. Lange, B. M. Seidt, T. B. Kim, A. K. Solanki, F. Tallia, G. Young, P. D. Lee, B. F. Pierce, W. Wagermaier, P. Fratzl, A. Goodship, J. R. Jones, G. Blunn, and M. M. Stevens. 2019. "Multiscale Analyses Reveal Native-like Lamellar Bone Repair and near Perfect Bone-Contact with Porous Strontium-Loaded Bioactive Glass." *Biomaterials* 209(October 2018):152–62.
- Azizi, Susan, Mansor B. Ahmad, Farideh Namvar, and Rosfarizan Mohamad. 2014. "Green Biosynthesis and Characterization of Zinc Oxide Nanoparticles Using Brown Marine Macroalga *Sargassum Muticum* Aqueous Extract." *Materials Letters* 116:275–77.
- Boningari, Thirupathi, Siva Nagi Reddy Inturi, Makram Suidan, and Panagiotis G. Smirniotis. 2018. "Novel One-Step Synthesis of Sulfur Doped-TiO₂ by Flame Spray Pyrolysis for Visible Light Photocatalytic Degradation of Acetaldehyde." *Chemical Engineering Journal* 339(January):249–58.
- Boukhachem, A., B. Ouni, M. Karyaooui, A. Madani, R. Chtourou, and M. Amlouk. 2012. "Structural, Opto-Thermal and Electrical Properties of ZnO:Mo Sprayed Thin Films." *Materials Science in Semiconductor Processing* 15(3):282–92.
- Brynildsen, Mark P., Jonathan A. Winkler, Catherine S. Spina, I. Cody MacDonald, and James J. Collins. 2013. "Potentiating Antibacterial Activity by Predictably Enhancing Endogenous Microbial ROS Production." *Nature Biotechnology* 31(2):160–65.
- Carmona, Erico R., Claudio Inostroza-Blancheteau, Veroska Obando, Laura Rubio, and Ricard Marcos. 2015. "Genotoxicity of Copper Oxide Nanoparticles in *Drosophila Melanogaster*." *Mutation Research - Genetic Toxicology and Environmental Mutagenesis* 791:1–11.

- Chary, Komandur V. R., Kondakindi Rajender Reddy, Gurram Kishan, J. W. Niemantsverdriet, and Gerhard Mestl. 2004. "Structure and Catalytic Properties of Molybdenum Oxide Catalysts Supported on Zirconia." *Journal of Catalysis* 226(2):283–91.
- Craciun, V., and R. K. Singh. 2000. "Characteristics of the Surface Layer of Barium Strontium Titanate Thin Films Deposited by Laser Ablation." *Applied Physics Letters* 76(14):1932–34.
- Ding, Wenqiang, Lidan Zhao, Hongguang Yan, Xin Wang, Xiaoping Liu, Xiangyu Zhang, Xiaobo Huang, Ruiqiang Hang, Yueyue Wang, Xiaohong Yao, and Bin Tang. 2019. "Bovine Serum Albumin Assisted Synthesis of Ag/Ag₂O/ZnO Photocatalyst with Enhanced Photocatalytic Activity under Visible Light." *Colloids and Surfaces A: Physicochemical and Engineering Aspects* 568(December 2018):131–40.
- Ding, Yanyuan, Lifang Sun, Yanling Jiang, Shunxiang Liu, Mingxing Chen, Miaomiao Chen, Yanan Ding, and Qingyun Liu. 2016. "A Facile Strategy for the Preparation of ZnS Nanoparticles Deposited on Montmorillonite and Their Higher Catalytic Activity for Rapidly Colorimetric Detection of H₂O₂." *Materials Science and Engineering C* 67:188–94.
- Du, Jingjing, Ruilin Guo, Ke Li, Bingbing Ma, Yan Chen, and Yanna Lv. 2019. "Contributions of Zn Ions to ZnO Nanoparticle Toxicity on *Microcystis Aeruginosa* During Chronic Exposure." *Bulletin of Environmental Contamination and Toxicology* 103(0123456789):802–807.
- Ebrahimi, Roya, Khosro Hossienzadeh, Afshin Maleki, Reza Ghanbari, Reza Rezaee, Mahdi Safari, Behzad Shahmoradi, Hiua Daraei, Ali Jafari, Kaan Yetilmezsoy, and Shivaraju Harikaranahalli Puttaiah. 2019. "Effects of Doping Zinc Oxide Nanoparticles with Transition Metals (Ag, Cu, Mn) on

- Photocatalytic Degradation of Direct Blue 15 Dye under UV and Visible Light Irradiation.” *Journal of Environmental Health Science and Engineering* 17(1):479–92.
- Fan, Gongduan, Minchen Bao, Xiaomei Zheng, Liang Hong, Jiajun Zhan, Zhong Chen, and Fangshu Qu. 2019. “Growth Inhibition of Harmful Cyanobacteria by Nanocrystalline Cu-MOF-74: Efficiency and Its Mechanisms.” *Journal of Hazardous Materials* 367:529–38.
- Fan, Gongduan, Yifan You, Bo Wang, Shimin Wu, Zhi Zhang, Xiaomei Zheng, Minchen Bao, and Jiajun Zhan. 2019. “Inactivation of Harmful Cyanobacteria by Ag/AgCl@ZIF-8 Coating under Visible Light: Efficiency and Its Mechanisms.” *Applied Catalysis B: Environmental* 256(April):123767.
- Ghasempour, Fariba, Rouhollah Azimirad, Abbas Amini, and Omid Akhavan. 2015. “Visible Light Photoinactivation of Bacteria by Tungsten Oxide Nanostructures Formed on a Tungsten Foil.” *Applied Surface Science* 338:55–60.
- Gouda, Mohamed. 2012. “Nano-Zirconium Oxide and Nano-Silver Oxide/Cotton Gauze Fabrics for Antimicrobial and Wound Healing Acceleration.” *Journal of Industrial Textiles* 41(3):222–40.
- Halbus, Ahmed F., Tommy S. Horozov, and Vesselin N. Paunov. 2020. “Surface-Modified Zinc Oxide Nanoparticles for Antialgal and Antiyeast Applications.” *ACS Applied Nano Materials* 3(1):440–51.
- He, Xingxing, Changjian Xie, Yuhui Ma, Lin Wang, Xiao He, Weiqun Shi, Xiaodong Liu, Ying Liu, and Zhiyong Zhang. 2019. “Size-Dependent Toxicity of ThO₂ Nanoparticles to Green Algae *Chlorella Pyrenoidosa*.” *Aquatic Toxicology* 209(October 2018):113–20.

- Hoque, Md Ariful, and Marcelo I. Guzman. 2018. "Photocatalytic Activity: Experimental Features to Report in Heterogeneous Photocatalysis." *Materials* 11(10).
- Hou, Jing, Yazhou Wu, Xin Li, Benben Wei, Shiguo Li, and Xiangke Wang. 2018. "Toxic Effects of Different Types of Zinc Oxide Nanoparticles on Algae, Plants, Invertebrates, Vertebrates and Microorganisms." *Chemosphere* 193:852–60.
- Joonas, Elise, Villem Aruoja, Kalle Olli, and Anne Kahru. 2019. "Environmental Safety Data on CuO and TiO₂ Nanoparticles for Multiple Algal Species in Natural Water: Filling the Data Gaps for Risk Assessment." *Science of the Total Environment* 647:973–80.
- Kalanur, Shankara S., and Hyungtak Seo. 2018. "Influence of Molybdenum Doping on the Structural, Optical and Electronic Properties of WO₃ for Improved Solar Water Splitting." *Journal of Colloid and Interface Science* 509:440–47.
- Khaki, Mohammad Reza Delsouz, Mohammad Saleh Shafeeyan, Abdul Aziz Abdul Raman, and Wan Mohd Ashri Wan Daud. 2017. "Application of Doped Photocatalysts for Organic Pollutant Degradation - A Review." *Journal of Environmental Management* 198:78–94.
- Kim, Dongin, Geonwoo Kim, Hyeonbin Bae, Eunwoo Kim, Byunghyun Moon, and Daho Cheon. 2019. "An External Energy Independent WO₃/MoCl₅ Nano-Sized Catalyst for the Superior Degradation of Crystal Violet and Rhodamine B Dye." *Catalysts* 9(8):642.
- Lebedev, Andrei, Franklin Anariba, Jeck Chuang Tan, Xu Li, and Ping Wu. 2018. "A Review of Physiochemical and Photocatalytic Properties of Metal Oxides against Escherichia Coli." *Journal of Photochemistry and Photobiology A:*

Chemistry 360:306–15.

- Li, Fengmin, Zhi Liang, Xiang Zheng, Wei Zhao, Miao Wu, and Zhenyu Wang. 2015. “Toxicity of Nano-TiO₂ on Algae and the Site of Reactive Oxygen Species Production.” *Aquatic Toxicology* 158:1–13.
- Lonkar, Sunil P., Vishnu Pillai, and Ahmed Abdala. 2019. “Solvent-Free Synthesis of ZnO-Graphene Nanocomposite with Superior Photocatalytic Activity.” *Applied Surface Science* 465(August 2018):1107–13.
- Madhavi, V., P. Jeevan Kumar, P. Kondaiah, O. M. Hussain, and S. Uthanna. 2014. “Effect of Molybdenum Doping on the Electrochromic Properties of Tungsten Oxide Thin Films by RF Magnetron Sputtering.” *Ionics* 20(12):1737–45.
- Metzler, David M., Ayca Erdem, and Chin Pao Huang. 2018. “Influence of Algae Age and Population on the Response to Tio₂ Nanoparticles.” *International Journal of Environmental Research and Public Health* 15(4):501–6.
- Mitran, Gheorghita, Florentina Neațu, Octavian D. Pavel, Mihaela M. Trandafir, and Mihaela Florea. 2019. “Behavior of Molybdenum-Vanadium Mixed Oxides in Selective Oxidation and Disproportionation of Toluene.” *Materials* 12(5):748.
- Nakagaki, Shirley, Alesandro Bail, Vannia Cristina dos Santos, Victor Hugo Rodrigues de Souza, Heron Vrubel, Fábio Souza Nunes, and Luiz Pereira Ramos. 2008. “Use of Anhydrous Sodium Molybdate as an Efficient Heterogeneous Catalyst for Soybean Oil Methanolysis.” *Applied Catalysis A: General* 351(2):267–74.
- Nasir, Zeba, Mohammad Lutfullah Shakir, Rizwan Wahab, Mohd Shoeb, Parvez Alam, Rizwan Hasan Khan, and Mohammad Mobin. 2017. “Co-Precipitation Synthesis and Characterization of Co Doped SnO₂ NPs, HSA Interaction via

Various Spectroscopic Techniques and Their Antimicrobial and Photocatalytic Activities.” *International Journal of Biological Macromolecules* 94:554–65.

Nosaka, Yoshio, Shinichiro Takahashi, Yasufumi Mitani, Xiaoqing Qiu, and Masahiro Miyauchi. 2012. “Reaction Mechanism of Visible-Light Responsive Cu(II)-Grafted Mo-Doped SrTiO₃ Photocatalyst Studied by Means of ESR Spectroscopy and Chemiluminescence Photometry.” *Applied Catalysis B: Environmental* 111–112:636–40.

Oukarroum, Abdallah, Ilias Halimi, and Mohamed Siaj. 2019. “Cellular Responses of Chlorococcum Sp. Algae Exposed to Zinc Oxide Nanoparticles by Using Flow Cytometry.” *Water, Air, and Soil Pollution* 230(1):1–7.

Phongarthit, Kanitta, Pongsaton Amornpitoksuk, and Sumetha Suwanboon. 2019. “Synthesis, Characterization, and Photocatalytic Properties of ZnO Nanoparticles Prepared by a Precipitation-Calcination Method Using a Natural Alkaline Solution.” *Materials Research Express* 6(4):45501.

Quek, Jian Ai, Sze Mun Lam, Jin Chung Sin, and Abdul Rahman Mohamed. 2018. “Visible Light Responsive Flower-like ZnO in Photocatalytic Antibacterial Mechanism towards Enterococcus Faecalis and Micrococcus Luteus.” *Journal of Photochemistry and Photobiology B: Biology* 187(August):66–75.

Reddy, K. Vasudeva, D. Nagarjuna Reddy, and K. Hussain Reddy. 2011. “Study of Synthesis and Photocatalytic Activities of Mo Doped ZnO.” *Journal of Chemical and Pharmaceutical Research* 3(2):234–44.

Rusu, D. I., G. G. Rusu, and D. Luca. 2011. “Structural Characteristics and Optical Properties of Thermally Oxidized Zinc Films.” *Acta Physica Polonica A* 119(6):850–56.

- Shafei, A., M. E. Salarpour, and S. Sheibani. 2019. "Effect of Intermediate Ball Milling on the Synthesis of Cu-Doped TiO₂ Nano-Photocatalyst by Sol-Gel Method." *Journal of Sol-Gel Science and Technology* 92(1):173–185.
- Shatnawi, M., A. M. Alsmadi, I. Bsoul, B. Salameh, M. Mathai, G. Alnawashi, Gassem M. Alzoubi, F. Al-Dweri, and M. S. Bawa'aneh. 2016. "Influence of Mn Doping on the Magnetic and Optical Properties of ZnO Nanocrystalline Particles." *Results in Physics* 6(November):1064–71.
- Shu, Zhanxia, Xiuling Jiao, and Dairong Chen. 2012. "Synthesis and Photocatalytic Properties of Flower-like Zirconia Nanostructures." *CrystEngComm* 14(3):1122–27.
- Silva, Bruna Lallo da, Marina Paiva Abuçafy, Eloisa Berbel Manaia, João Augusto Oshiro Junior, Bruna Galdorfini Chiari-Andréo, Rosemeire C. L. R. Pietro, and Leila Aparecida Chiavacci. 2019. "Relationship between Structure and Antimicrobial Activity of Zinc Oxide Nanoparticles: An Overview." *International Journal of Nanomedicine* 14:9395–9410.
- Sousa, Cátia A., Helena M. V. M. Soares, and Eduardo V. Soares. 2019. "Chronic Exposure of the Freshwater Alga *Pseudokirchneriella subcapitata* to Five Oxide Nanoparticles: Hazard Assessment and Cytotoxicity Mechanisms." *Aquatic Toxicology* 214(April):105265.
- Suman, T. Y., S. R. Radhika Rajasree, and R. Kirubakaran. 2015. "Evaluation of Zinc Oxide Nanoparticles Toxicity on Marine Algae *Chlorella vulgaris* through Flow Cytometric, Cytotoxicity and Oxidative Stress Analysis." *Ecotoxicology and Environmental Safety* 113:23–30.
- Swapna, R., and M. C. Santhosh Kumar. 2013. "Growth and Characterization of Molybdenum Doped ZnO Thin Films by Spray Pyrolysis." *Journal of Physics*

and Chemistry of Solids 74(3):418–25.

- Theerthagiri, J., Sunitha Salla, R. A. Senthil, P. Nithyadharseni, A. Madankumar, Prabhakarn Arunachalam, T. Maiyalagan, and Hyun-seok Kim. 2019. “A Review on ZnO Nanostructured Materials: Energy, Environmental and Biological Applications.” *Nanotechnology* 30(39):392001.
- Xie, Shuibo, Kaidong Chen, Alexis T. Bell, and Enrique Iglesia. 2000. “Structural Characterization of Molybdenum Oxide Supported on Zirconia.” *Journal of Physical Chemistry B* 104(43):10059–68.
- Xiu, Xianwu, Zhiyong Pang, Maoshui Lv, Ying Dai, Lina Ye, and Shenghao Han. 2007. “Transparent Conducting Molybdenum-Doped Zinc Oxide Films Deposited by RF Magnetron Sputtering.” *Applied Surface Science* 253(6):3345–48.
- Yan, Xu, Shaofang Sun, Bo Hu, Xiyong Wang, Wei Lu, and Weidong Shi. 2013. “Enhanced Photocatalytic Activity Induced by Surface Plasmon Resonance on Ag-Loaded Strontium Titanate Nanoparticles.” *Micro and Nano Letters* 8(9):504–7.
- Yin, Haibo, Yasutaka Kuwahara, Kohsuke Mori, Hefeng Cheng, Meicheng Wen, Yuning Huo, and Hiromi Yamashita. 2017. “Localized Surface Plasmon Resonances in Plasmonic Molybdenum Tungsten Oxide Hybrid for Visible-Light-Enhanced Catalytic Reaction.” *Journal of Physical Chemistry C* 121(42):23531–40.
- Yu, Changlin, Kai Yang, Qing Shu, Jimmy C. Yu, Fangfang Cao, Xin Li, and Xiaochun Zhou. 2012. “Preparation, Characterization and Photocatalytic Performance of Mo-Doped ZnO Photocatalysts.” *Science China Chemistry* 55(9):1802–10.

- Yu, Xiaojuan, Jiangya Zhou, Zhiping Wang, and Weimin Cai. 2010. "Preparation of Visible Light-Responsive AgBiO₃ Bactericide and Its Control Effect on the *Microcystis Aeruginosa*." *Journal of Photochemistry and Photobiology B: Biology* 101(3):265–70.
- Zhao, Miaomiao, Xinyi Chen, Ning Ma, Qiuyue Zhang, Dong Qu, and Ming Li. 2018. "Overvalued Allelopathy and Overlooked Effects of Humic Acid-like Substances on *Microcystis Aeruginosa* and *Scenedesmus Obliquus* Competition." *Harmful Algae* 78(July):18–26.
- Zhou, Shiqing, Yisheng Shao, Naiyun Gao, Shumin Zhu, Lei Li, Jing Deng, and Minqiu Zhu. 2014. "Removal of *Microcystis Aeruginosa* by Potassium Ferrate (VI): Impacts on Cells Integrity, Intracellular Organic Matter Release and Disinfection by-Products Formation." *Chemical Engineering Journal* 251:304–9.
- Znaidi, Lamia, Tahar Touam, Dominique Vrel, Nacer Souded, Sana Ben Yahia, Ovidiu Brinza, Alexis Fischer, and Azzedine Boudrioua. 2013. "AZO Thin Films by Sol-Gel Process for Integrated Optics." *Coatings* 3(3):126–39.

Chapter 5

Microwave-Assisted Synthesis and Characterization of Solar-Light-Active Copper–Vanadium Oxide: Evaluation of Antialgal and Dye Degradation Activity

5.1 Abstract

Toxins producing freshwater algae and dye are the main water pollutants. Immediate action is required to rid-off these issues. To deal with this issue copper-vanadium oxide (Cu-VO) was fabricated by a novel and easy microwave irradiation method. Cu-VO was successfully characterized by analyzing microstructure, atomic composition, crystal structure, surface chemistry, and types of binding using FESEM, EDS, XRD, XPS, and FTIR spectroscopy, respectively. The effect of Cu-VO on algal growth and dye concentration under solar light was examined against *Microcystis aeruginosa* (*M. aeruginosa*) and methylene blue (MB). The photocatalytic mechanism of Cu-VO was studied using $\cdot\text{OH}$ and ROS assays. Cu-VO had a spheroid shape with 132 nm in diameter. The crystals of Cu-VO had a monoclinic arrangement with $\text{Cu}_3\text{V}_2\text{O}_8$ atomic composition. FTIR showed the presence of tetrahedral VO_4 and octahedral CuO_6 in Cu-VO. Algal growth inhibition was achieved at 4 ppm, and dye degradation at 20 ppm under solar light. $\cdot\text{OH}$ radical and ROS played a major role in photocatalytic activity of Cu-VO. Further, this work suggested that the microwave method could be a green and efficient method for the synthesis of the solar light active photocatalyst.

5.2 Introduction

Water contamination due to toxic cyanobacteria and dye effluents diminishes water quality and causes health risk to humans and aquatic animals. Increased industrialization, global warming, and high living standards contributes to the water pollution and poses continuing risks to human health. Water pollutants, such as blooming harmful cyanobacteria and dye limited the access to fresh drinking water and sanitation, which necessitates the remediation of these pollutants (C. Zhang et al. 2019). Several strains of bloom-forming cyanobacteria such as *Anabaena*, *Microcystis*, *Oscillatoria* etc., are found in aquatic system (Dai et al. 2016). Out of these strains *Microcystis aeruginosa* (*M. aeruginosa*) is a major bloom-forming freshwater blue-green algae (El-Sheekh, Haroon, and Sabae 2017; Halbus, Horozov, and Paunov 2020). Textile, paper, cosmetic, and dye industries discharge unused dye into water (Begum et al. 2020). Methylene blue (MB) is a major industrial waste discharged into water (Ray et al. 2017). *M. aeruginosa* contaminates freshwater by releasing cyanotoxins such as neurotoxins and hepatotoxins, whereas MB is toxic for aquatic animals and humans. These issues could be counter by applying the efficient, cheap, and easy technique.

Semiconductor photocatalysts are a clean sustainable solar energy-based system that could be a promising and attractive strategy to deal with blooming *M. aeruginosa* (Nandanwar et al. 2020) and MB pollutants (Ray et al. 2017). Irradiation of photocatalysts with higher light energy than its bandgap generates electrons and holes in the conduction and valence band (Lebedev et al. 2018). These excited photocatalysts can efficiently oxidize or reduce surrounding pollutants, which arouse their substantial interest in the degradation of environmental pollutants. Vanadium pentoxide (V_2O_5) is an efficient *n*-type semiconductor photocatalyst for the degradation organic pollutants, due to its benign nature, high chemical and light stability, and visible light activity (Jayaraj et al. 2018). V_2O_5 showed poor degradation efficiency towards methylene blue dye (Jayaraj et al.

2018). Fabrication of metal oxide composites of V_2O_5 is an effective strategy for the improvement of degradation efficiency towards methylene blue dye (Zelege and Kuo 2019). Recently, visible light active transition metal vanadates have been intensively researched for various applications such as antimicrobial activity (Simo et al. 2018), dye degradation (Suresh et al. 2014), optical devices (He et al. 2018), lithium batteries (Ni et al. 2015), etc. Out of several transition metal vanadates, $Cu_3V_2O_8$ has been extensively studied for photocatalytic performances and electrochemical properties (Seabold and Neale 2015). Copper vanadate is a natural mineral identified as pseudolyonsite (Zelenski et al. 2011) and has been extensively used for O_2 production (Seabold and Neale 2015), battery (Zhang et al. 2013), and dye degradation (Ghiyasiyan-Arani, Masjedi-Arani, and Salavati-Niasari 2016). Jain et al. (Jain et al. 2020) found that the precursor of $Cu_3V_2O_8$ i.e. $Cu_3V_2O_7(OH)_2 \cdot 2H_2O$ behave like peroxidase enzyme. Peroxidase enzymes mimicking metal oxides have a potential of oxidative degradation of microbial cell membrane (Karim et al. 2018). The literature survey showed that the anti-algal activity of $Cu_3V_2O_8$ is not yet been studied. Therefore, it is important to investigate the antialgal activity of $Cu_3V_2O_8$.

Semiconductor photocatalysts oxidize water under light to produce reactive oxygen species such as hydroxyl free radicals ($\cdot OH$) (Jing et al. 2020). $\cdot OH$ is a highly reactive species with high oxidation potential and can degrade organic pollutants (Kadam et al. 2020) and microorganism in aqueous medium (X. Zhang et al. 2019). Several studies have indicated that photocatalysts can also cause oxidative stress in algal cells by increasing the intracellular ROS level, which can damage DNA, RNA, proteins, and lipids, leading to cell death (Brynildsen et al. 2013; Suman, Radhika Rajasree, and Kirubakaran 2015; Yan et al. 2013). Thus, water oxidation property of semiconductor is a critical mechanism for environmental abatement.

Here, we attempted to synthesize Cu-VO using the microwave method. Cu-VO was characterized using Field emission scanning electron microscope (FESEM), energy dispersive X-ray analysis (EDX), X-ray diffraction (XRD), X-ray photoelectron spectroscopy (XPS), and FT-IR spectroscopy. The anti-alga and dye degradation efficiency of Cu-VO was inspected under the direct sunlight. The effect of precursor metal salts on algal growth was investigated as a control experiment. Furthermore, the mechanisms of action of Cu-VO were investigated in terms of the production of extracellular hydroxyl radical ($\cdot\text{OH}$) and intracellular ROS assay.



5.3. Results

5.3.1 Synthesis, morphological and microstructural analysis of Cu-VO

Microwave irradiation of aqueous mixture of blue-colored $\text{Cu}(\text{NO}_3)_2$ and white KVO_3 lead the formation of bright yellow colored Cu-VO. Upon annealing bright yellow colored Cu-VO at $400\text{ }^\circ\text{C}$ for 2h, the color changed to brown. The obtained weight of the final product was 0.0326 g out of net weight of reactants used (0.0464 g).

The FESEM image of Cu-VO showed the presence of well-dispersed spheroid-like particles (Figure 5.1) (Li et al. 2016). Cu-VO had particle size between 25 nm to 350 nm. The average particle size of Cu-VO was 133 nm. Due to the smaller particle size of Cu-VO, it had high surface area, surface energy, and reactivity. EDX spectrum of Cu-VO showed the presence of Cu, V, and O elements in the single crystal of Cu-VO (Figure 5.2). The weight% and atomic% of the elements present in Cu-VO are shown in Table 5.1. The calculated atomic ratio Cu: V: O using EDX data was 3.13: 2: 7.25. It showed that the product Cu-VO may had single phase of $\text{Cu}_3\text{V}_2\text{O}_8$.

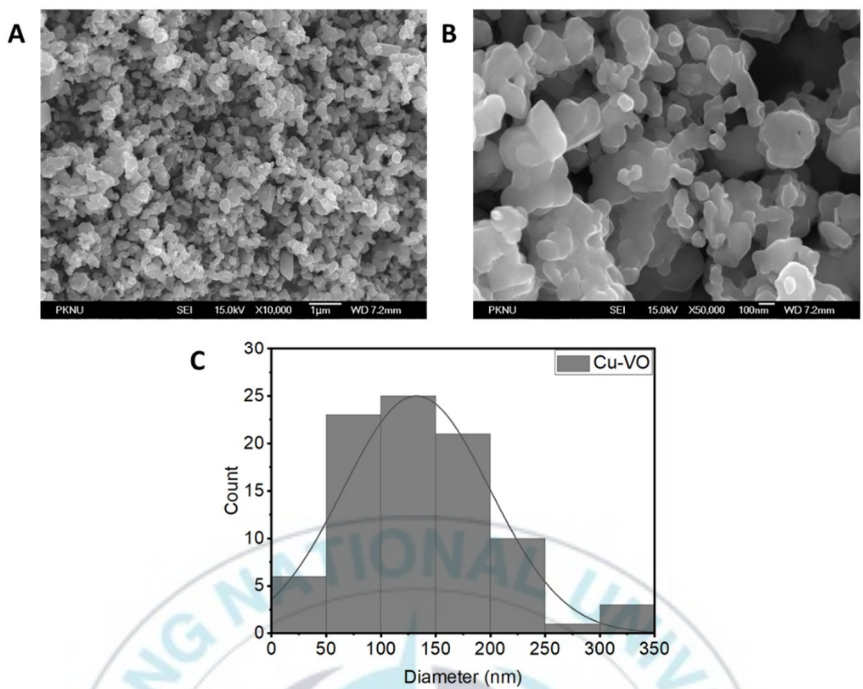


Figure 5.1. FESEM image of Cu-VO (A) low magnification and (B) high magnification, and (C) particle size distribution.

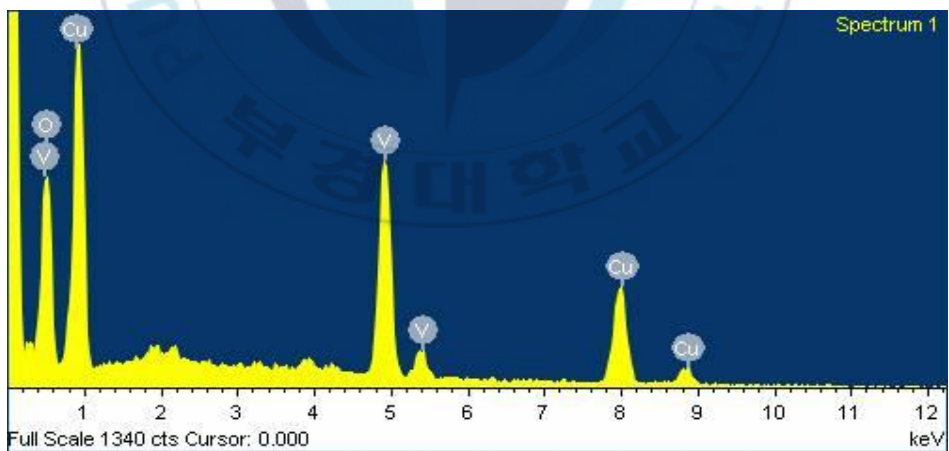


Figure 5.2. EDX spectrum of Cu-VO.

Table 5.1. Element proportion analysis of Cu-VO.

Element	Weight%	Atomic%
O	27.90	58.64
V	24.41	16.12
Cu	47.69	25.24

5.3.2 Structural analysis of Cu-VO

The XRD plot of Cu-VO showed the presence of (100), (-110), (020), (021), (111), (-121), (-211), (021), (121), (-212), (130), (-131), (102), (211), (040), (031), (-123), (212), (-142), (042), (-233), and (-330) peaks (Figure 5.3) (Li et al. 2016). All these diffraction peaks corresponded to the monoclinic $\text{Cu}_3\text{V}_2\text{O}_8$ phase with space group P21/c (JCPDS card no. 26-0567) (Li et al. 2016). These results showed the presence of single phase crystals $\text{Cu}_3\text{V}_2\text{O}_8$ in Cu-VO (Li et al. 2016). These results matched well with the EDS analysis of Cu-VO.

The crystallinity of Cu-VO was analyzed using an X-ray diffractometer (Rigaku Ultima IV, Rigaku, Japan), with Cu $K\alpha$ radiation (wavelength = 1.54 nm) operated at 40 kV and 40 mA. The crystallite size D of Cu-VO was calculated using the Scherrer equation (Table 2) (Ghiyasiyan-Arani, Masjedi-Arani, and Salavati-Niasari 2016):

$$D = \frac{k\lambda}{\beta \cos \theta}$$

where D is the crystalline size; k is the shape factor (0.9); λ is the wavelength of X-ray (1.54056 Å); β is the Full Width at Half Maximum (FWHM) of the diffraction peak (in radians); θ is the diffraction angle of the reflection.

The lattice constants were measured by applying the following equation (Table 2) (Saud et al. 2014):

$$\frac{1}{d^2} = \frac{1}{\sin^2 \beta} \left(\frac{h^2}{a^2} + \frac{k^2 \sin^2 \beta}{b^2} + \frac{l^2}{c^2} - \frac{2hl \cos \beta}{ac} \right)$$

where a, b, c are the lattice parameters and d is the spacing between the (hkl) planes. β is the unique interaxial angle, reported to be 111.49° for monoclinic $\text{Cu}_3\text{V}_2\text{O}_8$ crystal system (Shannon and Calvo 1972).

The lattice strain (ϵ) was measured using the tangent formula (Table 5.2) (Boukhachem et al. 2012):

$$\epsilon = \frac{\beta}{4 \tan \theta}$$

where β is the Full Width at Half Maximum (FWHM) of the diffraction peak (in radians); θ is the diffraction angle of the reflection.

Table 5.2. Calculated crystallite size, lattice constants, and microstrain values of Cu-VO.

Material	Crystallite size (nm)	Lattice constant (Å)			Lattice strain (ϵ)
		a	b	c	
Cu-VO	58 ± 10	6.28	7.99	6.39	0.13 ± 0.03

The high resolution XPS spectrum of Cu 2p showed the main characteristic doublet peaks at 955 eV and 935 eV, corresponding to $\text{Cu}^{2+} 2p_{3/2}$ and $\text{Cu}^{2+} 2p_{1/2}$ (Figure 5.4A) (Akgul et al. 2014). Additional two strong satellite peaks other than the main peaks of Cu 2p appeared at 962.5 eV and 942 eV. The binding energy (BE) difference of the spin-orbits of $\text{Cu}^{2+} 2p_{3/2}$ and $\text{Cu}^{2+} 2p_{1/2}$ was approximately 20 eV, which matched well with the values reported earlier (Akgul et al. 2014). The multiple excitations of CuO generated the satellite peaks on the higher BE side of the core level Cu 2p XPS. These satellite peaks were attributed to the $2p^03d^9$ configuration of Cu^{2+} in the CuO phase (Svintsitskiy, Yu. Kardash, and Boronin 2019). The high resolution XPS spectrum of V 2p showed the main characteristic doublet peaks $\text{V}^{5+} 2p_{3/2}$ and $\text{V}^{5+} 2p_{1/2}$ at 517.3 eV and 525.1 eV, respectively (Figure 5.4B). The difference between BE of $\text{V}^{5+} 2p_{3/2}$ and $\text{V}^{5+} 2p_{1/2}$ was 7.8 eV, which matched well with the values reported earlier (Li et al. 2016). The XPS spectrum

of O 1s showed a main peak at 530.5 eV, which corresponded to O^{2-} 1s (Figure 5.4C).

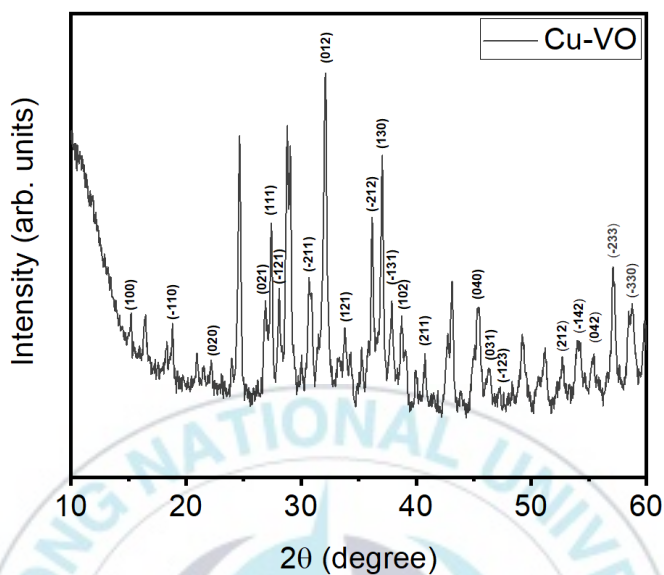


Figure 5.3. X-ray diffraction patterns of Cu-VO.

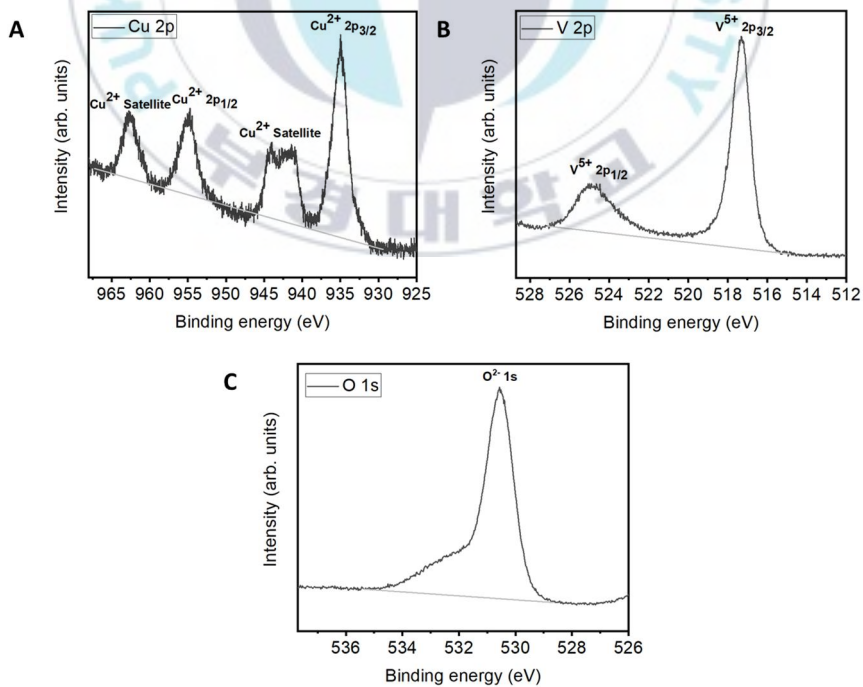


Figure 5.4. XPS spectra of Cu-VO A) Cu B) V, and C) O.

The FT-IR spectrum of Cu-VO was shown in Figure 5.5. The absorption band in the range of 3750-3250 cm^{-1} could be assigned to the stretching vibration of the hydroxyl groups of the water adsorbed on the surface of Cu-VO (Ghiyasiyan-Arani, Masjedi-Arani, and Salavati-Niasari 2016). The bending vibration of hydroxyl group was appeared at around 1630 cm^{-1} . The FT-IR spectrum of Cu-VO showed the characteristic bands for VO_4^{3-} at 900-700 cm^{-1} (Liu et al. 2009). The vibration of Cu-O bond was appeared at around 420 cm^{-1} in the FT-IR spectrum (Lin, Li, and Yang 2018). The vibration bands in the range of 960–450 cm^{-1} indicated the presence of tetrahedral VO_4 and octahedral CuO_6 crystals in Cu-VO. FT-IR spectra of Cu-VO matched well with the XRD and EDS results.

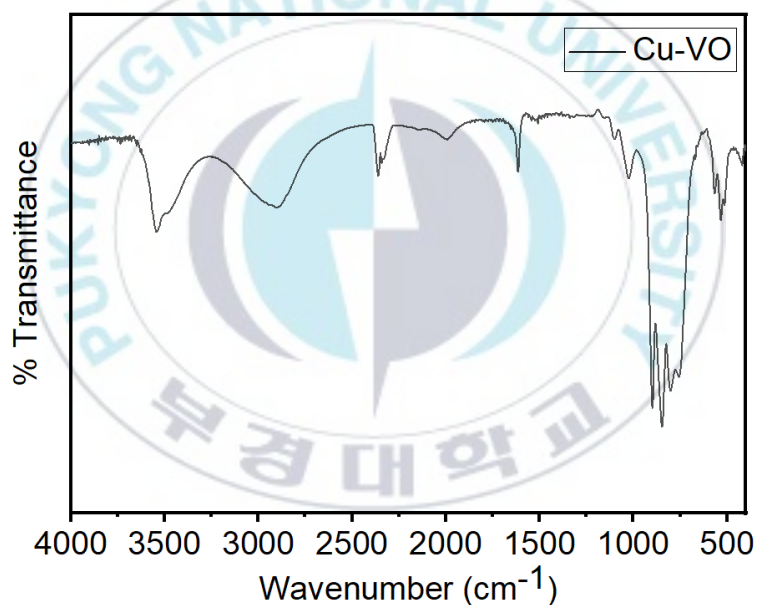


Figure 5.5. FT-IR spectra of Cu-VO.

5.3.3 Anti-algal Assay

The anti-algal activity of Cu-VO was represented in Figure 5.6. A change in the pigment of *M. aeruginosa* was observed after incubating with various concentrations of Cu-VO (Figure 5.6A). Cu-VO showed concentration-dependent growth inhibited of *M. aeruginosa*. The culture of *M. aeruginosa* incubated with 8

mg/L, 12 mg/L, and 24 mg/L of Cu-VO displayed alteration of pigment dark green to faint green within 3 h of incubation, whereas 4 mg/L of Cu-VO exhibited a change in pigment within 4 h of incubation. The lowest concentration of Cu-VO (0.4 mg/L) was found inefficient for algal growth inhibition.

OD680 value of *M. aeruginosa* was decreased in a concentration-dependent manner (Figure 5.6B). The kinetics of algal growth inhibition was initially slow, whereas sudden increase was observed after specific time interval. The algal cells incubated with 0.4 mg/L of Cu-VO and KVO_3 showed growth of algae similar to control (C). This indicated that precursor compounds were ineffective for algal growth inhibition. Overall, the suppression of *M. aeruginosa* growth due to the presence of Cu-VO was justified in this work, and the minimum effective concentration was found to be 4 mg/L.

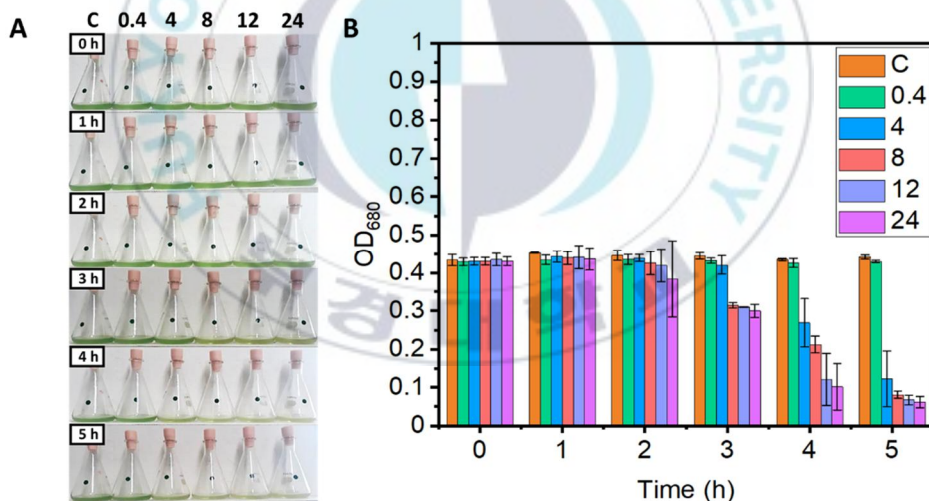


Figure. 5.6. Growth inhibition of *M. aeruginosa* by Cu-VO with time. (A) Change in pigment of *M. aeruginosa* suspension, and (B) Change in OD680 of *M. aeruginosa*.

5.3.4 Dye degradation assay

The UV-Vis spectrum of methylene blue (MB) treated with Cu-VO was shown in Figure 5.7A. The absorbance of MB decreased with time, indicating the decreased concentration in presence of Cu-VO. The color of the MB dye solution almost disappeared within 6 h of the addition of the catalyst. The % degradation of MB was represented in Figure 5.7B. Cu-VO degraded almost 93% of MB within 6 h of incubation under sunlight.

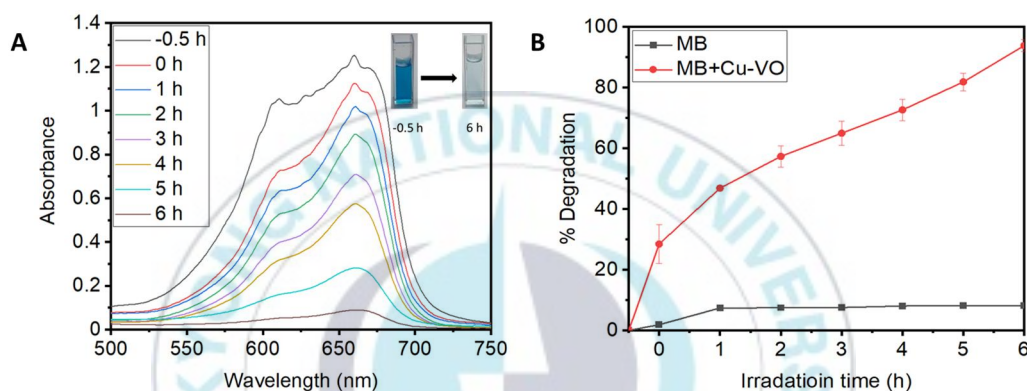
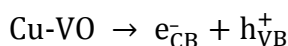


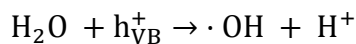
Figure 5.7. UV-vis absorbance spectra (A) and % degradation of 50 μM MB (B) treated with Cu-VO catalyst at different time interval.

5.3.5 Mechanism of action

Generation of extracellular $\cdot\text{OH}$ by Cu-VO in BGM, under direct solar light (C, E) was investigated using $\cdot\text{OH}$ assay (Figure 5.8). The fluorescence intensity of the control groups (C) was lower than that of the experimental groups (E). Isopropanol scavenged the $\cdot\text{OH}$ formed by nanomaterials, thus decreasing the $\cdot\text{OH}$ fluorescence intensity of the control group (Phongarthit, Amornpitoksuk, and Suwanboon 2019). The fluorescence intensity of experimental groups is 1.42-fold than control group.

The plausible steps for the generation of $\cdot\text{OH}$ free radical by Cu-VO were given as follows:





The irradiation of Cu-VO with solar light caused the generation of a negatively charged conduction band (e_{CB}^-) and positively charged valence band (h_{VB}^+) (Ali et al. 2018). The h_{VB}^+ extracted electrons from nearby water molecules, producing hydroxyl radicals and protons. The high oxidation potential of the generated $\cdot\text{OH}$ can damage harmful cyanobacteria and dye.

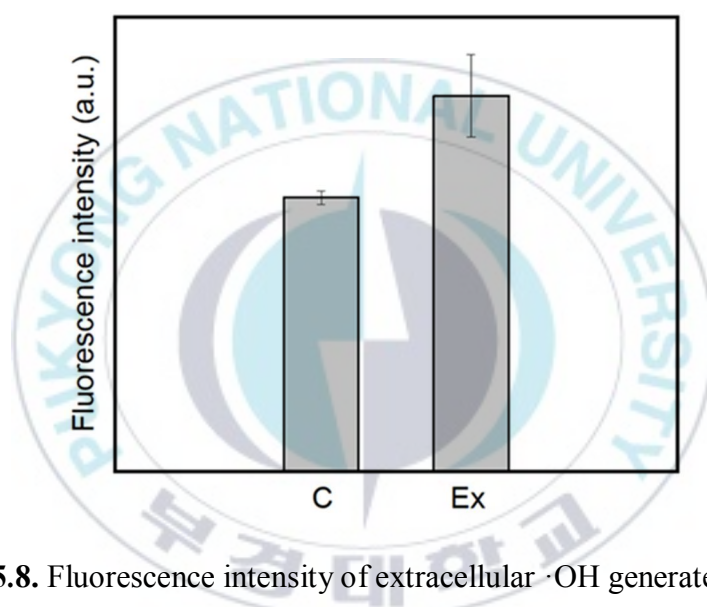


Figure 5.8. Fluorescence intensity of extracellular $\cdot\text{OH}$ generated at 4 h. C and EX are control and experimental groups under open air.

Intracellular ROS induced by different concentrations of Cu-VO in the *M. aeruginosa* cells was measured up to 4 h (Figure 5.9). *M. aeruginosa* cells showed concentration-dependent intracellular ROS production. ROS was a highly unstable and reactive species. ROS concentration changed at every fraction of a second. The rapid change in concentration could give improper results.

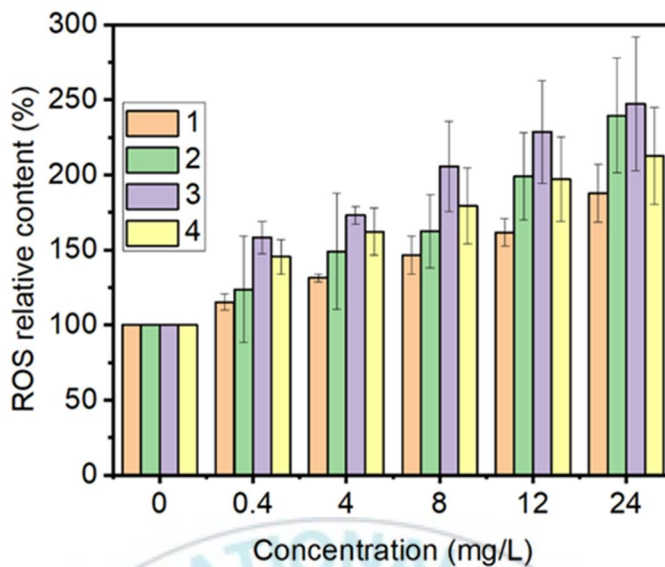
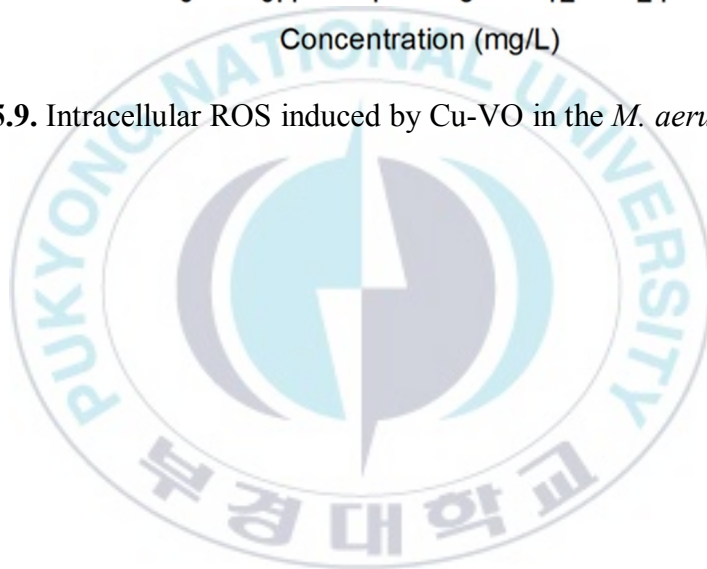


Figure 5.9. Intracellular ROS induced by Cu-VO in the *M. aeruginosa* cells.



5.4. Discussion

In this study, we successfully synthesized nano-size Cu-VO using the microwave-assisted synthesis method. The synthesis of Cu-VO required very little time (10 min) compared to other methods such as thermal decomposition (Shannon and Calvo 1972), simple heating (Zhang et al. 2013; Li et al. 2016; Seabold and Neale 2015; Ghiyasiyan-Arani, Masjedi-Arani, and Salavati-Niasari 2016; Ghiyasiyan-Arani, Masjedi-Arani, Ghanbari, et al. 2016), and hydrothermal (Leblanc and Ferey 1990) for the synthesis of Cu-VO. These results indicated that microwave-assisted synthesis of Cu-VO is a highly efficient method for the synthesis of Cu-VO. FESEM, XRD, and XPS results of Cu-VO matched well with the results obtained by Li et al. (Li et al. 2016). The size of Cu-VO was twice the size obtained by Li et al. (Li et al. 2016). Cu-VO had a spheroid shape with a monoclinic crystal structure.

Cu-VO showed rapid growth inhibition of *M. aeruginosa* at a minimum concentration of 4 mg/L within 4 h under solar light, whereas the precursor compound KVO_3 had no effect on *M. aeruginosa* growth. CuO nanoparticles inhibited algal growth within 96 h at a concentration of 50 mg/L (Sankar et al. 2014). Cu-MOF-74 inhibited the growth of algal cells within 120 h at an effective concentration of 5 mg/L (Fan et al. 2019). Cu-g- C_3N_4 showed algal growth inhibition within 96 h at an effective concentration of 100 mg/mL (Cao et al. 2021). These results indicated that Cu-VO was a highly efficient anti-algal agent.

The solar light active Cu-VO (20 ppm) degraded 93 % MB (50 μ M) within 6 h. Twenty ppm of V_2O_5 showed poor MB (50 μ M) degradation efficiency (24%) within 3 h than the same concentration of Rhodamine 6G (83%) and methyl orange (48%) under visible light (Jayaraj et al. 2018). The UV-Vis active hollow $Cu_3V_2O_8$ (1000 ppm) degraded 78% of methyl orange (20 ppm) within 2 h (Zhang et al. 2013). The in situ and ex situ prepared $Cu_3V_2O_8$ - $Cu_2V_2O_7$ (250 ppm) degraded 51% and 83% of methylene blue (20 ppm) within 2 h under UV light, respectively

(Ghiyasiyan-Arani, Masjedi-Arani, and Salavati-Niasari 2016). Five hundred mg of visible light active V_2O_5/ZnO composite efficiently degraded the 500 mg of MB solution within 2 h (Saravanan et al. 2014). The quantum dots of vanadium oxide was found inefficient for the degradation of Rhodamine B (25 ppm) or MB, but the same quantum dots were highly efficient in combination with H_2O_2 or magnetic $Fe_3O_4@SiO_2 + H_2O_2$ (M. Zhang, Niu, and Xu 2020). All these results indicated that Cu-VO was highly efficient for MB degradation compared to V_2O_5 , moderately efficient compared to hollow $Cu_3V_2O_8$ or $Cu_3V_2O_8-Cu_2V_2O_7$, but poorly efficient compared to V_2O_5/ZnO or $V_2O_5 + H_2O_2$ or $V_2O_5 +$ magnetic $Fe_3O_4@SiO_2 + H_2O_2$. Also, the dye degradation efficiency of pristine V_2O_5 could be strongly enhanced in a combination with other transition metal oxides and H_2O_2 .

Metal oxides generated reactive oxygen species (ROS) such as $\cdot OH$, $\cdot O_2^-$, h^+ , and $HO_2\cdot$ in presence of light (Habibi-Yangjeh et al. 2020). ROS has a high oxidation potential to oxidize organic contaminants such as microorganisms, dye, and other pollutants. Regmi et al. (Regmi et al. 2017) found that nickel doped bismuth vanadate generated $\cdot OH$, $\cdot O_2^-$, and h^+ under visible light. Zhang et al. (N. Zhang et al. 2020) found that copper vanadium oxide rapidly dissociated H_2O_2 to produce $\cdot OH$ for the degradation of fluconazole. The enhanced dye degradation efficiency of V_2O_5 in the presence of H_2O_2 , indicating the generation of reactive $\cdot OH$, played a crucial role in dye degradation (M. Zhang et al. 2020). Zinc doped copper oxide nanoparticles generated reactive $\cdot OH$ for the growth inhibition of Multi-Drug Resistant Bacteria (Malka et al. 2013). Based on this research, we hypothesized that Cu-VO could generate $\cdot OH$ in the medium, which can degrade algal cells and dye. The increased fluorescence intensity of terephthalic acid in the presence of Cu-VO indicated the production of $\cdot OH$ in the medium. Additionally, to support this result, we performed the same experiment in the presence of isopropanol (Nandanwar et al. 2020), a well-known $\cdot OH$ scavenger. The presence of isopropanol decreased the fluorescence intensity of terephthalic acid, which

confirm the anti-algal and dye degradation mechanism of Cu-VO was the production of $\cdot\text{OH}$ in the medium. The presence of $\cdot\text{OH}$ in the algal medium generates oxidative stress in the algal cells due to the production of an intracellular ROS (Nandanwar et al. 2020). The antitumor activity of vanadium dioxide nanocoated quartz glass was due to the induction of intracellular reactive oxygen species (Li et al. 2019)(Xi et al. 2020). It was found that $\text{ZnO-V}_2\text{O}_5$ trigger the upsurge of reactive oxygen species in bacteria, causing oxidative stress in bacteria and eventually cell death (Sun et al. 2019). This discussion indicated that Cu-VO could generate oxidative stress in algal cells leading to the production of intracellular ROS. The ROS assay showed the increase in the fluorescence intensity of non-fluorescent DCFH-DA incubated with Cu-VO treated algal cells. The production of fluorescent DCFH-DA indicated the production of intracellular ROS in *M. aeruginosa*, which might be the result of oxidative stress developed by $\cdot\text{OH}$ present in the algal medium. Intracellular ROS was a highly reactive species, degrading important cellular components such as DNA, RNA, proteins, and lipids, leading to cell death. Thus the production of extracellular $\cdot\text{OH}$ and intracellular ROS considered an important anti-algal mechanism.

5.5. Materials and Methods

5.5.1 Synthesis of Cu-VO

Copper-vanadium oxide (Cu-VO) was synthesized in the aqueous medium using a microwave oven (Samsung, Korea). In a typical process, 3mmol of $\text{Cu}(\text{NO}_3)_2 \cdot 3 \text{H}_2\text{O}$, 2 mmol of KVO_3 , and 1 g urea were added in 50 ml distilled water with vigorous stirring in a 250 ml conical flask. After 15 min, the conical flask was irradiated with 700 W microwave for 10 min. The reaction mixture was stirred after every 10 s. After 10 min the color of the reaction mixture turned colorless to yellow. The yellow-colored product was cooled and centrifuged at 4,000 rpm for 20 min. The product was washed four times with distilled water and three times with absolute ethanol. The washed product was kept for drying at 60 °C for up to 6 h in an oven. The dry product was annealed at 400 °C for 2 h at the heating rate of 5 °C/min. Afterward, the product was stored in a sealed glass tube.

5.5.2 Characterization

The morphology was observed by a field emission scanning electron microscopy (FESEM, JSM-6700F, JEOL, Tokyo, Japan), and the atomic% of Cu, V, and O in Cu-VO single crystal was analyzed using an energy dispersive X-ray spectrometer (EDX, INCAx-sight, Oxford). The crystalline nature of Cu-VO was observed by XRD analysis (Rigaku Ultima IV, Rigaku, Japan; Cu $K\alpha$ X-ray radiation). XPS measurement was carried out on a THERMO VG SCIENTIFIC (MultiLab 2000) X-ray photoelectron spectroscopes with a monochromatic Al-Ka source to explore the elements on the surface. FT-IR spectra were measured to find the type of bond present in Cu-VO (JASCO FT/IR-4100, Tokyo, Japan). The optical absorption property of the Cu-VO was analyzed by a UV–vis–NIR spectrophotometer (Perkin-Elmer Lambda 950, USA).

5.5.3 Photocatalytic experiments

5.5.3.1 Algae culture

A strain of *M. aeruginosa* (No. FBCC000002) was received from the Nakdonggang National Institute of Biological Resources (Sangju, Korea). The *M. aeruginosa* was cultured according to the condition given in our previous paper (Nandanwar et al. 2020).

5.5.3.2 Algae growth inhibition assay

The anti-algal assay was performed using the same procedure, as we mentioned in the previous paper (Nandanwar et al. 2020) with slight changes. Different concentration of Cu-VO (0, 0.4, 4, 8, 12, and 24 mg/L) and 2 mg of KVO₃ were incubated with *M. aeruginosa* for 5h under direct solar light.

5.5.3.3 Photocatalytic dye degradation

The Cu-VO nano-photocatalyst was applied for the degradation of methylene blue (MB) solution under direct solar light. The photocatalytic activity was carried out in conical flask. Twenty mg of Cu-VO nano-photocatalyst was added in 50 µM solution of MB. The resulting mixture was sonicated for 30 min to maintain adsorption-desorption equilibrium. Then, the conical flask was kept in direct solar light. The aliquots of the reaction mixture were filtered at every 1 h interval using 0.22 µm filter. UV-vis spectrum (BioDrop Duo, England, Cambridge, UK) of filtered solution was measured and %degradation was calculated as follows:

$$\% \text{Degradation} = \frac{A_i - A_f}{A_i} \times 100\%$$

where A_i and A_f were the absorbance value of solution at 0 and t min, respectively

5.5.4 Photocatalysis mechanism

5.5.4.1 $\cdot\text{OH}$ assay

The $\cdot\text{OH}$ assay was performed using the same procedure, as we mentioned in the previous paper (Nandanwar et al. 2020) with slight changes. The terephthalic acid solution was incubated with 4 mg/L of Cu-VO for 4h under solar light.

5.5.4.2 ROS assay

For ROS assay please refer our previous research paper (Nandanwar et al. 2020).



5.6. Conclusions

Cu-VO nanoparticles were effectively synthesized by a rapid and facile microwave-assisted synthesis method. The characterization of Cu-VO using FESEM, EDX, XRD, XPS, and FT-IR measurements indicated that Cu-VO contained typical monoclinic nanocrystals of approximately 58 nm. The calculated values of lattice constants from XRD data were matched well with the values given in the literature. XPS measurement showed the presence of $\text{Cu}^{2+}2p_{1/2}$, $\text{Cu}^{2+}2p_{3/2}$, $\text{V}^{5+}2p_{1/2}$, $\text{V}^{5+}2p_{3/2}$, and $\text{O}^{2-}1s$ in Cu-VO. FESEM analysis showed that the average particle size of Cu-VO was 132 nm. EDX analysis indicated the presence of Cu, V, and O elements in Cu-VO with atomic% of 3.13: 2: 7.25, respectively. XRD, and FT-IR analysis showed the presence of tetrahedral VO_4 and octahedral CuO_6 crystals in Cu-VO. Investigation of photocatalytic growth inhibition of algal cells showed that Cu-VO inhibited the growth of algae in a concentration-dependent manner. The superior anti-algal activity was found at a minimum effective concentration value of 4 mg/L under solar light. Cu-VO degraded 93% of methylene blue dye within 6h. The generation of highly reactive $\cdot\text{OH}$ radicals was indicated by the increase in fluorescence of terephthalic acid under solar light. $\cdot\text{OH}$ radical efficiently reacted with algae and dye, causing the degradation of algae and dye. The presence of $\cdot\text{OH}$ radical in the algal medium produced intracellular ROS in algae. The oxidative stress developed by intracellular ROS could destroy cell organelle, ultimately causing algal death. Further, our study suggested that a solar light active Cu-VO could be used as an efficient nanoparticle for wastewater treatment.

5.7. References:

- Akgul, Funda Aksoy, Guvenc Akgul, Nurcan Yildirim, Husnu Emrah Unalan, and Rasit Turan. 2014. "Influence of Thermal Annealing on Microstructural, Morphological, Optical Properties and Surface Electronic Structure of Copper Oxide Thin Films." *Materials Chemistry and Physics* 147(3):987–95.
- Ali, Imran, Omar M. L. Alharbi, Zeid A. Alothman, and Ahmad Yacine Badjah. 2018. "Kinetics, Thermodynamics, and Modeling of Amido Black Dye Photodegradation in Water Using Co/TiO₂ Nanoparticles." *Photochemistry and Photobiology* 94(5):935–41.
- Begum, Robina, Jawayria Najeeb, Ayesha Sattar, Khalida Naseem, Ahmad Irfan, Abdullah G. Al-Sehemi, and Zahoor H. Farooqi. 2020. "Chemical Reduction of Methylene Blue in the Presence of Nanocatalysts: A Critical Review." *Reviews in Chemical Engineering* 36(6):749–70.
- Boukhachem, A., B. Ouni, M. Karyaoui, A. Madani, R. Chtourou, and M. Amlouk. 2012. "Structural, Opto-Thermal and Electrical Properties of ZnO:Mo Sprayed Thin Films." *Materials Science in Semiconductor Processing* 15(3):282–92.
- Brynildsen, Mark P., Jonathan A. Winkler, Catherine S. Spina, I. Cody MacDonald, and James J. Collins. 2013. "Potentiating Antibacterial Activity by Predictably Enhancing Endogenous Microbial ROS Production." *Nature Biotechnology* 31(2):160–65.
- Cao, Xuesong, Le Yue, Fei Lian, Chuanxi Wang, Bingxu Cheng, Jinze Lv, Zhenyu Wang, and Baoshan Xing. 2021. "CuO Nanoparticles Doping Recovered the Photocatalytic Antialgal Activity of Graphitic Carbon Nitride." *Journal of Hazardous Materials* 403(July 2020):123621.
- Dai, Ruihua, Pinfei Wang, Peili Jia, Yi Zhang, Xincheng Chu, and Yifei Wang.

2016. "A Review on Factors Affecting Microcystins Production by Algae in Aquatic Environments." *World Journal of Microbiology and Biotechnology* 32(3):1–7.
- El-Sheekh, M. M., A. M. Haroon, and S. Sabae. 2017. "Activity of Some Nile River Aquatic Macrophyte Extracts against the Cyanobacterium *Microcystis Aeruginosa*." *African Journal of Aquatic Science* 42(3):271–77.
- Fan, Gongduan, Minchen Bao, Xiaomei Zheng, Liang Hong, Jiajun Zhan, Zhong Chen, and Fangshu Qu. 2019. "Growth Inhibition of Harmful Cyanobacteria by Nanocrystalline Cu-MOF-74: Efficiency and Its Mechanisms." *Journal of Hazardous Materials* 367:529–38.
- Ghiyasiyan-Arani, Maryam, Maryam Masjedi-Arani, Davood Ghanbari, Samira Bagheri, and Masoud Salavati-Niasari. 2016. "Novel Chemical Synthesis and Characterization of Copper Pyrovanadate Nanoparticles and Its Influence on the Flame Retardancy of Polymeric Nanocomposites." *Scientific Reports* 6(1):1–9.
- Ghiyasiyan-Arani, Maryam, Maryam Masjedi-Arani, and Masoud Salavati-Niasari. 2016. "Facile Synthesis, Characterization and Optical Properties of Copper Vanadate Nanostructures for Enhanced Photocatalytic Activity." *Journal of Materials Science: Materials in Electronics* 27(5):4871–78.
- Habibi-Yangjeh, Aziz, Soheila Asadzadeh-Khaneghah, Solmaz Feizpoor, and Afsar Rouhi. 2020. "Review on Heterogeneous Photocatalytic Disinfection of Waterborne, Airborne, and Foodborne Viruses: Can We Win against Pathogenic Viruses?" *Journal of Colloid and Interface Science* 580:503–14.
- Halbus, Ahmed F., Tommy S. Horozov, and Vesselin N. Paunov. 2020. "Surface-Modified Zinc Oxide Nanoparticles for Antialgal and Antiyeast Applications." *ACS Applied Nano Materials* 3(1):440–51.

- He, Pan, Guobin Zhang, Xiaobin Liao, Mengyu Yan, Xu Xu, Qinyou An, Jun Liu, and Liqiang Mai. 2018. "Sodium Ion Stabilized Vanadium Oxide Nanowire Cathode for High-Performance Zinc-Ion Batteries." *Advanced Energy Materials* 8(10):1–6.
- Jain, Siddarth, Bhagwati Sharma, Neha Thakur, Suryakant Mishra, and Tridib K. Sarma. 2020. "Copper Pyrovanadate Nanoribbons as Efficient Multienzyme Mimicking Nanozyme for Biosensing Applications." *ACS Applied Nano Materials* 3(8):7917–29.
- Jayaraj, Santhosh Kumar, Vishwanathan Sadishkumar, Thirumurugan Arun, and Paramasivam Thangadurai. 2018. "Enhanced Photocatalytic Activity of V₂O₅ Nanorods for the Photodegradation of Organic Dyes: A Detailed Understanding of the Mechanism and Their Antibacterial Activity." *Materials Science in Semiconductor Processing* 85(April):122–33.
- Jing, Liquan, Yuanguo Xu, Jie Liu, Minjing Zhou, Hui Xu, Meng Xie, Huaming Li, and Jimin Xie. 2020. "Direct Z-Scheme Red Carbon Nitride/Rod-like Lanthanum Vanadate Composites with Enhanced Photodegradation of Antibiotic Contaminants." *Applied Catalysis B: Environmental* 277(June):119245.
- Kadam, Rahul L., Yeonhee Kim, Sanjit Gaikwad, Mincheol Chang, Naresh H. Tarte, and Sangil Han. 2020. "Catalytic Decolorization of Rhodamine B, Congo Red, and Crystal Violet Dyes, with a Novel Niobium Oxide Anchored Molybdenum (Nb–O–Mo)." *Catalysts* 10(5).
- Karim, Md. Nurul, Mandeep Singh, Pabudi Weerathunge, Pengju Bian, Rongkun Zheng, Chaitali Dekiwadia, Taimur Ahmed, Sumeet Walia, Enrico Della Gaspera, Sanjay Singh, Rajesh Ramanathan, and Vipul Bansal. 2018. "Visible-Light-Triggered Reactive-Oxygen-Species-Mediated Antibacterial Activity of Peroxidase-Mimic CuO Nanorods." *ACS Applied Nano Materials*

1(4):1694–1704.

- Lebedev, Andrei, Franklin Anariba, Jeck Chuang Tan, Xu Li, and Ping Wu. 2018. “A Review of Physiochemical and Photocatalytic Properties of Metal Oxides against Escherichia Coli.” *Journal of Photochemistry and Photobiology A: Chemistry* 360:306–15.
- Leblanc, M., and G. Ferey. 1990. “Room-Temperature Structures of Oxocopper(II) Vanadate(V) Hydrates, $\text{Cu}_3\text{V}_2\text{O}_8(\text{H}_2\text{O})$ and $\text{CuV}_2\text{O}_6(\text{H}_2\text{O})_2$.” *Acta Crystallographica Section C Crystal Structure Communications* 46(1):15–18.
- Li, Jinhua, Meng Jiang, Huaijuan Zhou, Ping Jin, Kenneth M. C. Cheung, Paul K. Chu, and Kelvin W. K. Yeung. 2019. “Vanadium Dioxide Nanocoating Induces Tumor Cell Death through Mitochondrial Electron Transport Chain Interruption.” *Global Challenges* 3(3):1800058.
- Li, Malin, Yu Gao, Nan Chen, Xing Meng, Chunzhong Wang, Yaoqing Zhang, Dong Zhang, Yingjin Wei, Fei Du, and Gang Chen. 2016. “ $\text{Cu}_3\text{V}_2\text{O}_8$ Nanoparticles as Intercalation-Type Anode Material for Lithium-Ion Batteries.” *Chemistry - A European Journal* 22(32):11405–12.
- Lin, Zhaoyong, Weijia Li, and Guowei Yang. 2018. “Hydrogen-Interstitial CuWO_4 Nanomesh: A Single-Component Full Spectrum-Active Photocatalyst for Hydrogen Evolution.” *Applied Catalysis B: Environmental* 227(January):35–43.
- Liu, Guocong, Xuechen Duan, Haibin Li, and Hui Dong. 2009. “Hydrothermal Synthesis, Characterization and Optical Properties of Novel Fishbone-like $\text{LaVO}_4:\text{Eu}^{3+}$ Nanocrystals.” *Materials Chemistry and Physics* 115(1):165–71.
- Malka, Eyal, Ilana Perelshtein, Anat Lipovsky, Yakov Shalom, Livnat Naparstek, Nina Perkas, Tal Patick, Rachel Lubart, Yeshayahu Nitzan, Ehud Banin, and

- Aharon Gedanken. 2013. "Eradication of Multi-Drug Resistant Bacteria by a Novel Zn-Doped CuO Nanocomposite." *Small* 9(23):4069–76.
- Nandanwar, Sondavid, Myung Won Lee, Shweta Borkar, Jeong Hyung Cho, Naresh H. Tarte, and Hak Jun Kim. 2020. "Synthesis, Characterization, and Anti-Algal Activity of Molybdenum-Doped Metal Oxides." *Catalysts* 10(7):805.
- Ni, Shibing, Jianjun Ma, Jicheng Zhang, Xuelin Yang, and Lulu Zhang. 2015. "Electrochemical Performance of Cobalt Vanadium Oxide/Natural Graphite as Anode for Lithium Ion Batteries." *Journal of Power Sources* 282:65–69.
- Phongarthit, Kanitta, Pongsaton Amornpitoksuk, and Sumetha Suwanboon. 2019. "Synthesis, Characterization, and Photocatalytic Properties of ZnO Nanoparticles Prepared by a Precipitation-Calcination Method Using a Natural Alkaline Solution." *Materials Research Express* 6(4):45501.
- Ray, Schindra Kumar, Dipesh Dhakal, Yuwaraj K. Kshetri, and Soo Wahn Lee. 2017. "Cu- α -NiMoO₄ Photocatalyst for Degradation of Methylene Blue with Pathways and Antibacterial Performance." *Journal of Photochemistry and Photobiology A: Chemistry* 348:18–32.
- Regmi, Chhabilal, Yuwaraj K. Kshetri, Tae Ho Kim, Ramesh Prasad Pandey, Schindra Kumar Ray, and Soo Wahn Lee. 2017. "Fabrication of Ni-Doped BiVO₄ Semiconductors with Enhanced Visible-Light Photocatalytic Performances for Wastewater Treatment." *Applied Surface Science* 413:253–65.
- Sankar, Renu, Barathan Balaji Prasath, Ravichandran Nandakumar, Perumal Santhanam, Kanchi Subramanian Shivashangari, and Vilwanathan Ravikumar. 2014. "Growth Inhibition of Bloom Forming Cyanobacterium *Microcystis Aeruginosa* by Green Route Fabricated Copper Oxide Nanoparticles."

Environmental Science and Pollution Research 21(24):14232–40.

- Saravanan, R., V. K. Gupta, Edgar Mosquera, and F. Gracia. 2014. "Preparation and Characterization of V₂O₅/ZnO Nanocomposite System for Photocatalytic Application." *Journal of Molecular Liquids* 198:409–12.
- Saud, Safaa N., E. Hamzah, T. Abubakar, and S. Farahany. 2014. "Structure-Property Relationship of Cu-Al-Ni-Fe Shape Memory Alloys in Different Quenching Media." *Journal of Materials Engineering and Performance* 23(1):255–61.
- Seabold, Jason A., and Nathan R. Neale. 2015. "All First Row Transition Metal Oxide Photoanode for Water Splitting Based on Cu₃V₂O₈." *Chemistry of Materials* 27(3):1005–13.
- Shannon, Robert D., and Crispin Calvo. 1972. "Crystal Structure of a New Form of Cu₃V₂O₈." *Canadian Journal of Chemistry* 50(24):3944–49.
- Simo, A., M. Drah, N. R. S. Sibuyi, M. Nkosi, M. Meyer, and M. Maaza. 2018. "Hydrothermal Synthesis of Cobalt-Doped Vanadium Oxides: Antimicrobial Activity Study." *Ceramics International* 44(7):7716–22.
- Suman, T. Y., S. R. Radhika Rajasree, and R. Kirubakaran. 2015. "Evaluation of Zinc Oxide Nanoparticles Toxicity on Marine Algae *Chlorella Vulgaris* through Flow Cytometric, Cytotoxicity and Oxidative Stress Analysis." *Ecotoxicology and Environmental Safety* 113:23–30.
- Sun, Haiyun, Zhaoqing Yang, Yanan Pu, Wenwen Dou, Caiyu Wang, Wenhui Wang, Xiangping Hao, Shougang Chen, Qian Shao, Mengyao Dong, Shide Wu, Tao Ding, and Zhanhu Guo. 2019. "Zinc Oxide/Vanadium Pentoxide Heterostructures with Enhanced Day-Night Antibacterial Activities." *Journal of Colloid and Interface Science* 547:40–49.
- Suresh, R., K. Giribabu, R. Manigandan, S. Munusamy, S. Praveen Kumar, S.

- Muthamizh, A. Stephen, and V. Narayanan. 2014. "Doping of Co into V₂O₅ Nanoparticles Enhances Photodegradation of Methylene Blue." *Journal of Alloys and Compounds* 598:151–60.
- Svintsitskiy, Dmitry A., Tatyana Yu. Kardash, and Andrei I. Boronin. 2019. "Surface Dynamics of Mixed Silver-Copper Oxide AgCuO₂ during X-Ray Photoelectron Spectroscopy Study." *Applied Surface Science* 463(August 2018):300–309.
- Xi, Wen Song, Huan Tang, Yuan Yuan Liu, Chun Yuan Liu, Yanfeng Gao, Aoneng Cao, Yuanfang Liu, Zhang Chen, and Haifang Wang. 2020. "Cytotoxicity of Vanadium Oxide Nanoparticles and Titanium Dioxide-Coated Vanadium Oxide Nanoparticles to Human Lung Cells." *Journal of Applied Toxicology* 40(5):567–77.
- Yan, Xu, Shaofang Sun, Bo Hu, Xiyu Wang, Wei Lu, and Weidong Shi. 2013. "Enhanced Photocatalytic Activity Induced by Surface Plasmon Resonance on Ag-Loaded Strontium Titanate Nanoparticles." *Micro and Nano Letters* 8(9):504–7.
- Zelege, Misganaw Alemu, and Dong Hau Kuo. 2019. "Synthesis and Application of V₂O₅-CeO₂ Nanocomposite Catalyst for Enhanced Degradation of Methylene Blue under Visible Light Illumination." *Chemosphere* 235:935–44.
- Zelenski, Michael E., Natalia V. Zubkova, Igor V. Pekov, Maya M. Boldyreva, Dmitry Yu. Pushcharovsky, and Aleksey N. Nekrasov. 2011. "Pseudolyonsite, Cu₃(VO₄)₂, a New Mineral Species from the Tolbachik Volcano, Kamchatka Peninsula, Russia." *European Journal of Mineralogy* 23(3):475–81.
- Zhang, Chi, Yi Li, Danmeng Shuai, Yun Shen, Wei Xiong, and Linqiong Wang. 2019. "Graphitic Carbon Nitride (g-C₃N₄)-Based Photocatalysts for Water Disinfection and Microbial Control: A Review." *Chemosphere* 214:462–79.

- Zhang, Meng, Yusheng Niu, and Yuanhong Xu. 2020. "Heterogeneous Fenton-like Magnetic Nanosphere Coated with Vanadium Oxide Quantum Dots for Enhanced Organic Dyes Decolorization." *Journal of Colloid and Interface Science* 579:269–81.
- Zhang, Nuanqin, Chengjie Xue, Kuang Wang, and Zhanqiang Fang. 2020. "Efficient Oxidative Degradation of Fluconazole by a Heterogeneous Fenton Process with Cu-V Bimetallic Catalysts." *Chemical Engineering Journal* 380(May 2019):122516.
- Zhang, Shaoyan, Yan Sun, Chunsheng Li, and Lijie Ci. 2013. "Cu₃V₂O₈ Hollow Spheres in Photocatalysis and Primary Lithium Batteries." *Solid State Sciences* 25:15–21.
- Zhang, Xin, Jie Zhang, Jianqiang Yu, Yan Zhang, Fengkai Yu, Lei Jia, Yunling Tan, Yimen Zhu, and Baorong Hou. 2019. "Enhancement in the Photocatalytic Antifouling Efficiency over Cherimoya-like InVO₄/BiVO₄ with a New Vanadium Source." *Journal of Colloid and Interface Science* 533:358–68.

국문요약

유해성 시아노 박테리아와 같은 세균이나, 염료와 같은 환경 오염 물질은 - 신선한 식수 및 위생에 대한 접근을 제한합니다. 산업화, 지구 온난화 및 높은 생활 수준은 환경 오염을 가속하고 인체 건강에 지속적인 위험을 유발합니다. 세균은 어디에나 존재하며 여러 항생제에 대한 내성을 발생시켰으며 이는 최근 제약 산업에 가장 큰 위협 중 하나입니다. 지구 온난화와 부영양화는 수중의 유해성 시아노 박테리아의 성장을 가속합니다. 시아노 박테리아는 수중에 독소를 생성하고 생명체의 건강을 위협합니다. *Microcystis aeruginosa* 는 신경독 및 간 독소와 같은 시아노톡신을 방출하는 담수 조류입니다. 메틸렌 블루 (MB)는 여러 산업 및 연구 기관에서 사용되며 수중으로 방류됩니다. 메틸렌 블루에 오염된 물은 인간에게 여러 해로운 영향을 미칩니다. 이러한 문제에 대응하려면 효율적이고 쉽고 저렴한 기술이 필요합니다. 유기 금속 복합체 (OC)와 나노 금속 산화물 (NMO)은 이러한 환경 문제를 완화할 수 있습니다. 이러한 환경 문제에 대처하기 위해서 OC 및 NMO의 오염 통제에 대한 잠재력을 평가하기 위한 심층적인 연구가 필요합니다.

따라서 우리 연구의 주요 목적은 시아노 박테리아의 성장 억제와 염료의 분해를 위한 유기 금속 복합체와 나노 금속 산화물의 합성 및 분류였습니다. 우리는 6개의 유기 금속 착물 (dichloro-bis(2-isopropylimidazole)-zinc(II) (**Zn1**), dichloro-bis(2-methylbenzimidazole)-zinc(II) (**Zn2**), dichloro-bis(2-methylbenzoxazole)-zinc(II) (**Zn3**), dichloro-bis(2-methylbenzimidazole)-cobalt(II) (**Co1**), dichloro-bis(2-methylbenzoxazole)-cobalt(II) (**Co2**), 그리고 dichloro-bis(2-methylbenzothiazole)-cobalt(II) (**Co3**) complexes) 및 두 개의 나노 금속 산화물 (molybdenum doped zinc oxide (**4**) 과 copper-vanadium oxides (**5**))에 대해 연구했습니다. 복합 Zn1-3 / Co1-3 은 실온에서 금속과 리간드를 혼합하여 합성되었습니다. 몰리브덴 도핑된 산화 아연(**4**) (MoZnO)은 dry ball mill 법을 사용하여 합성된 반면 구리 도핑된 산화 바나듐(**5**)은 마이크로파법을 사용하여 합성되었습니다. 유기 금속 복합체는 UV-visible

spectroscopy (UV-VIS), ¹H NMR spectroscopy, single X-ray crystallography 및 elemental analysis 를 사용하여 분류되었으며, 금속 복합체는 FESEM (field Emission 주사 전자 현미경), Energy-dispersive X-ray spectroscopy (EDS), X-선 회절 (XRD) 및 FT-IR 분광법을 이용하여 분류되었습니다. 유기 금속 복합체 (**Zn1-3** / **Co1-3**)는 내성 균주를 포함한 그람 양성 및 그람 음성 박테리아에 대해 적용되었습니다. 나노 금속 산화물 **4** 는 가시 광선 하에서 유해성 시아노 박테리아에 대해 적용되었고 **5** 는 유해성 시아노 박테리아 및 염료에 대해 적용되었습니다. 복합체 **Zn1-3** / **Co1-3** 및 나노 금속 산화물 **4** 및 **5** 의 작용 메커니즘을 각각 세균, 시아노 박테리아 및 염료에 대해 조사했습니다. Sytox green assay 는 **Co1-3** 를 단독으로 사용했을 때 와 암피실리과 같이 사용했을 때의 세균 표면 침투를 연구하기 위해 사용되었습니다. 나노 금속 산화물 **4** 와 **5** 의 산화 분해 메커니즘을 찾기 위해 ·OH, ROS 및 지질 과산화 분석을 수행했습니다.

단결정 X-선 분석으로 복합 **Zn1-3** / **Co1-3** 이 사면체 구조를 가짐을 알 수 있었습니다. 금속 산화물의 XRD 결과는 나노 금속 산화물 **4** 및 **5** 의 결정 특성을 반영합니다. FESEM 으로 얻은 나노 금속 산화물 **4** 및 **5** 의 평균 직경은 40 nm (**4**) 및 133 nm (**5**) 였습니다. 복합체 **Zn1-3** / **Co1-3** 은 50-200 µg/ml 의 농도 범위 내에서 모든 항생제 민감성 세균에 대해 좋은 항균성을 나타냈습니다. 복합체 **Co1-3** 은 복합체 **Zn1-3** 보다 높은 항균성을 나타냈습니다. **Co2** 및 **Co3** 복합체의 항균성은 다른 세균에 비해 최소 억제 농도 (MIC) 값이 12.5 µg / mL 로 *S. aureus* 에 대해 더 높았습니다. 암피실린 (AMP)과 복합체 **Co1-3** 의 조합은 Methicillin-Resistant *S. aureus* 균주 (MRSA)에 대한 **Co1-3** 의 항균성을 증가시킵니다. 흥미롭게도 복합체 **Co1-3** 단독 및 AMP 와의 조합은 다른 항균 작용 메커니즘을 나타 냈습니다. AMP 와 결합 된 **Co2** 및 **Co3** 복합체는 MRSA 막을 파괴 한 반면 나머지 복합체는 그러한 메커니즘을 나타내지 않았습니다. 나노 금속 산화물 **4** 와 **5** 는 최소 유효 농도 1mg / L 로 및 4 mg / L *M. aeruginosa* 에 대한 항 조류 활성을 나타 냈습니다. 나노 금속 산화물 **4** 와 **5** 의 항 조류 메커니즘을 조사한 결과 가시

광선 하에서 BG-11 매질에서 수산화 라디칼($\cdot\text{OH}$)이 생성되는 것으로 나타났습니다. $\cdot\text{OH}$ 는 *M. aeruginosa* 지질막의 과산화를 유발하는 반응성이 높은 산소종으로 세포 내 ROS의 생성을 강화하여 시아노 박테리아의 응집을 유발합니다. 나노 금속 산화물 5는 MB를 93.8% 분해했습니다. 결과적으로 복합체 Zn1-3/ Co1-3과 나노 금속 산화물 4와 5를 이용하여 세균과 시아노박테리아, 염료를 더 효과적으로 제어할 수 있었습니다



Acknowledgement

I would first like to thank my supervisor, Prof. Jeong Hyung Cho, Department of Interdisciplinary Program of Marine Conversion Design, for his mentorship, encouragement, patience, and financial support. I would like to express deepest gratitude to my co-supervisor, Prof. Hak Jun Kim, Department of Chemistry, for his mentorship, encouragement, and for providing me this priceless opportunity to learn scientific research and introducing me to the field of Organometallic chemistry and Nanotechnology. His guidance and liberty enhanced the tuning of my focus and the freedom to develop and express my own scientific ideas, which was of great importance to me in raising individual abilities. His expertise was invaluable in formulating the research questions and methodology. His insightful feedback pushed me to sharpen my thinking and brought my work to a higher level. Thank you for always being open to discussion and giving me the freedom to develop myself as a researcher. The meetings and conversations were vital in inspiring me to think outside the box, from multiple perspectives to form a comprehensive and objective critique.

I would like to thank thesis committee members, Prof. Shin Hee Jae, Prof. Myung Won Lee, Prof. Syungi Lee, Prof. Hak Jun Kim, and Prof. Jeong Hyung Cho for their careful revision and valuable suggestions for my thesis. My expanding knowledge and widening experience are to be thanked for their helpful inputs, scientific contribution as well as discussion theme.

I would like to say special thanks to the Dr. Naresh Hiralal Tarte, Department of Chemistry and Biology, KSA of KAIST for allowing me to work in his lab, continuous support in research, and discussing unique research ideas. I would like to thank my colleagues Ms. Shweta Bharat Borkar and Mr. Young Hoon Lee for their help in my research and creating nice working environment.

I must also thank Mr. Chetan Chunilal Patel and Mr. Rahul L. Kadam for their valuable guidance and mental support. I am also thankful to those who were involved directly or indirectly in making my life happy and helped during my stay in Korea.

My family being the backbone of my life, I couldn't have achieved this without their support, appreciation, extraordinary love, concern and cushion. I dedicated this thesis to my father Shri. Keshao Rama Nandanwar and my mother Mrs. Rajashri Keshao Nandanwar.

Last but not the least; I would like to thank omnipresent almighty, for answering my prayers. Thank you once again for sharing, for all your blessings and for opening me a door to a new life. Namaste!!!

